UNIVERSITY OF SOUTHAMPTON

FACULTY OF ENGINEERING AND THE ENVIRONMENT

Fluid structures interactions research group

Intermediate strain rate testing methodologies and full-field optical strain measurement techniques for composite materials characterisation

by

Marco Luigi Longana

Thesis for the degree of Doctor of Philosophy

March 2014

UNIVERSITY OF SOUTHAMPTON

ABSTRACT

FACULTY OF ENGINEERING AND THE ENVIRONMENT

Fluid structures interactions research group

Doctor of Philosophy

Intermediate strain rate testing methodologies and full-field optical strain measurement techniques for composite materials characterisation

by Marco Luigi Longana

Two optical full-field strain measurement techniques, Digital Image Correlation and the Grid Method, are applied to characterise the strain-rate dependent constitutive behaviour of composite materials. Optical strain measurement techniques based on full-field images are well established for material characterisation in the quasi-static strain rate region, however in this work they are developed to study the material behaviour at intermediate strain rates, which is relatively unexplored. For this purpose a testing methodology that combines high speed imaging and the use of a high speed test machine is devised. The overall goal is to extract composite materials constitutive parameters to be used in the modelling of strain rate dependent behaviour. Particularly the strain rate dependence of the stiffness of glass and carbon fibre reinforced epoxy materials is investigated. A characterisation procedure based on off-axis specimens with oblique end-tabs is developed and applied to the study of the shear behaviour of a carbon/epoxy composite material.

The research in the PhD programme constitutes an essential first step for more profitable applications of full-field measurement techniques to high speed testing. Full-field data acquired with the experimental methodology devised here can be used to investigate non linear material behaviours. Furthermore this experimental methodology, applied to specimens that generate non uniform strain fields, can produce strain maps useful for the application of the Virtual Fields Method. This will lead to a reduction of the experiments needed to characterise materials.

Alla mia famiglia
per il loro incoraggiamento,
aiuto e sostegno

"Restiamo umani,
anche quando intorno a noi l'umanità pare si perda."
Vittorio Arrigoni

Contents

List of Figures

List of Tables

Declaration of authorship

I, *Longana Marco Luigi*, declare that the thesis entitled:
"Intermediate strain rate testing methodologies and full-field optical strain measurement techniques for composite materials characterisation"
and the work presented in the thesis are both my own, and have been generated by me as the result of my own original research. I confirm that:

- this work was done wholly or mainly while in candidature for a research degree at this University;
- where any part of this thesis has previously been submitted for a degree or any other qualification at this University or any other institution, this has been clearly stated;
- where I have consulted the published work of others, this is always clearly attributed;
- where I have quoted from the work of others, the source is always given. With the exception of such quotations, this thesis is entirely my own work;
- I have acknowledged all main sources of help;
- where the thesis is based on work done by myself jointly with others, I have made clear exactly what was done by others and what I have contributed myself;
- parts of this work have been published as:
  - **Approaches to synchronise conventional measurements with optical techniques at high strain rates**
    D.A. Crump, J.M. Dulieu-Barton, M.L. Longana
    Applied Mechanics and Materials Vol. 70 (2011) pp 75-80
  - **Application of optical measurement techniques to high strain rate deformations in composite materials**
    M.L. Longana, J.M. Dulieu-Barton, S. Syngellakis
    7th Asian Conference on Composite Materials, Taipei, TW, 15-18 November 2010.

– **Identification of constitutive properties of composite materials under high strain rate loading using optical strain measurement techniques** M.L. Longana, J.M. Dulieu-Barton, F. Pierron, S. Syngellakis
16th International Conference on Composite Structures, Porto, PT, 28-30 June 2011.

– **Identification of constitutive properties of composite materials under high strain rate loading using optical strain measurement techniques**
M.L. Longana, J.M. Dulieu-Barton, F. Pierron
15th European Conference on Composite Materials, Venice, IT, 24-28 June 2012.

Signed: . . . . . .

Date: . . . . . .

Acknowledgements

I want to thank my supervisors Prof. Janice M. Dulieu-Barton, Prof. Fabrice Pierron and Dr. Stavros Syngellakis for their help and guidance.

A big thank you goes to all the FSI colleagues (in particular Gary Battams, George Crammond, Duncan Crump, Richard Fruehmann, Andy Robinson, Rachael Waugh and Shufeng Zhang) for sharing their knowledge and advices.
I also wish to thank all the technicians who helped me all through this work, and the other users of TSRL for the long, tough but good hours spent together.

A big hug to all my great friends, old and new, far and near, at home or scattered around the world, who I hounded or neglected in the last few year: you know who you are. All my love to my Piccolinka.

Finally the most grateful thoughts go to my family, who helped and supported me with love and encouragements all through this journey.

This thesis is written with LaTeX.

Acronyms

CCD Charge Coupled Device.
CFRP Carbon Fibre Reinforced Plastics.
CMOS Complementary Metal Oxide Semiconductor.
CV Coefficient of Variation.

DIC Digital Image Correlation.
DOF Depth of Field.
DW Drop Weight Machine.

FRP Fibre Reinforced Plastics.

GFRP Glass Fibre Reinforced Plastics.
GM Grid Method.

QS Quasi-Static.

RMS Root Mean Square.

SH Servo Hydraulic Machine.
SHB Split Hopkinson bar.

VFM Virtual Fields Method.
VHS Very High Speed.

List of Symbols

S_{ab} Specimen axis: Compliance matrix coefficients.
u Specimen axis: Longitudinal displacement.
v Specimen axis: Transverse displacement.
ϵ_{xx} Specimen axis: Longitudinal strain.
γ_{xy} Specimen axis: Engineer shear strain.
ϵ_{yy} Specimen axis: Transverse strain.
σ_{xx} Specimen axis: Longitudinal stress.
ϵ_{11} Material axis: Strain parallel to the fibre direction.
ϵ_{12} Material axis: Shear strain.
γ_{12} Material axis: Engineer shear strain.
ϵ_{22} Material axis: Strain perpendicular to the fibre direction.
E_{11} Material axes: Longitudinal modulus (parallel to the fibre direction).
E_{22} Material axes: Transverse modulus (perpendicular to the fibre direction).
G_{12} Material axes: Shear modulus.
ν_{12} Material axes: Major Poisson's ratio.
σ_{11} Material axis: Stress parallel to the fibre direction.
σ_{12} Material axis: Shear Stress.
σ_{22} Material axis: Stress perpendicular to the fibre direction.
M Regression function: Generic material property.
α Regression function: First material constant.
β Regression function: Second material constant.
χ Regression function: Third material constant.
A Grid Method: Amplitude.
Γ Grid Method: Contrast.
F Grid Method: Periodic function.
f Grid Method: Frequency of the carrier.
p Grid Method: Grid pitch.
Φ_x Grid Method: Carrier phase modulation along the x axis.
Φ_y Grid Method: Carrier phase modulation along the y axis.
V Nominal Strain Rate calculation: Actuator displacement speed.
L Nominal Strain Rate calculation: Gauge Length.

$\dot{\epsilon}$ Strain Rate.

ϑ Off axis tensile test: Off-axis angle.

φ Off axis tensile test: End-tab Anlge.

ω_{Long} Stress wave frequency calculation: Stress wave frequency.

L Stress wave frequency calculation: Travelling length.

E_M Stress wave frequency calculation: Material stiffness.

ρ_M Stress wave frequency calculation: Material density.

z Imaging parameters: Imaging distance.

dz Imaging parameters: Out of plane movement.

1 Introduction

1.1 Background and motivation

In general, a composite material system is the combination of two or more different materials, or phases. Its engineering properties are a combination of the individual constitutive materials properties and their interaction, i.e. the interface. The possibility of producing a material able to fulfil certain engineering tasks is the strength of composite materials which, in the last decades, have been used in several roles, e.g. ablative materials for thermal protection, vibration damping and primary structural materials. Historically, the first example of a composite material used as engineering material is wood used as a structural material, which is composed of a series of cellulose fibres, that bear the tensile loads, in a lignin matrix that bears the compressive loads. The earliest application of a man-made composite material was for building construction; straw and mud were mixed to form bricks. Apart from these natural composite material examples, composites are almost industrially irrelevant till the second post-war period. The real boost in the usage of composite materials for engineering and industrial applications was given by development of organic polymers synthesis techniques and by the improvements in materials manufacturing technologies. The progress in the chemistry and manufacturing field made possible the development of composite materials able to replace metals in many applications [1]. Specifically the most commonly used composite material are Fibre Reinforced Plastics (FRP). By means of example the development of FRP application in aeronautic applications is shown in Figures 1.1 and 1.2 from [2].

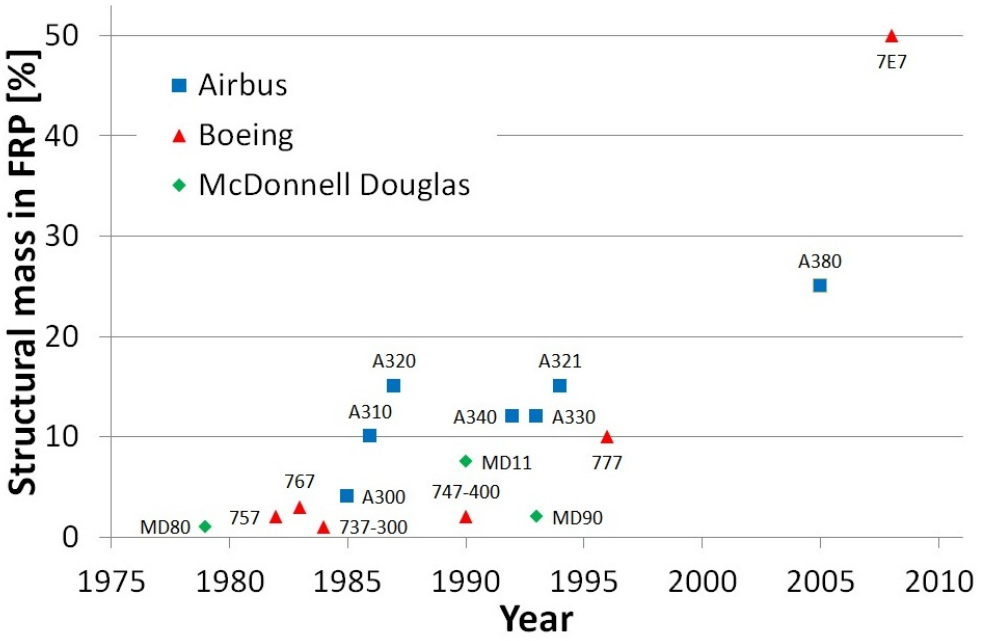

Figure 1.1: Development of composite share in civil aircraft structure, [2]

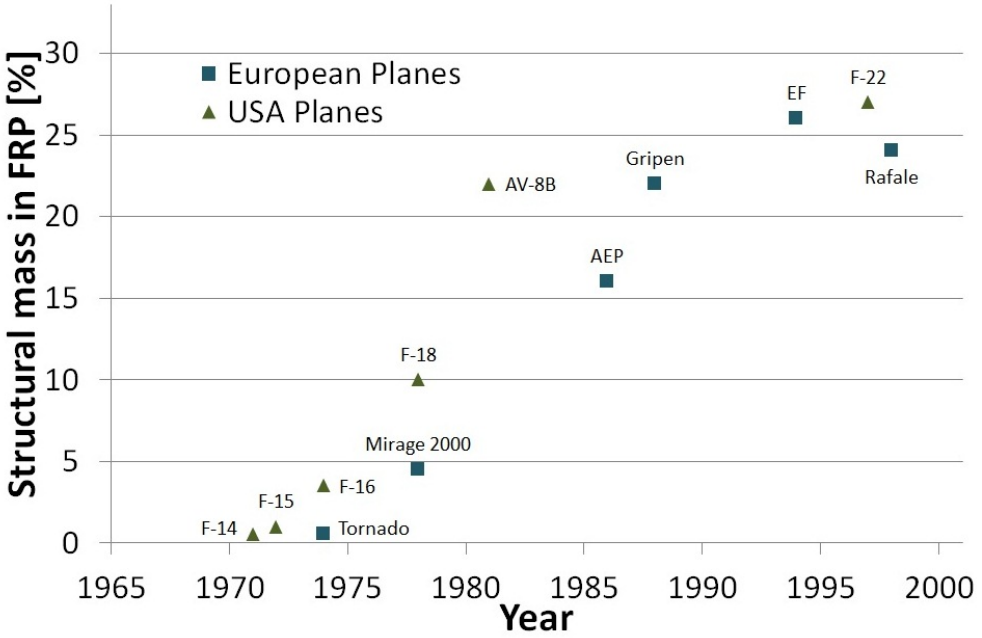

Figure 1.2: Development of composite share in military aircraft structure, [2]

The work described in the thesis focuses on the structural application of fibre reinforced thermosetting polymeric materials. These types of materials are a combination of a continuous polymeric matrix and an elongated fibrous phase. The fibres bear the tensile load while the matrix is responsible for transferring the load between the fibres, maintaining the shape and hence the compatibility as well as a corrosion protection role. The contact region between the two main constituents,

i.e. fibres and matrix, is called the interface, in certain case a new phase is formed in this region, the interphase. Composite materials are used in structural applications where the strength to weight ratio is important. Therefore during their working life, this materials have to withstand severe static loads as well as high velocity events, such as vibration and impact.

The structure of the material under investigation is further complicated by the typical laminated composition of composite materials, as can be seen in Figures 1.3 and 1.4.

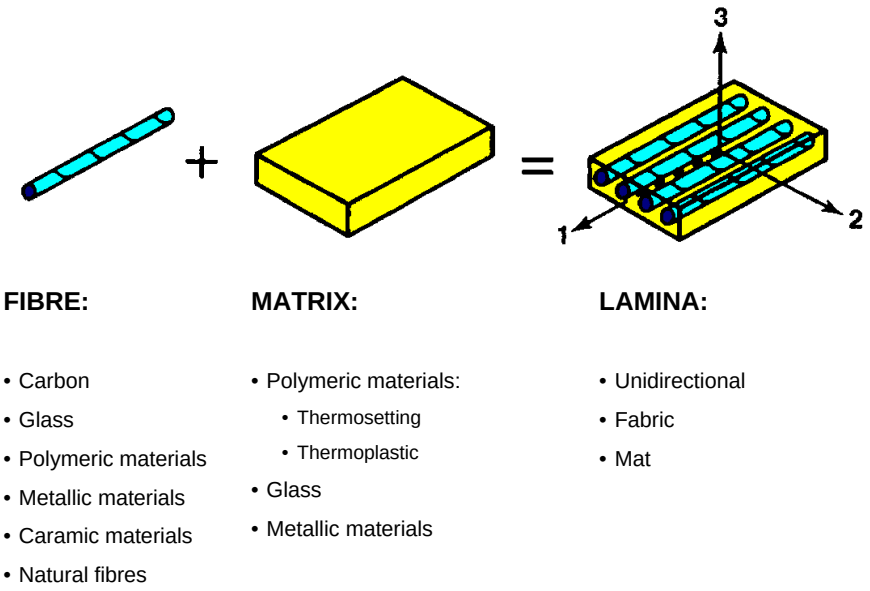

Figure 1.3: Typical fibre reinforced composite materials composition, as in [3]

The reinforcement fibres, usually bundled together with a specified twisting, have cylindrical shape, with a negligible cross section compared to the length. The fibres are generally organised in sheets of parallel fibres put side by side or weaved in fabric, known as lamina or ply. The bulk material is obtained by stacking a sequence of these laminae, often with different relative angle of the fibres, and connecting the fibres with the polymeric matrix, as shown in Figure 1.4.

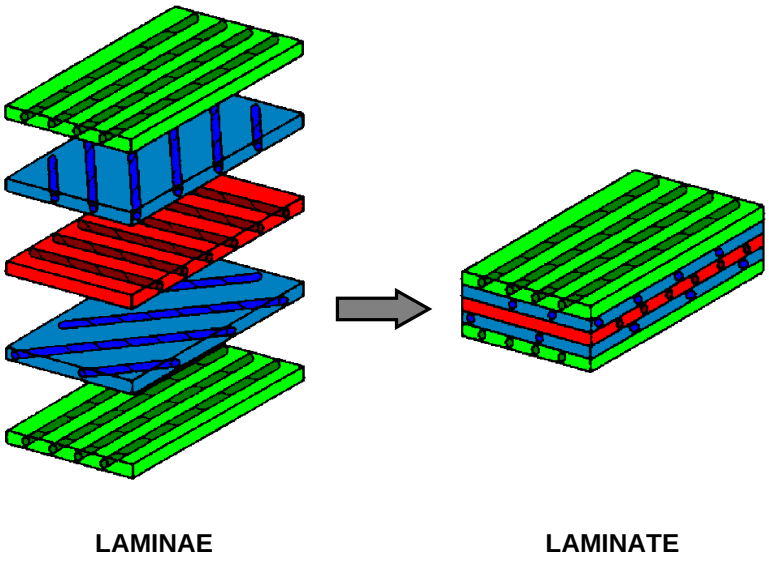

Figure 1.4: Composite material laminate, as in [3]

The reasons for the substantial multi scale nature of polymeric composite materials are as follows:

1. The layered structure can be treated as a bulk material, known as the laminate. Its mechanical properties are calculated by Classical Laminate Theory, [3] and the behaviour of the individual plies homogenised into a single material response.

2. In a more detailed approach, composite materials can be considered as a sequence of stacked layers or plies, known as laminae. Besides the overall behaviour of the bulk structure, the behaviour of a single layer can be taken into account; this is typical in composite failure analysis where criteria such as first ply failure or last ply failure are used. It is also relevant to account for the interaction between each ply that can significantly modify the characteristics of the material, i.e. the inter-laminar properties of the materials, [3].

3. Each ply, or lamina, is composed of two different phases, as shown in Figure 1.3, with considerably different mechanical characteristics:

   a) The fibres with elasto-brittle behaviour.

   b) The polymeric matrix with visco-elastic behaviour

The extensive application of composite materials started in the second half of the previous century and is relatively new in engineering. Their characteristic behaviour under static load can be said to be reasonably well understood; a deeper knowledge about their behaviour under high strain rate and fatigue load is required. It is

evident, from the available literature on the modelling of high strain rate response of composite materials, that considerable efforts have been made to model their fracture behaviour, but, despite its importance, the high strain rate behaviour of composite materials before the damage initiation has not been investigated in sufficient depth. Moreover it is evident from the literature [4] [5] that there is a lack of reliable high-strain rate experimental data to inform models of the strain rate dependent behaviour of composite materials. Being able to correctly model this behaviour is important for various reasons:

- The apparent Young's modulus of the material is strongly dependent on the strain rate, [6].
- The energy absorbed by a material while deforming is a key parameter in fracture mechanics and can considerably vary with the strain rate.
- Often high load rate events, that do not produce a failure of the material at ply scale, can induce another mode of failure, such as delamination, [7] and [8] or micro-cracking. For these reason it is important to be able to estimate the deformation of the material and its dependence on the loading rate.
- The failure stress is also function of the load rate.

1.2 Aim and Objectives

The PhD project is part of a larger investigation focused on a deeper understanding of the behaviour of fibre reinforced thermosetting polymeric materials subjected to high strain rate events. The structure of the Damage Tolerance Project as devised in September 2009 is shown in Figure 1.5.

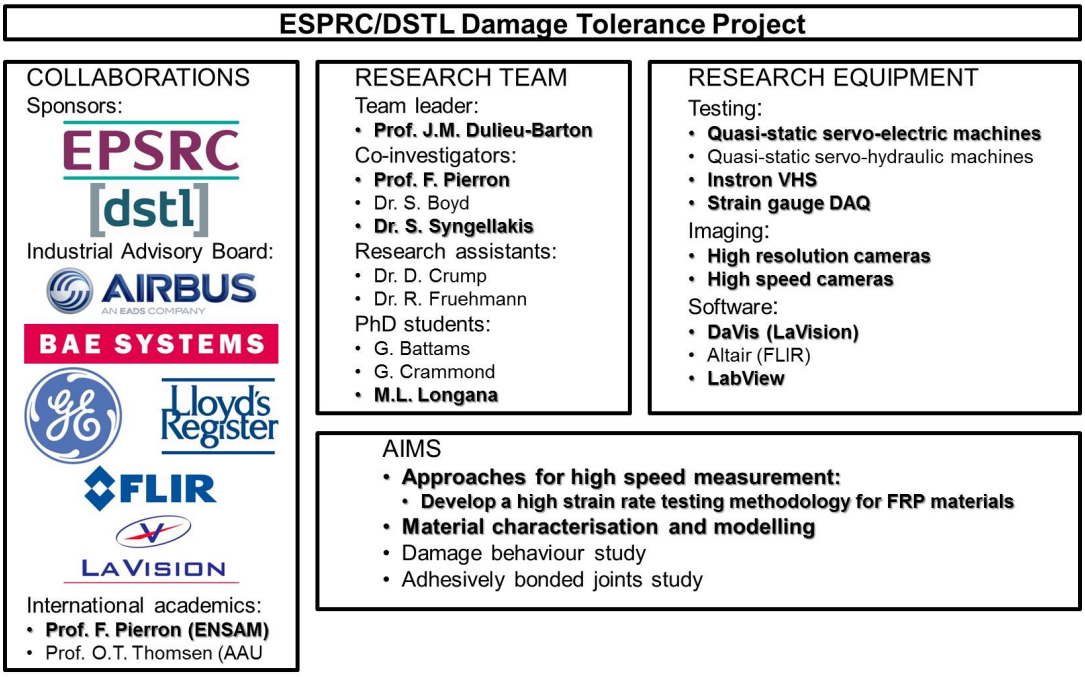

Figure 1.5: Damage Tolerance Project structure, September 2009

The aim of this project is to investigate the strain rate dependent behaviour of fibre reinforced thermosetting polymeric materials before damage initiation. An experimental methodology based on the usage of an Instron Very high speed (VHS) machine, to load the material, and of full-field optical strain measurement techniques, using high speed imaging, is devised. The constitutive parameters are then used to build and inform a phenomenological model able to describe the strain rate dependence of the stiffness of FRP materials.

This aim is achieved by meeting the following specific objectives:

- Devise a sound testing procedure to load FRP materials at different strain rate and obtain strain informations over the whole specimen surface.
  - The available technique for high strain rate testing on composite materials will be analysed.
  - An experimental set-up will be developed to load specimen to a nominal strain rate up to 100 s^{-1}.
  - A methodology to collect images at high frame rate suitable to perform full-field optical strain measurement will be devised.
  - Different full-field strain measurement techniques will be investigated. Digital Image Correlation (DIC) and the Grid Method (GM) will be compared with strain gauges measurements to evaluate their effectiveness in measuring the strain during high rate events.

- Investigate and characterise the rate dependent behaviour of composite materials:
  - The available literature about the strain rate dependent composite material behaviour is studied and used to define a base line knowledge to build upon.
  - A suitable methodology to use the devised experimental procedure to evaluate the shear modulus will be identified.
  - An efficient experimental procedure will be devised to simplify the test procedures needed to study the strain rate dependent behaviour of longitudinal, transversal and shear moduli (E_{11}, E_{22} and G_{12}).
- The collected data will be used to inform a model of the strain rate dependent behaviour of of E_{11}, E_{22} and G_{12} in FRP materials.

This research seeks to prove the suitability of full-field optical techniques to measure strain during high deformation speed events and investigate the strain rate dependency of the material behaviour in the linear region of the stress-strain curve. The work presented here is the first step for more profitable applications of full-field measurement techniques also at high speed. These non contact techniques allow the investigation of non linear material deformations and failure mechanisms, overcoming the limitations of contact techniques, such as strain gauges and extensometers. If applied to specimens able to generate a non-homogeneous strain field, [9], full-field measurement techniques coupled with the Virtual Fields Method (VFM), [10] allow the reduction of the number of experiments needed to fully characterise the material behaviour.

1.3 Novelty statement

The research described in the thesis is aimed at the development and validation of a new experimental methodology to perform test at strain rates between 0.01 and 100 s^{-1}. The approach combines the application of high rate load using a high speed servo-hydraulic tensile test machine with high speed image capture so full-field optical strain measurement techniques can be utilised. High speed servo-hydraulic tensile test machines, in contrast with the Split Hopkinson bar (SHB) widely used in the analysed literature, allows the usage of standard dimensions specimens [11]. This provides the opportunity to develop characterisation techniques used in quasi-static testing to higher strain rates. The novelty of the new experimental methodology is as follows:

- The combined use of high speed imaging and full-field measurement techniques with high speed servo-hydraulic machine to achieve quantitative maps of displacement, strain and strain rate over the whole specimen surface.
- The design of a specimen that allows to smoothly apply the load when performing high speed tests.
- The definition of a loading system suitable to perform high speed tests and the investigation of its impact on the experimental outputs.

Two optical full-field strain measurement techniques are developed for high strain rate measurements: DIC [12] and GM [13]. The novelty in the application of full-field strain measurement techniques are:

- The use of DIC and GM on the same specimen to directly compare the two techniques.
- The use of full-field measurement techniques in combination with a novel material characterisation procedure to study the strain rate dependence of composite material behaviour.

A novel experimental procedure, which uses off-axis tests on specimens with oblique end-tabs is developed to study the strain rate dependence of longitudinal, transverse and shear moduli in FRP materials. The novelty in this part of the work is as follows:

- The definition of an experimental procedure to study the strain rate dependence of constitutive moduli of FRP materials.
- The definition of a robust method to identify the elastic shear modulus G_{12} from the stress-strain curve.
- The use of a regression function to describe the strain rate dependent behaviour of all the constitutive moduli of FRP materials.

1.4 Structure of the thesis

Chapter 2 deals with the applications of full-field strain measurement techniques to material characterisation: general considerations about image acquisition to perform optical measurement techniques are given in Section 2.2, the preparatory work, conducted in the quasi-static range, to apply DIC and GM is described in Section 2.3 and 2.4.

The development of a testing methodology to perform high speed tests is detailed in Chapter 3. The chapter is opened, in Section 3.2, with an review of the experimental work carried on to characterise the strain rate dependence of E_{11}, E_{22} and G_{12}. Section 3.3 deals with definition of correct specimen loading condition, while the integration of optical techniques to high speed testing is described in Section 3.4

Chapter 4 is dedicated to the validation of the devised experimental technique trough the characterisation of the strain rate dependence of the Young's modulus of a Glass Fibre Reinforced Plastics (GFRP) material.

All the aspect related to the elaboration of a robust methodology to fully characterise the strain rate dependence of of longitudinal, transverse and shear moduli in a Carbon Fibre Reinforced Plastics (CFRP) materials are presented in Chapter 5.

2 Application of full-field optical measurement techniques to material characterisation

2.1 Introduction

Over the last decade, the development and improvement of devices for capturing electromagnetic radiation have made possible the development of sensors able to record images with higher quality, in a shorter time and at different frequencies than visible light. The availability of such images allowed the development of new measurement methodologies for surface stresses and strains, e.g. Thermoelastic Stress Analysis (TSA) [14], DIC [15] and the GM [13]. In their review of experimental techniques for high rate deformation and shock studies, Field *et al.* [16] suggest the use of optical techniques for full-field strain measurement on non-standard materials at high strain rate. The advantages of such techniques appear evident:

- There is no mechanical interaction between the measurand and the sensor:
  - The observed system is not modified by the measurement process. The only requirement is a correct preparation of the specimen surface to be able to retrieve the desired information, stress or strain, from the images.
  - The measurement process can continue up to the specimen failure, which is not possible with contact measurement techniques. This is particularly appealing in case of shock loading that, for example, might cause strain gauges or extensometers to detach from the specimen.
- It is possible to obtain strain and displacement maps over the whole specimen surface or large areas of it. This allows the capture of non homogeneous strain fields and non uniform behaviour of the specimens.

Grédiac describes the importance of full-field methods for the modelling of composite materials, [17] and [18]. Full-field techniques enable the relaxation of the restrictions on specimen dimension and loading conditions when performing mechanical characterisation tests on composite materials. In general, these tests require

a homogeneous stress-strain field in the material; this status is difficult to achieve in composite materials because of their anisotropy and their heterogeneity at different scales. Full-field techniques provide information over the complete stress-strain field and allow the heterogeneities in the field to be identified and accounted for in the modelling stage. Full-field strain data are also fundamental for material characterisation with the VFM [10]. Furthermore, they significantly reduce the number of experiments and sensors needed to identify all the parameters required to characterise an anisotropic material, [19], [20] and [21]. Figure 2.1 reports the link between the measurements and the modelling activities.

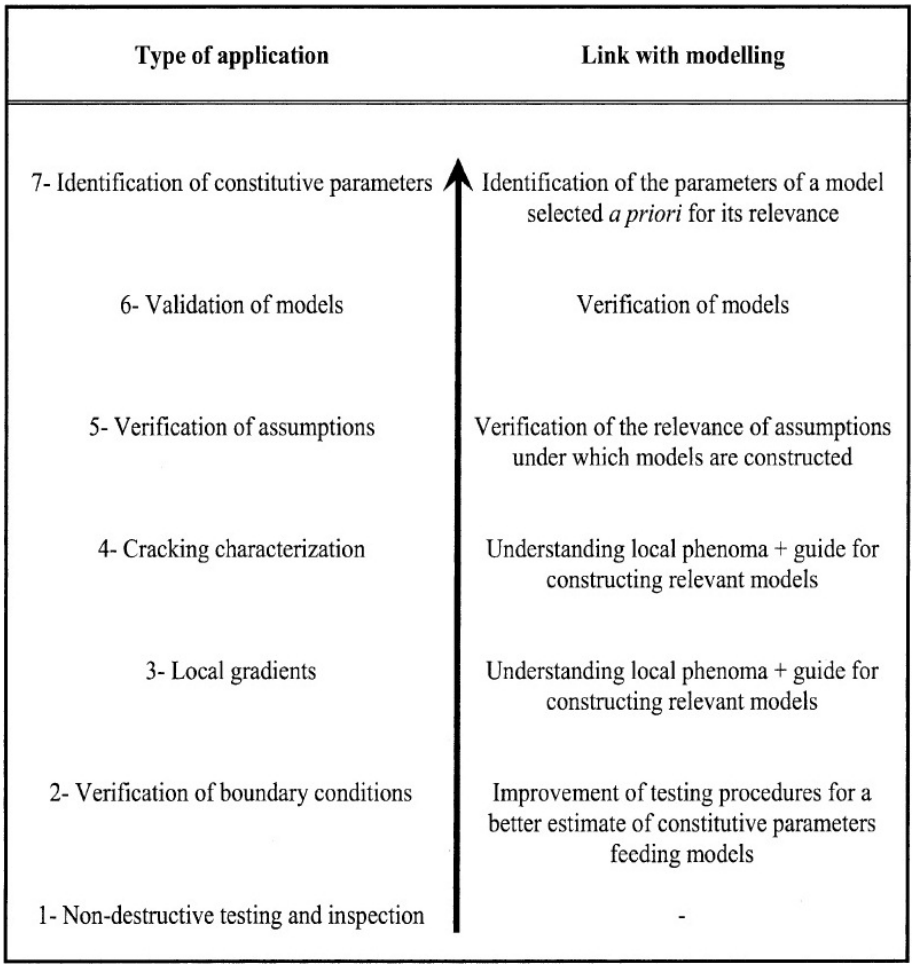

Figure 2.1: Link between full-field measurement and modelling activities from [18]

It has to be remarked that the limitation of full-field optical techniques lies in the hardware: spatial and temporal resolution depend on the spatial sensitivity and sampling rate of the imaging sensor. The constant improvement of such devices increases the speed and decreases the scale of the strains that can be observed with full-field optical techniques.

This chapter deals with the application of full-field optical strain measurement techniques to material characterisation. To acquire adequate images to perform displacement and strain measurement some important factors has to be taken into account. Furthermore both the techniques used during this research are affected by common issues that might cause error in the outputs:

- DIC requires a correct specimen surface preparation to produce a speckle pattern that ensures the correlation to be correctly performed. DIC requires dedicated software to be performed, in this research DaVis 8.1.4 is used. The correct correlations parameters, i.e. subset and step size, have to be selected when performing the correlation. It is also important to organise the experimental apparatus in a way that allows to minimise the systemic noisiness.
- GM requires a suitable grid pitch selection and its correct deposition on the specimen. Furthermore the experimental set-up requires precise alignment and magnification to be able to acquire images suitable to perform displacement and strain calculation. A code suitable to extract data for material characterisation from uniform strain fields, based on the GM processing code provided by Professor Pierron, has been developed and verified.

2.2 Image acquisition

2.2.1 Image acquisition equipment

Cameras

The various model of cameras used in this project are listed in Table 2.1 along with their characteristics. An explanation of the two different types of imaging sensors, Charge Coupled Device (CCD) and Complementary Metal Oxide Semiconductor (CMOS), and their relevance for image acquisition at high speed will be given in Section 3.4.1.

The AVT Manta cameras where used to define the measurement procedures for DIC and GM and to perform all the quasi-static experiments of this research. Redlake Motion Pro camera was used in the early stage of this project to define the experimental procedure on Instron VHS. The Photon cameras were provided by the EPSRC Instrument Pool, Airbus and DSTL. It was also possible to use pairs of Photron SA1, SA3 and SA5 for stereo imaging. These cameras were used, accordingly to their suitability and availability, to perform the validation experiments described in Chapter 4 and the material characterisation experiments of Chapter 5.

Table 2.1: Cameras used in this project

Manufacturer	Model	Sensor	Dinamic Range [bit]	Pixel Size [µm]	Frame Rate [kHz]		Resolution [pixel]
Allied Vision Technologies	Manta G-504	CCD	12	3.45	0.009		2542x2056
Redlake	Motion Pro X3	CMOS	8	12	1	at	1280x1024
					64	at	1280x16
Photron	SA3	CMOS	12	17	1	at	1024x1024
					120	at	128x16
Photron	SA1	CMOS	12	20	5.4	at	1024x1024
					675	at	64x16
Photron	SA5	CMOS	12	20	7	at	1024x1024
					1000	at	64x16

Illumination

During this research different types of illumination systems were used:

- **Halogen lamps** This kind of spotlight consists of a 1250 W halogen lamp, the light is also equipped with a cooling fan.
- **Fiber optic illuminator** This illumination system consists of a light bulb that is placed in an enclosed box, usually cooled by a fan, and has one or more diffusers connected to it via optical fibres. Two different systems are used:
  - Fiber-Lite PL-900 fibre optic illuminator manufactured by Dolan-Jenner Industries equipped with a 150 W Quartz halogen light and two 1.5 $\times$110 mm rectangular diffuser
  - KL 1500 fibre optic illuminator manufactured by Schott equipped with a 150 W Quartz halogen light and two 5 mm diameter round diffuser.
- **LED light** An illumination system was built using 8 Osram Opto Semiconductors Oslon SSL high brightness and luminance LED and Tina-Pin-OSL Real Spot lenses. This system became available in a late stage of the project.

Issues concerning the specimen illumination and their effect on the strain measurement are discussed in Section 2.3.4 and 3.4.4.

2.2.2 Image acquisition for full-field optical techniques

When setting-up an imaging apparatus for full-field optical stain measurement techniques the following practical considerations have to be taken into account:

- **Focusing** The whole specimen surface should be properly imaged and focused. In order to correctly focus the camera, high lens aperture is used, allowing shallow Depth of field (DOF). The camera focus is adjusted to produce a sharp image. Finally the aperture is regulated to obtain an unsaturated image.
- **Gray scale distribution** It must be guaranteed that the image is acquired with a grey scale distribution suitable to perform the image correlation, i.e. the dynamic range of the camera has to be exploited at its best. In the first instance the saturation of the sensor dynamic range must be avoided. Furthermore the grey level distribution should be maximised over the dynamic range of the imaging sensor. To obtain a suitable grey scale distribution it is necessary to regulate the amount of light that is captured by the imaging sensor acting on the lens aperture diameter and on the shutter speed. For example the pixel count over the grey level for a dark, a saturated and a correct image are shown in Figure 2.2.

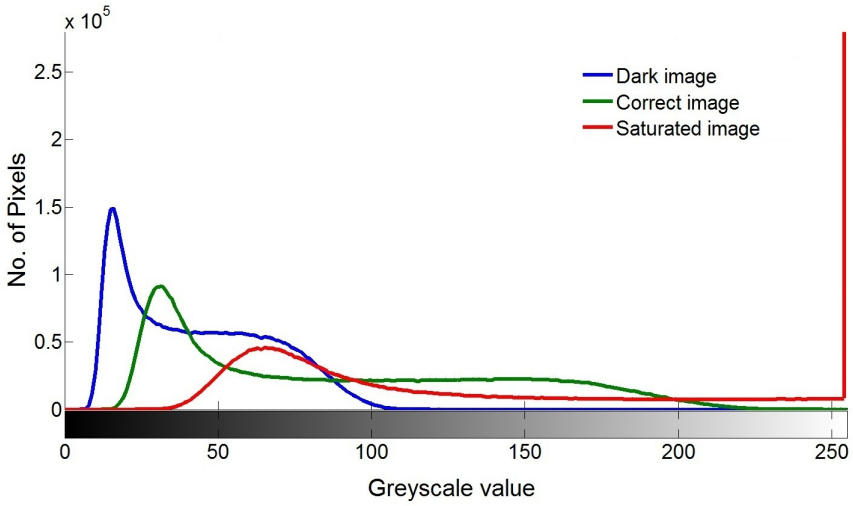

Figure 2.2: Pixel count over greyscale level

- **Depth of field** The depth of field is the distance between the farthest and closest object that appear acceptably sharp in an image. There are two reasons to maximise the DOF:
  - 2D techniques: the specimen may move out of plane during the test, therefore it is necessary to guarantee that the specimen surface stays in focus for post-processing of the images and obtain the displacement and strain fields.
  - Stereo imaging: the lens axis is not perpendicular to the specimen surface, as the cameras are placed at an angle. Therefore it is necessary that the DOF covers the whole specimen surface.

  When setting-up the imaging apparatus the main parameter that influences the DOF is the lens aperture diameter: reducing it will increase the DOF. At the same time, however, this also reduces the amount of light that is captured by the imaging sensor. Other ways to increase the DOF are reducing the focal length or increasing the stand-off distance. An example of the effect of the aperture diameter on the DOF is shown in Figure 2.3: a DIC target is imaged at an angle suitable for Stereo DIC image acquisition.

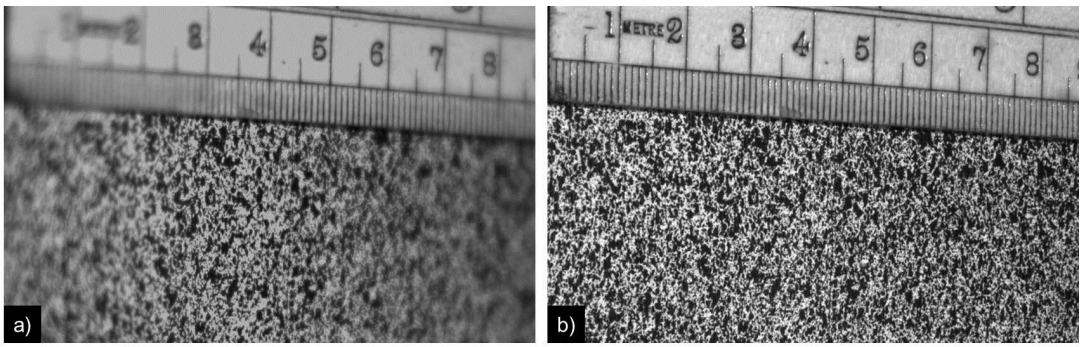

Figure 2.3: Different depth of field obtained with different aperture diameter:
a) f/1.8;
b) f/22

- **Shutter speed** The exposure time, or shutter speed, is the length of time an optical sensor takes in capturing the image. The maximum achievable exposure time is the inverse of the frame rate. It determines how sharp or blur free an image is. Particularly for the high speed imaging it is important to maximise the shutter speed to reduce the blurriness of the image. Reducing the exposure time also reduces the amount of light that is captured by the imaging sensor. An example of the effect of the shutter speed on the image blurriness is shown in Figure 2.4 of a DIC target rotating at 750 rpm imaged at 50 frame per second.

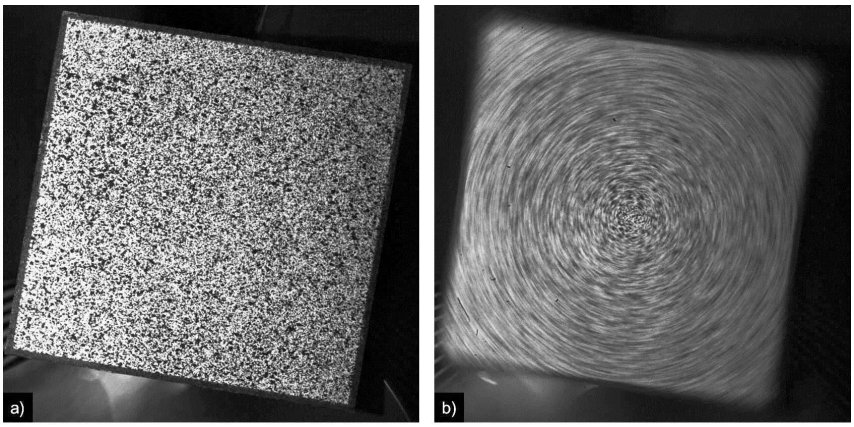

Figure 2.4: Example of images taken with different shutter speed:
a) Exposure time = 10 µs;
b) Exposure time = 1 ms

- **Illumination** To obtain an image suitable to perform the full-field optical strain measurement technique the ideal solution is to minimise both the lens aperture diameter and the exposure time. This, however, reduces the number of photons that impinge on the sensors. It is therefore necessary to maximise the light intensity. To guarantee correct imaging it is necessary to set-up the

light source to uniformly illuminate the specimen surface avoiding shadows. The usage of incandescent type lamps to illuminate the target might lead to distortion of the recorded images caused by convection waves. Moreover the target might be heated by radiation and behave differently than at room temperature. Furthermore specular reflections of the light on the specimen surface might cause biased images to be acquired. These problems can be mitigated if cold light sources are used. The issues regarding the specimen illumination are discussed in detail below in Section 2.3.4 and 3.4.4.

- **Resolution / Frame rate** In high speed cameras, reducing the sensor resolution, i.e. reducing the number of active sensors in the sensing array, allows recording at an higher frame rate. Particularly for high speed testing, it is necessary to obtain an ideal compromise between the two values. On one side it is necessary to record the images with a frame rate suitable to collect a sufficient number of data point to obtain a meaningful stress-strain curve. On the other side images with a number of pixels useful to perform the full-field strain measurement optical techniques must be acquired.

2.3 Digital image correlation

2.3.1 Theoretical background

DIC is a full-field, non interferometric optical technique able to provide displacement and strain over a surface. A typical DIC experimental set-up comprises one or two high resolution cameras, an interface that triggers the cameras and connects them to a computer used to control the measurements and process the images. If a single camera is used DIC will give two dimensional displacement and strain fields, this technique is called 2D DIC. When two cameras are used in stereo vision, capturing pairs of images of the specimen, DIC gives a three dimensional displacement field, this technique is called Stereo DIC. An overview of the correlation methodology is presented in Figure 2.5.

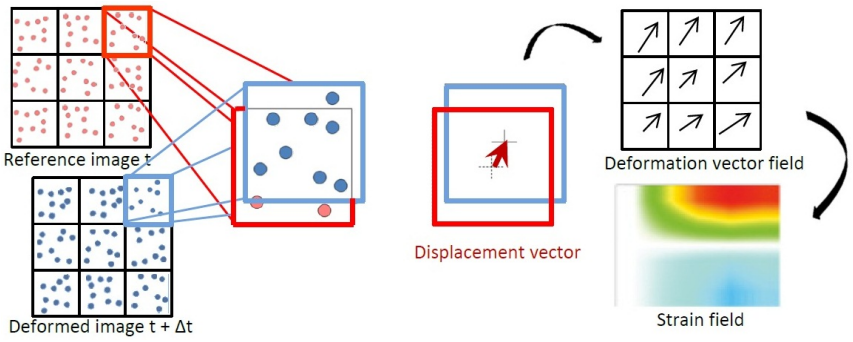

Figure 2.5: Schematic of DIC process, from [22]

DIC measurements are performed following these steps:

1. Specimen preparation. The specimen surface has to be prepared with a stochastic speckle pattern, typically with an aerosol spray paint, ensuring good adhesion with the specimen's surface. For the correct functioning of the correlation algorithm a random grey level distribution is necessary.

2. Set-up of the image recording system. This has to be done ensuring that:
   - The imaging sensor and the speckle pattern must remain parallel to each other during the whole test time.
   - An adequate illumination must be provided, particularly with high frame rate cameras.
   - For 2D DIC geometric distortion in the imaging system, caused by camera misalignment and lens distortion must be minimised, as explained in Section 2.5.

3. Record calibration and reference images:
   - For Stereo DIC calibration images of a calibration object, with a carefully machined and dotted surface, are needed to associate a dimension to the pixel size and to identify the relative position between the cameras and the specimen.
   - For 2D DIC it is necessary to take a picture with a dimensional reference to scale the images.
   - The reference picture, n_0, is the speckle distribution on the unloaded specimen.

4. Record images of the specimens while the load is applied: sampling frequency and area of interest are dependent on the experiment goal.

5. Image processing with a computer program to evaluate displacement and strain field. The program can work with a commercial or an in house software. The procedure can be summarised as follows:
   a) The recoded images are subdivided into an array of interrogation cells, or subsets, that provide the full-field data map over the specimen surface. Considering subsets that include a higher number of pixels, and therefore of speckles, will increase the measurement accuracy but will reduce the spatial resolution of the measurement.
   b) The grey level distribution of the speckle pattern in each subset of the deformed image n is compared with the one of the reference image n_0.

A correlation function value is generated, from the grey levels, for each subset to determine the matching between the deformed and the reference subset. Among the various correlation criteria it is worth mentioning the Cross Correlation, Equation 2.1 and the Sum of Squared Difference criteria, Equation 2.2.

$$C_{CC} = \sum_{i=-N}^{N} \sum_{j=-N}^{N} \left[f(x_i, y_j) \bullet g(x'_i, y'_j) \right] \tag{2.1}$$

$$C_{SSD} = \sum_{i=-N}^{N} \sum_{j=-N}^{N} \left[f(x_i, y_j) - g(x'_i, y'_j) \right]^2 \tag{2.2}$$

where $f(x, y)$ and $g(x', y')$ are the intensity or the grey scale of a pixel in the reference image and in the deformed image respectively.

c) The morphological changes of the deformed subset are identified using a shape function. Shape functions can be of various order, from the zero-order, that considers a rigid translation of the subset, to second or higher order that consider complex subset deformations.

d) To increase DIC measurement accuracy with sub-pixel measurement of the correlation function, interpolation functions are used. Different interpolations methods can be used, Schreier *et. al* [23], after conducting a numerical study of displacement and strain obtained with different speckle patterns and sub-pixel interpolation methods, recommend cubic and cubic B-spline interpolation over linear and quadratic B-spline interpolation. Furthermore sub-pixel displacement accuracy can be achieved using coarse-fine searching [24], peak-finding [25], Newton-Rapson [26], Levemberg-Marquardt [23] etc.

A good review of the DIC methodology and principles can be found in the paper by Pan *et al.* [12], while a full description of image correlation application for shape, motion and deformation measurements with theoretical background and experimental application is illustrated in the book from Sutton *et al.* [15].

2.3.2 Specimen surface preparation for DIC

To correctly perform DIC the specimen surface has to be prepared with a random speckle pattern as explained in Section 2.3.1. The specimens were painted using spray paint from RS components:

1. A uniform white background is painted on the specimen surface;

2. Black speckles were sprayed over the white background exploiting the nebulisation effect of the spray can nozzle.

This techniques allowed a random black speckle pattern over a white surface to be obtained, as the one shown in Figure 2.6, with the right characteristics to perform DIC. It must be remarked here that similar results could have been obtained using white speckle pattern on a black background. A white background was chosen because it is believed to be helpful in high speed imaging, where the exposure time is short. Compared to a black background, a white one generates a brighter surface to be imaged, that reflects a higher number of photons towards the imaging sensor.

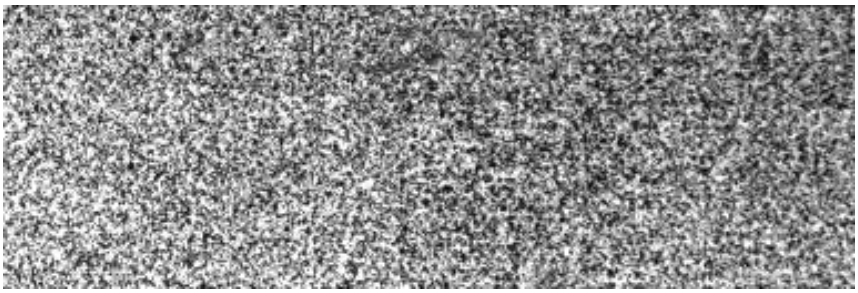

Figure 2.6: Random Speckle Pattern painted over a GFRP specimen

The targets to achieve when preparing a specimen surface for DIC are:

- Uniform speckle size;
- Uniformity in the speckle distribution.

In general the speckle size is dependent on the measurement purpose. A small speckle is desirable when imaging areas where strain concentration and high-order strain gradients are expected. When pure translation or uniform strains are expected larger speckle can be acceptable. A study about the average speckle size was carried out by Hung and Voloshin [27] who found that the ideal average size of the speckle in pixels is dependent on the average strain that has to be measured and its nature. Haddadi and Belhabib [28] demonstrated with rigid body motion tests that a small random pattern with a high number of speckles performs better than a coarser dotted pattern.

2.3.3 Effect of the software correlation parameters on measurement resolution

The accuracy of DIC measurements depends on the correlation parameters: the shape function [29], the sub-pixel interpolation function [23] and subset size [30]. The DaVis 8.1.4 software from LaVision was used to perform DIC. This software

uses a least squares matching correlation function, a first order shape function and a sixth order spline interpolation function for the sub-pixel accuracy. Ultimately the user has the possibility to customise the following parameters to perform the correlation:

- Subset size: the size, in pixels, of the interrogation cells over witch the image correlation is performed;
- Step size: the distance, in pixel, between the centre of the interrogation cells;

In general modifying the correlation parameters, i.e. subset and step size, to improve the spatial resolution leads to an increase in the noise level [31]. Using a larger subset size increases the strain measurement precision because there are more features, i.e. speckles, to track within each cell, but it also lowers the spatial resolution. Similarly reducing the step size increases the spatial resolution but also the noise level. To demonstrate the effects of subset and step size on the strain resolution a correlation has been run on a sequence of steady images of a target prepared with black speckles over a white background. Figure 2.7 shows the results for the set of images acquired using a AVT Manta CCD based camera, while Figure 2.8 for a Photron SA3 CMOS based camera. The resolution is calculated as the standard deviation of the strain data, as will be explained in Section 2.5, to have a first evaluation of the strain resolution. It has to be remarked that the analysis of strain in the x and the y direction produced similar results. The step size is here expressed as percentage of the considered subset size.

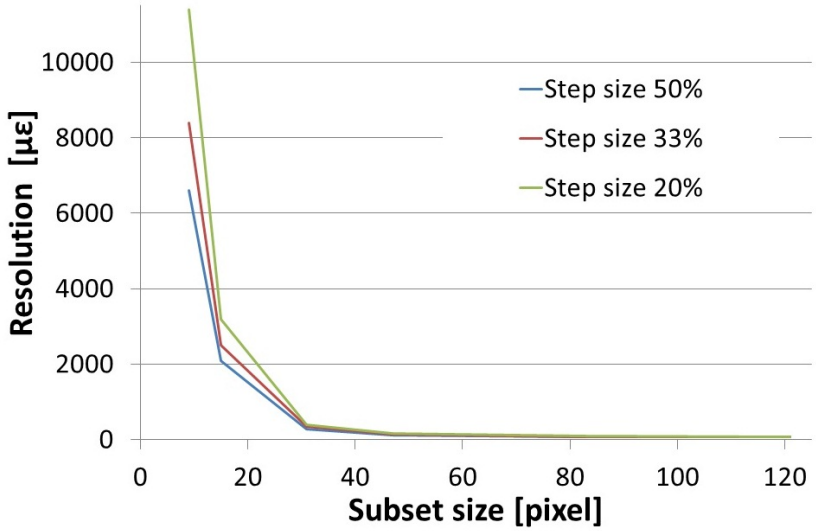

Figure 2.7: Strain resolution as function of subset and step size in a CCD sensor

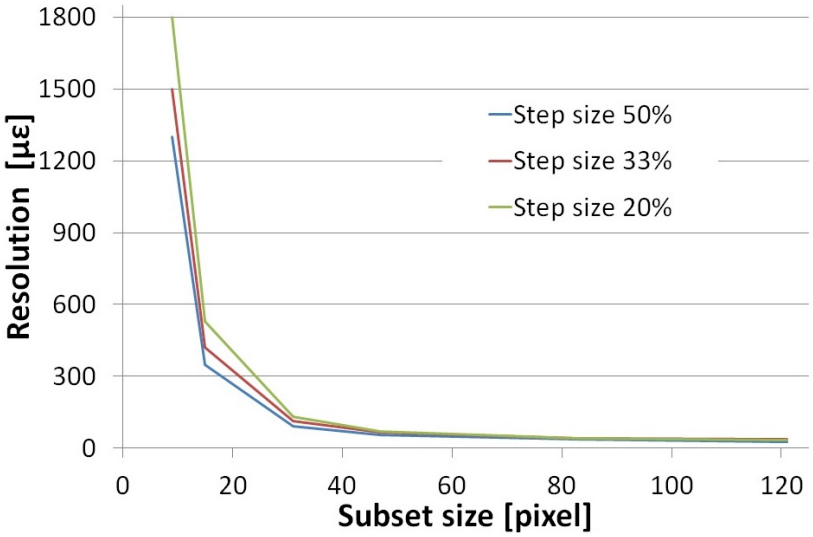

Figure 2.8: Strain resolution as function of subset and step size in a CMOS sensor

It can be observed that using a small subset size increases the noisiness of the data. This is due to the fact that the subset size is comparable with the speckle size, compromising the quality of the correlation, and by statistical effects caused by a higher number of data points. The software developer suggests to use a subset size that includes at least three features. Increasing the subset size leads to a reduction in the noisiness and improves the strain resolution. The benefit of increasing the subset size become negligible after a certain limit. The usage of large subset size is therefore not beneficial because it reduces the number of data points available for the data post process. It is therefore necessary to find a compromise between spatial resolution and error. The CCD sensor, with a higher number of pixels and a smaller pixel size, allows to obtain a significantly higher number of data points over the same area than the CMOS. The higher resolution of the CMOS based camera can be explained by the bigger physical size of the pixel detector. A way to increase the number of data points without significantly affect the resolution is to reduce the step size.

2.3.4 DIC measurement procedure definition

A series of preliminary tests were run to evaluate the resolution of the data acquisition system for quasi-static characterisation tests and define the ideal data acquisition procedure. The set-up information obtained in the quasi-static tests will also be applied to high speed tests in Section 3.4. In this set of preparatory tests a specimen made of MTM58FRB/HS(24K)-450-38%RW (Umeco) CFRP pre-preg material stacked in a unidirectional lay-up was used. The nominal width of the

specimen was 25 mm and the thickness 1.5 mm. The surface of the specimen was prepared with a black speckle pattern over a white background on both sides of the gauge length. The test were run on a Series 5560, servo-electric, dual column, Instron test machine at a cross-head displacement speed of 0.1 mm/s. The image acquisition was done using four Manta G-504 cameras controlled with a LabView code. The code was designed to simultaneously acquire four images and two voltage signals from a National Instrument USB-6009 data acquisition device. One channel was used to record the force signal out of the load cell and the other the cross-head displacement. The code was tested with a chronometer and it is proven to have an accuracy of 1 ms with a maximum sampling frequency of 1.3 frame per second.

Image and data acquisition

The first step is to assess if the four cameras have the same characteristic regarding the noise level and obtainable strain resolution. 2D DIC is performed at the same time on the front and back of the specimen. The specimen is illuminated using two Schott KL 1500 fibre optic illuminators, each one equipped with two light diffusers. The fibre optic illuminators ensure that the specimen surface is not heated, the devices are placed in a position that ensures that no heat waves are distorting the acquired images. A schematic of the experimental set-up is shown in Figure 2.9.

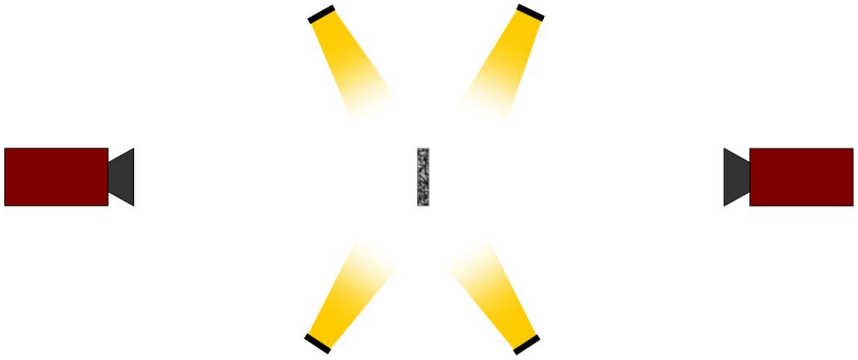

Figure 2.9: Schematic of the experimental set-up for 2D DIC

The characteristics of the measurements performed on the front and the back of the specimen are reported in Tables 2.2 and 2.3.

Table 2.2: Imaging characteristics for 2D DIC on the front of the specimen for individual cameras evaluation

Technique	DIC
Software	DaVis 8.0.8
Subset size	31 x 31 pixels
Step size	10 pixels
Camera	AVT Manta G-504
Lens	Sigma 105 mm f/2.8
Resolution	2452 x 2056 pixels
Field of view	92.5 x 77.6 mm
Frame rate	0.2 Hz
Imaging distance	$\simeq$ 1200 mm
Spatial Resolution	0.377 mm

Table 2.3: Imaging characteristics for 2D DIC on the back of the specimen for individual cameras evaluation

Technique	DIC
Software	DaVis 8.0.8
Subset size	31 x 31 pixels
Step size	10 pixels
Camera	AVT Manta G-504
Lens	Sigma 105 mm f/2.8
Resolution	2452 x 2056 pixels
Field of view	114.1 x 95.7 mm
Frame rate	0.2 Hz
Imaging distance	$\simeq$ 1500 mm
Spatial Resolution	0.465 mm

The spatial resolution is the distance between two data points, i.e. the step size. The resolutions for displacement and strain, calculated as standard deviation of the displacement and the strain fields obtained performing the correlation of two images of the unloaded specimen, are shown in Table 2.4.

Table 2.4: Measurement resolution

	Front		Back	
	Displacement [pixels]	Strain [mε]	Displacement [pixels]	Strain [mε]
Camera 1	0.017	0.40	0.013	0.40
Camera 2	0.015	0.34	0.008	0.34
Camera 3	0.016	0.42	0.010	0.37
Camera 4	0.016	0.36	0.007	0.30

Typical strain maps used to evaluate the noise levels for the 2D DIC performed on the front and on the back of the specimen are shown in Figures 2.10 and 2.11.

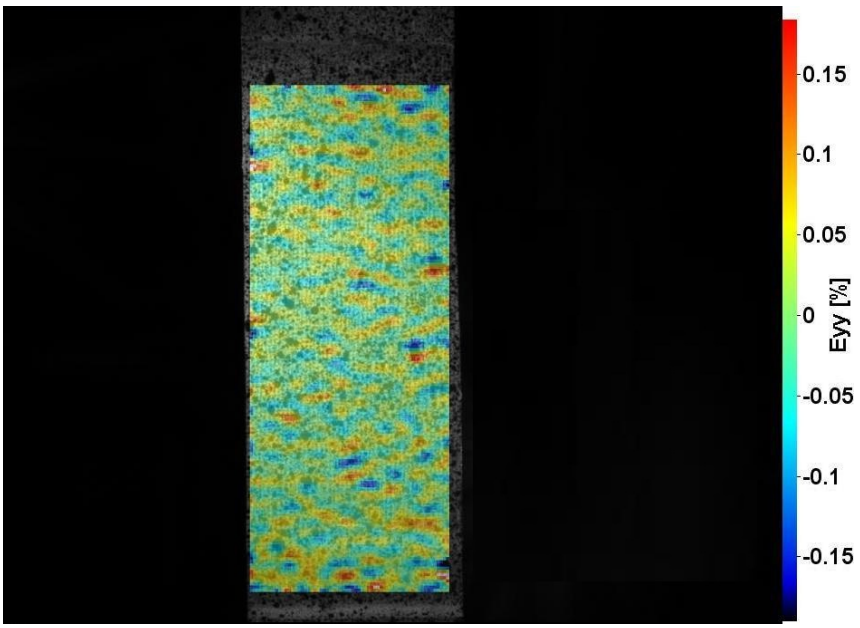

Figure 2.10: Strain map used to evaluate the noise level of 2D DIC on the front of the specimen

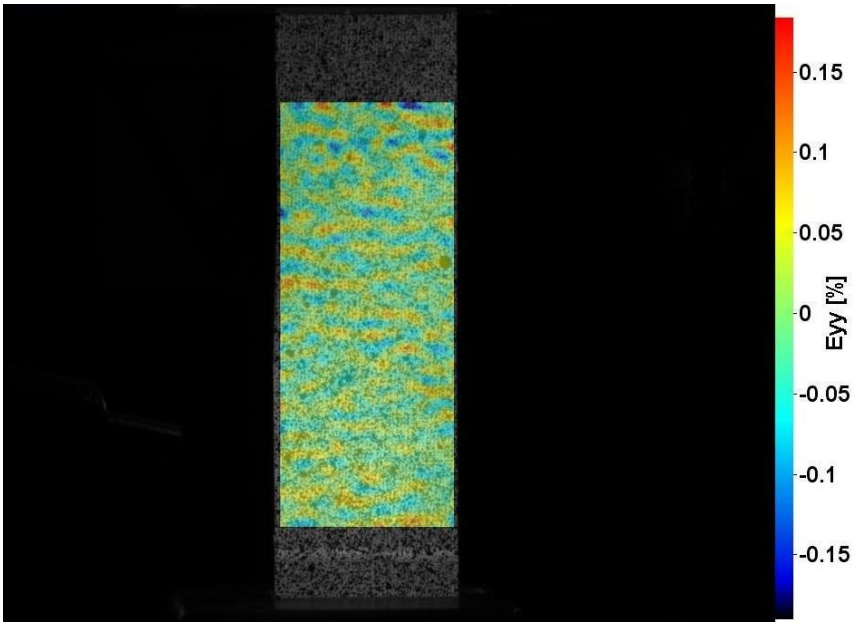

Figure 2.11: Strain map used to evaluate the noise level of 2D DIC on the back of the specimen

The Stress-Strain curves obtained from the 2D DIC with all the cameras used on the front and back of the specimen are shown in Figures 2.12 and 2.13.

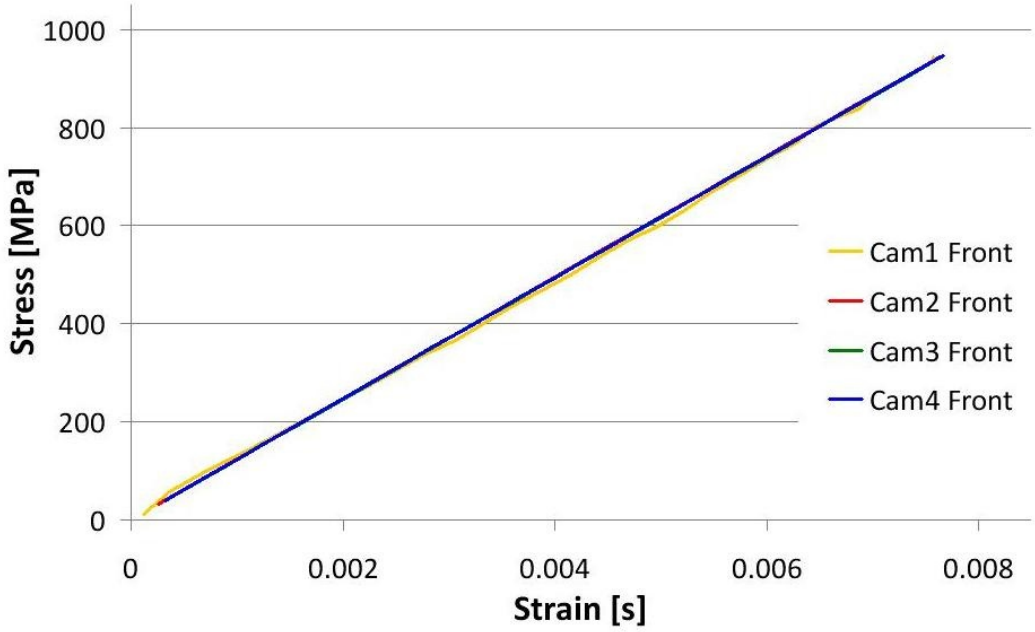

Figure 2.12: Stress-Strain curve from the front of the specimen obtained with 2D DIC

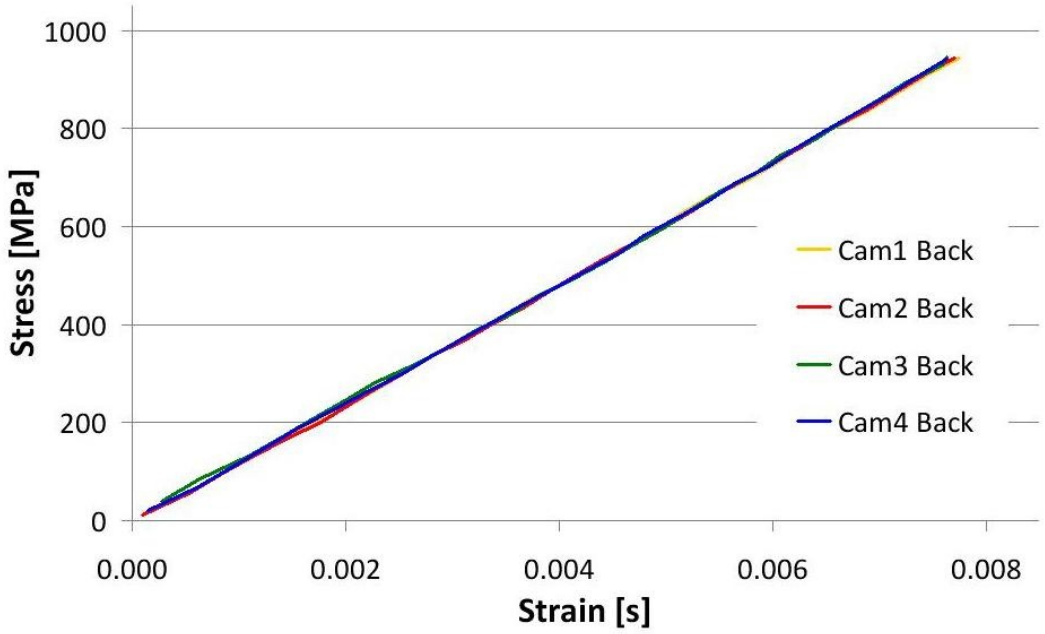

Figure 2.13: Stress-Strain curve from the back of the specimen obtained with 2D DIC

The obtained Young's Moduli are summarised in Table 2.5, along with the Coefficient of variation (CV).

Table 2.5: Young's Moduli in GPa from 2D DIC for cameras evaluation

	Front	Back
Camera 1	122.5	124.0
Camera 2	123.6	123.1
Camera 3	123.4	123.5
Camera 4	122.5	123.5
Average	123.00	123.53
CV [%]	0.47	0.30
Average	123.26	
CV [%]	0.43	

From the evaluation of the single cameras performed by conducting tensile tests on unidirectional carbon-epoxy specimens, and measuring the strain with 2D DIC it can be concluded that the cameras have the same or very similar performance, giving Young's moduli with a CV lower than 1%. The tests are run keeping the same boundary conditions. The noise levels of displacement and strain are substantially the same, i.e. in the same order of magnitude, for all the cameras from the correlation performed on the front and on the back of the specimen, as shown in Table 2.4.

Specimen illumination

The cameras are then tested to evaluate their performances when used to acquire images for Stereo DIC. The cameras are rotated around the specimen testing various combinations, as shown in Table 2.6.

Table 2.6: Positions of the cameras in the tested configurations for stereo DIC evaluation

	Cameras			
	Camera 1	Camera 2	Camera 3	Camera 4
Combination 1	Front Right	Back Left	Back Right	Front Left
Combination 2	Back Right	Back Left	Front Right	Front Left
Combination 3	Back Right	Front Right	Back Left	Front Left
Combination 4	Back Right	Front Right	Front Left	Back Left
Combination 5	Front Left	Front Right	Back Right	Back Left
Combination 6	Front Left	Back Right	Front Right	Back Left

The camera combinations are chosen ensuring that each camera and all the possible couples of cameras are viewing at least once the front and the back of the specimen. Placing the same combination of cameras on the same side of the specimen just swapping their position is considered redundant. A schematic of the experimental set-up is shown in Figure 2.14. At this stage the light source is still provided by two Schott KL 1500 fibre optic illuminators, as for the 2D DIC tests.

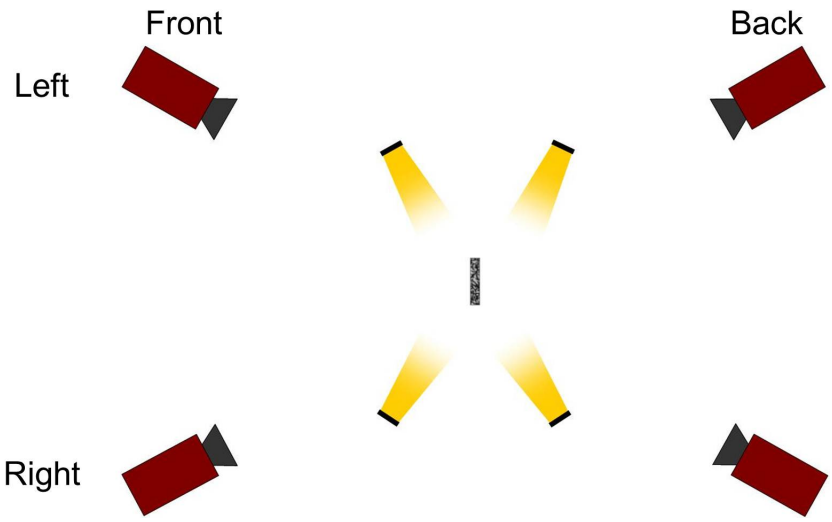

Figure 2.14: Schematic of the experimental set-up for Stereo DIC with Schott KL 1500 fibre optic illuminator

The characteristics of the measurements performed on the front and the back of the specimen are reported in Tables 2.7 and 2.8.

Table 2.7: Imaging characteristics for Stereo DIC on the front of the specimen

Technique	DIC
Software	DaVis 8.0.8
Subset size	31 x 31 pixels
Step size	10 pixels
Camera	AVT Manta G-504
Lens	AF NIKKOR 50 mm
Resolution	2452 x 2056 pixels
Field of view	110 x 95 mm
Frame rate	1 Hz
Spatial Resolution	0.435 mm

Table 2.8: Imaging characteristics for Stereo DIC on the back of the specimen

Technique	DIC
Software	DaVis 8.0.8
Subset size	31 x 31 pixels
Step size	10 pixels
Camera	AVT Manta G-504
Lens	AF NIKKOR 50 mm
Resolution	2452 x 2056 pixels
Field of view	105 x 93.5 mm
Frame rate	1 Hz
Spatial Resolution	0.444 mm

The Root mean square (RMS) of the fit, an indicator of the quality of the calibration, are summarised in Table 2.9. The RMS of the fit is automatically calculated by

the DaVis software when generating the calibration file, and represents the accuracy in the calculation of the relative position between the two cameras and the target. The software manufacture recommend a value lower than 0.5 pixel to be obtained to classify the calibration as accurate

Table 2.9: RMS of the fit in pixel

	Front	Back
Combination 1	0.397	0.296
Combination 2	0.294	0.380
Combination 3	0.297	0.348
Combination 4	0.299	0.267
Combination 5	0.386	0.303
Combination 6	0.329	0.300

It can be observed that all the tested configurations present a RMS of the fit of the same order of magnitude and therefore their results can be compared to assess the quality of the evaluated strain results.

The displacement and strain resolution are summarised in Table 2.10.

Table 2.10: Resolution for the different cameras configurations

	Front		Back	
	Displacement [pixels]	Strain [mε]	Displacement [pixels]	Strain [mε]
Combination 1	0.125	0.35	0.014	0.172
Combination 2	0.071	0.13	0.019	0.065
Combination 3	0.046	0.12	0.024	0.073
Combination 4	0.046	0.16	0.012	0.073
Combination 5	0.073	0.14	0.023	0.068
Combination 6	0.025	0.11	0.022	0.054

The mismatch in the displacement and strain resolution between the various combination is attributable to the to the chosen illumination approach, that causes biased images to be acquired. Typical strain maps used to evaluate the noise levels for the Stereo DIC performed on the front and on the back of the specimen are shown in Figures 2.15 and 2.16.

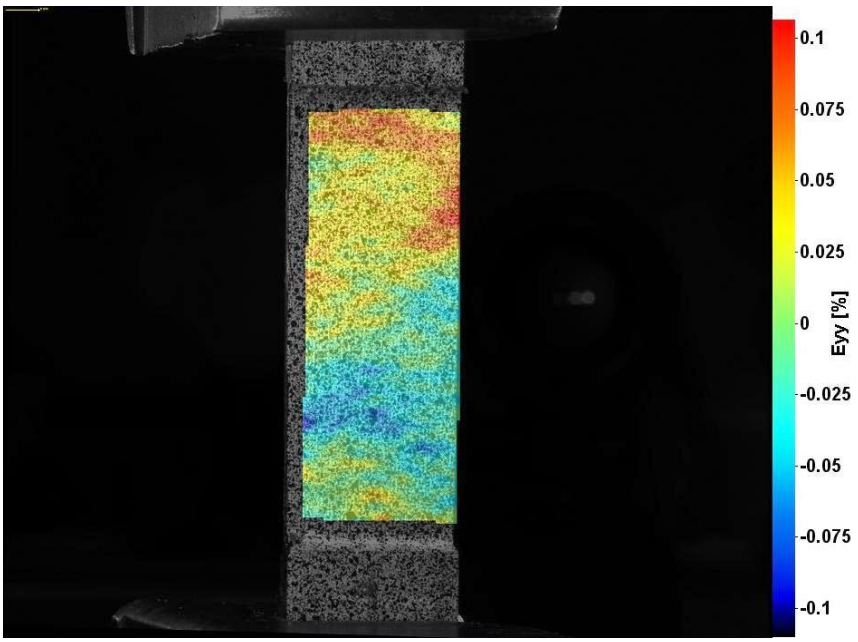

Figure 2.15: Strain map used to evaluate the noise level for Stereo DIC on the front of the specimen

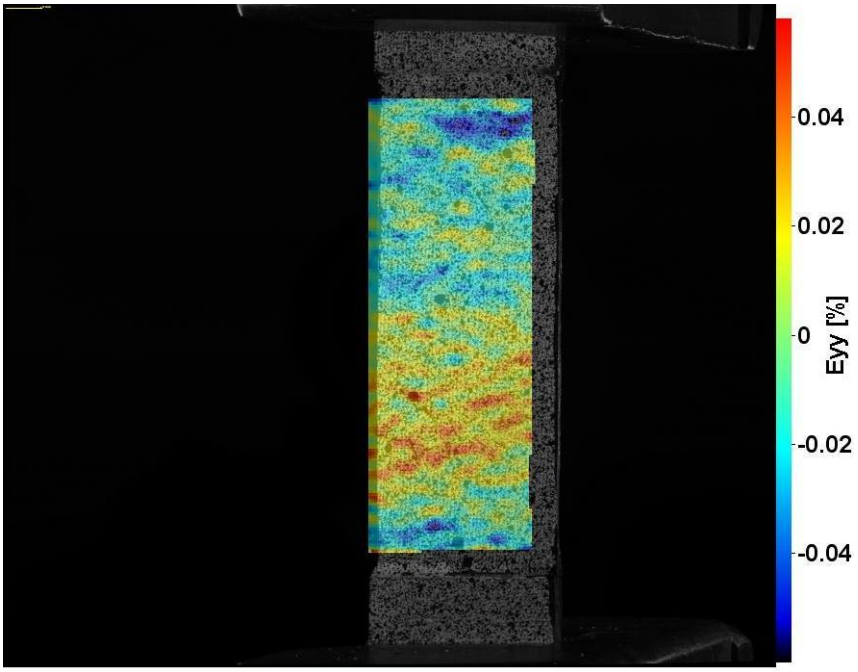

Figure 2.16: Strain map used to evaluate the noise level for Stereo DIC on the back of the specimen

Observing both figures it is evident the strain maps do not have the form of a white noise: regions of positive and negative strains can be identified.

The Stress-Strain curves obtained from the Stereo DIC for all cameras combination are shown in Figures 2.17 and 2.18.

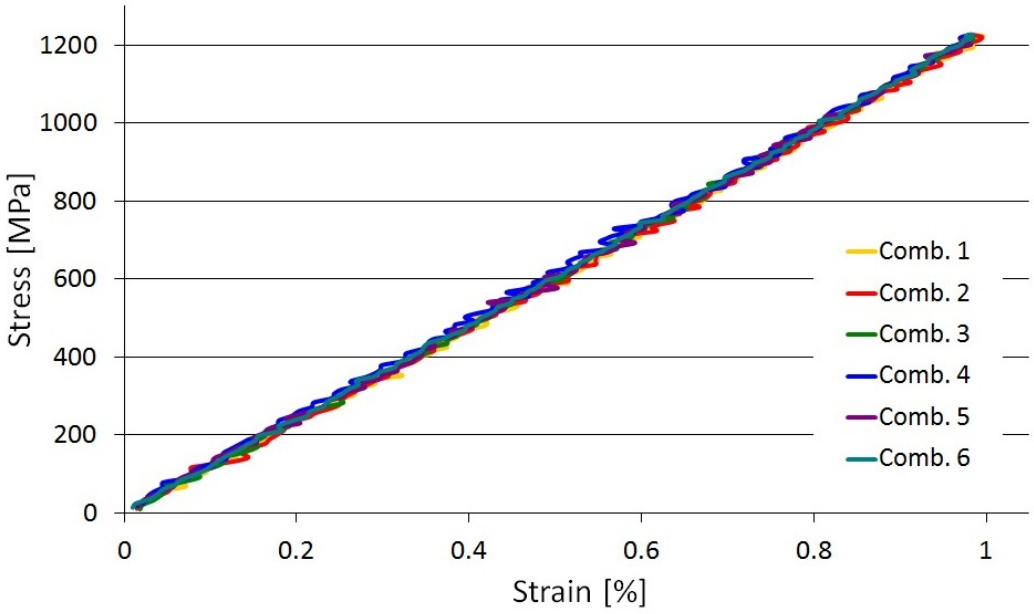

Figure 2.17: Stress-Strain curve from the front of the specimen obtained with Stereo DIC

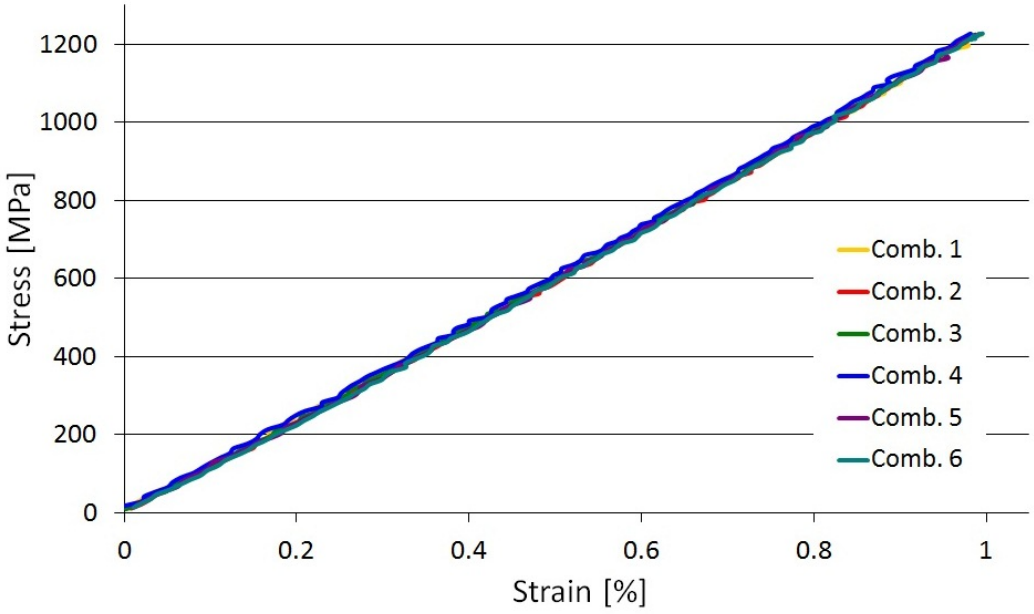

Figure 2.18: Stress-Strain curve from the back of the specimen obtained with Stereo DIC

The obtained Young's Moduli are summarised in Table 2.11.

Table 2.11: Young's Moduli in GPa from Stereo DIC for cameras evaluation

	Front	Back
Combination 1	123.3	122.5
Combination 2	123.4	123.4
Combination 3	124.3	123.7
Combination 4	123.4	123.7
Combination 5	123.3	123.3
Combination 6	124.1	124.1
Average	123.63	123.45
CV [%]	0.36	0.44
Average	123.54	
CV [%]	0.39	

Observing the Stress-Strain curves shown in Figures 2.17 and 2.18 it is clear that, even if the the Young's Moduli summarised in Table 2.11 are in agreement with the values obtained from the 2D DIC, the curves are affected by a high level of noisiness. It is believed that the noisiness of the strain data is caused by specular reflection on the specimen surface of the light from the illuminator light source to the camera CCD sensor. Furthermore the light used to illuminate the front of the specimen directly hit the CCD sensor of the camera imaging the back of the specimen. It is therefore necessary to modify the experimental set-up to reduce the noisiness of the strain data caused by the illumination of the specimen.

It can be concluded that the different configurations give the moduli results, with a low CV, the cameras can therefore be used with confidence in any position of the front and back Stereo DIC imaging acquisition set-up. The quality of the data and the noisiness can be reduced modifying the specimen illumination.

Finalisation of the imaging techniques for two sided Stereo DIC

To confirm that the noisiness of the data can be reduced, a new experimental set-up, shown in Figure 2.19, was used.

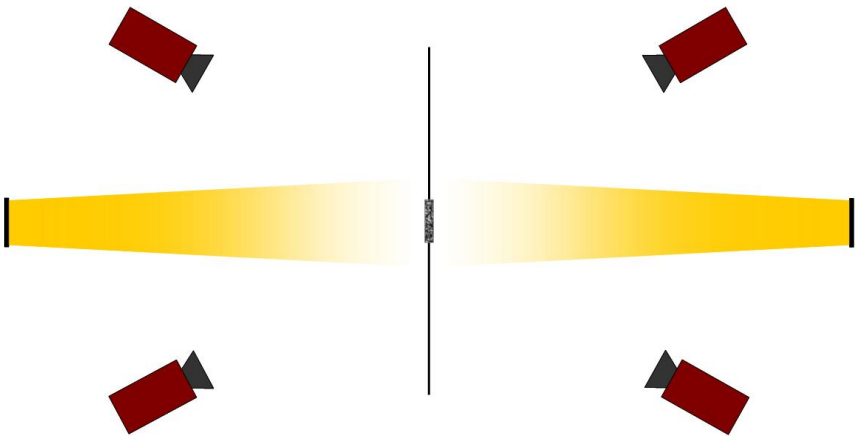

Figure 2.19: Schematic of the experimental set-up for Stereo DIC with single light source, light screens are placed on the side of the specimen.

This configuration allows the reduction of specular reflection of the light to the CCD sensors on the cameras. The light source is an incandescence spot light but the distance from the specimen, about 2000 mm, is great enough to avoid heating the specimens. Positioning the light behind the cameras, ensures that no heat waves are interfering with the imaging process creating distortion of the images. Furthermore a screen has been placed on the sides of the specimens to avoid direct light to hit the imaging sensors.
At this stage different combinations of shutter speed and lens aperture are tested, as summarised in Table 2.12.

Table 2.12: Different imaging configuration for finalisation of the Stereo DIC set-up

	Aperture f-ratio	Shutter time µs
Configuration 1	f/4	1750
Configuration 2	f/8	7500
Configuration 3	f/16	25000
Configuration 4	f/22	75000

The characteristics of the measurements performed on the front and the back of the specimen are reported in Tables 2.13 and 2.14.

Table 2.13: Imaging characteristics for Stereo DIC on the front of the specimen for methodology finalisation

Technique	DIC
Software	DaVis 8.0.8
Subset size	31 x 31 pixels
Step size	10 pixels
Camera	AVT Manta G-504
Lens	AF NIKKOR 50 mm
Resolution	2452 x 2056 pixels
Field of view	95 x 78 mm
Frame rate	0.2 Hz
Spatial Resolution	0.384 mm

Table 2.14: Imaging characteristics for Stereo DIC on the back of the specimen for methodology finalisation

Technique	DIC
Software	DaVis 8.0.8
Subset size	31 x 31 pixels
Step size	10 pixels
Camera	AVT Manta G-504
Lens	AF NIKKOR 50 mm
Resolution	2452 x 2056 pixels
Field of view	98 x 80 mm
Frame rate	0.2 Hz
Spatial Resolution	0.387 mm

The displacement and strain resolution are summarised in Table 2.15.

Table 2.15: Resolution for the different imaging combinations

	Front		Back	
	Displacement [pixels]	Strain [mε]	Displacement [pixels]	Strain [mε]
Configuration 1	0.005	0.11	0.023	0.37
Configuration 2	0.005	0.19	0.026	0.29
Configuration 3	0.008	0.27	0.010	0.29
Configuration 4	0.009	0.14	0.021	0.22

Typical strain maps used to evaluate the noise levels for the Stereo DIC performed on the front and on the back of the specimen are shown in Figures 2.20 and 2.21.

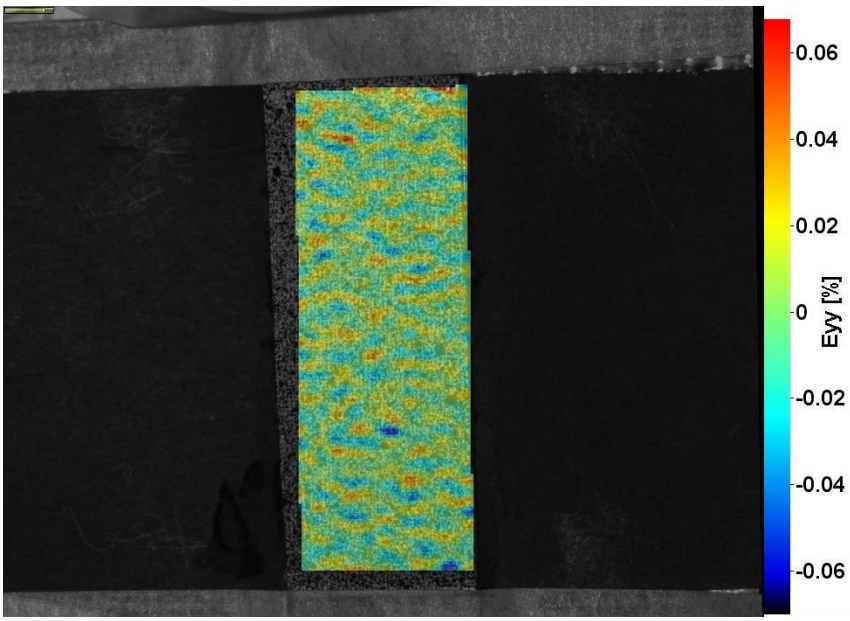

Figure 2.20: Strain map used to evaluate the noise level for Stereo DIC on the front of the specimen

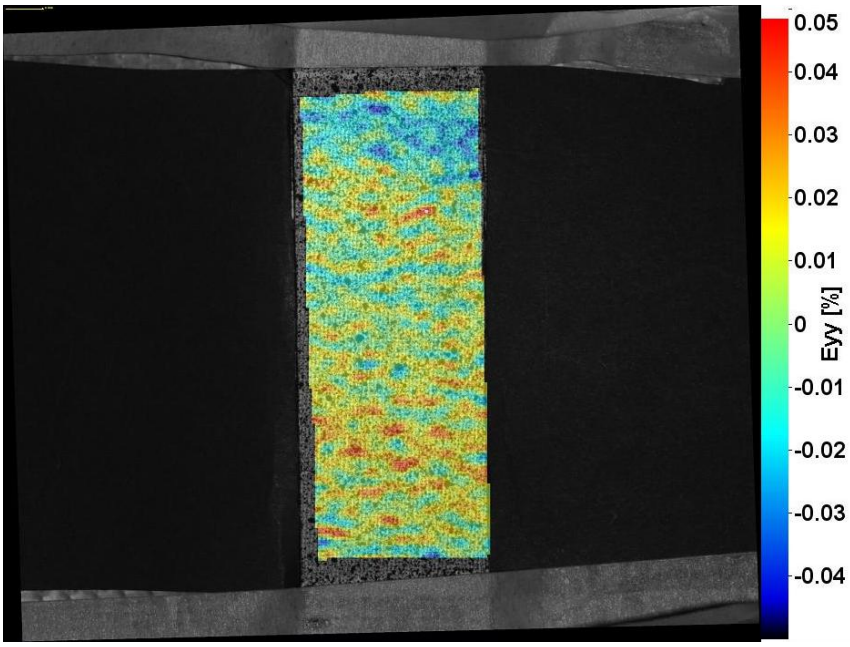

Figure 2.21: Strain map used to evaluate the noise level for Stereo DIC on the back of the specimen

In Figures 2.20 and 2.21 the strain noisiness is distributed as white noise. This means that the illumination of the specimen is not affecting the image acquisition.

The Stress-Strain curves obtained from the Stereo DIC for all cameras combination are shown in Figures 2.22 and 2.23.

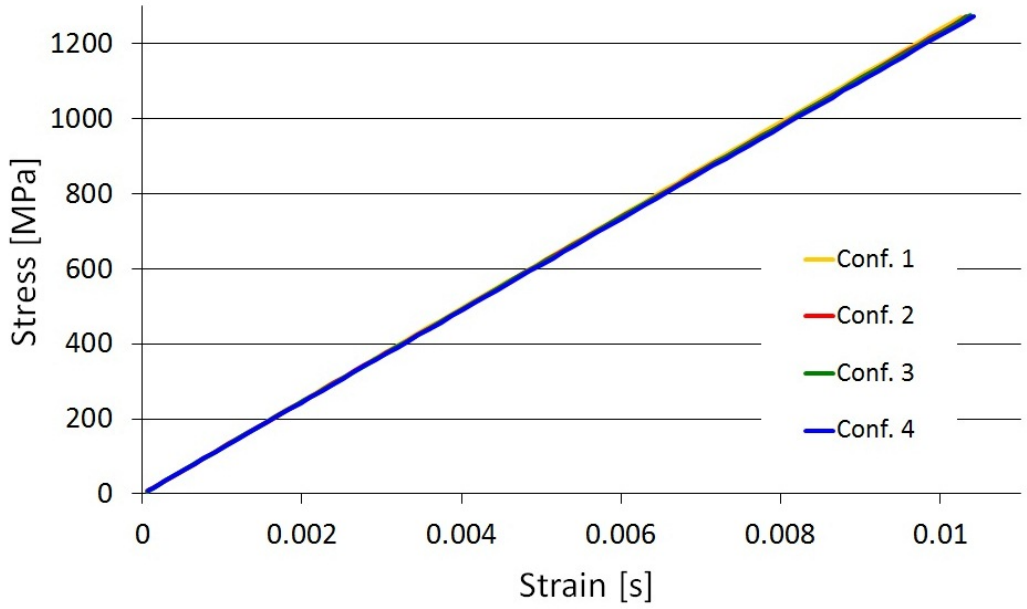

Figure 2.22: Stress-Strain curve from the front of the specimen obtained with Stereo DIC

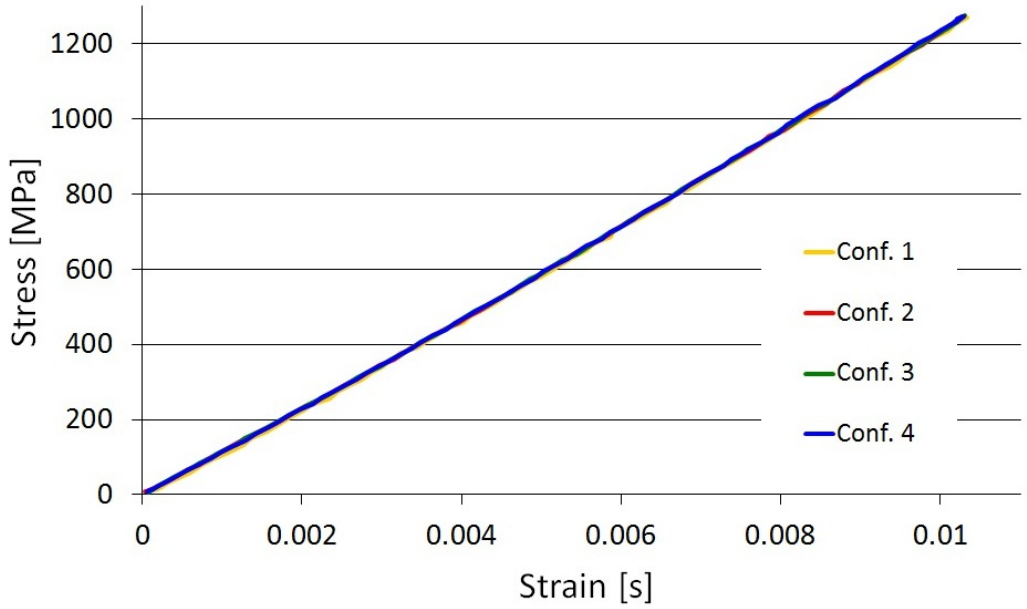

Figure 2.23: Stress-Strain curve from the back of the specimen obtained with Stereo DIC

The obtained Young's Moduli are summarised in Table 2.16.

Table 2.16: Young's Moduli in GPa from Stereo DIC for evaluation of the new illumination set-up

	Front	Back
Configuration 1	123.8	123.6
Configuration 2	123.1	123.7
Configuration 3	122.9	124.0
Configuration 4	122.3	124.1

Observing the measurement resolution, the strain maps and the stress strain curves it can be concluded that this experimental set-up reduces the image bias and consequently the noisiness of the data, especially as much as regards the stress-strain curves. Furthermore for quasi-static tests the lens aperture and and shutter speed do not have a high impact on the data nosiness. Once a DOF suitable to perform Stereo DIC is achieved, aperture and shutter speed can be regulated to achieve the ideal grey scale distribution. Moreover the slow deformation speed do not causes blurriness in the images.

Conclusions

This series of experiments tested the imaging acquisition system to perform DIC on the front and the back of the specimen. The positioning of the illumination device that allows to minimise the image bias and the data noisiness have been identified. This light positioning will be also used to perform the high speed tests, as explained in Section 3.4.4.

2.4 Grid Method

2.4.1 Theoretical background

.

Another full-field, non interferometric, optical technique able to provide displacement and strain fields is the Grid Method GM. Avril *et al.* in [13] provided a description of the method besides some examples of its application on composite materials. Badulescu *et al.* studied the application of the GM to calculate the one and two dimensional strain fields in a translation and in a tensile test, [32] and [33]. In general, the experimental procedure to perform the GM is similar to the one used for DIC. The only difference lies in the way the images are compared and therefore on how the specimen surface is prepared. If the strain is only to be measured in one direction then a series of black and white parallel lines are used, whereas if the strain

is measured in two perpendicular directions then a grid is deposited on the specimen surface. The grid deposition process is described by Piro and Grédiac in [34] and reported below. In the GM, the displacement and strain information are carried by the light intensity reflected by the grid applied to the specimen and recorded by the CCD sensor. The light intensity can be written as:

$$I(x,y) = \frac{A}{2}[2 + \Gamma F(2\pi f x + \Phi_x) + \Gamma F(2\pi f y + \Phi_y)] \tag{2.3}$$

where A is the amplitude, Γ is the contrast, F is a 2π periodic function, f is the frequency of the carrier defined by the inverse of its pitch p, and Φ_x and Φ_y are the carrier phase modulation along the x and the y axis.
The displacements, u and v, can be defined from the phase variation as:

$$\begin{aligned} u &= -\frac{p}{2\pi}\Delta\Phi_x \\ v &= -\frac{p}{2\pi}\Delta\Phi_y \end{aligned} \tag{2.4}$$

where $\Delta\Phi_x$ and $\Delta\Phi_y$ are the phase variation between final and initial images along x and y direction.
The strain can be evaluated as:

$$\begin{aligned} \epsilon_{xx} &= -\frac{p}{2\pi}\frac{\partial\Delta\Phi_x}{\partial x} \\ \epsilon_{yy} &= -\frac{p}{2\pi}\frac{\partial\Delta\Phi_y}{\partial y} \\ \epsilon_{xy} &= -\frac{p}{4\pi}(\frac{\partial\Delta\Phi_x}{\partial y} + \frac{\partial\Delta\Phi_y}{\partial x}) \end{aligned} \tag{2.5}$$

To achieve high quality measurement it is important that the grid is accurately aligned with specimen and without any bonding defects. Furthermore, to acquire images suitable to perform the GM, it is necessary that the CCD array and the grid are perfectly aligned and that each grid period is sampled by an integer number of pixels. If correctly performed the GM allows the measurement of displacement of the order of 0.5 µm [35].

2.4.2 Specimen surface preparation for GM

To correctly perform the GM the specimen surface has to be prepared with a regular grid as explained in Section 2.4.1. The grid is transferred to the specimen surface from an acetate backing paper which is printed using an industrial plotter with 6000 dpi resolution. To transfer the grid on to the specimen surface the procedure devised by Piro [34] was followed:

1. The surface of the specimen is gently abraded to promote the bonding;
2. The specimen surface and the grid are cleaned using ethanol or isopropanol;
3. A thin layer of white epoxy adhesive, such as E504 form Epotecny, is spread over the specimen surface;
4. The grid, printed on the backing film is then bonded to the specimen;
5. The epoxy resin is cured for at least 35 hours at a temperature of 40° ;
6. The backing film is peeled of the specimen surface leaving the grid bonded to epoxy resin and therefore the specimen surface.

To obtain a complete and high quality grid transfer it is advisable to remove any air bubbles trapped inside the epoxy resin and to ensure a perfect adhesion of the backing film to the resin. This was achieved in this research using a degassing chamber. Figure 2.24 shows a grid deposed over a GFRP specimen, it is possible to observe some imperfections caused by an incomplete grid transfer.

Figure 2.24: Image of the grid deposed over a GFRP specimen: imperfections in the grid transfer are shown.

2.4.3 Grid pitch selection

The grid pitch selection it is dependent on camera resolution and specimen size. Knowing the camera resolution and considering that a suitable number of pixels to sample a grid period is between 5 and 7, it is possible to calculate the number of periods that the sensor is able to sample,

$$Sampled\ Periods = \frac{Camera\ Resolution}{Pixel\ per\ Period} \tag{2.6}$$

the grid pitch can then be determined as

$$Grid\ pitch = \frac{Specimen\ Size}{Sampled\ Periods} \tag{2.7}$$

It is possible to increase the measurement resolution by increasing the number of pixel per period, this also reduces the spatial resolution and the field of view.

2.4.4 Imaging set-up for GM

With the procedure described in Section 2.4.2 a shiny surface is obtained: it is particularly important to take into account the considerations done in Section 2.3.4 to avoid specular reflections that would affect the results. Furthermore to correctly perform the GM two fundamentals conditions have to be respected:

- **Sensor array and grid alignment** The sensor array on the camera must be perfectly aligned with the grid on the specimen. To achieve this it is convenient to use a tripod with a precisely adjustable head and even better if controlled with micrometers. This allows camera rotation and by observing the captured images it is possible to verify when the sensor array is aligned with the grid, as shown in Figure 2.25 a).

- **Grid sampling** Each grid period has to be sampled by an integer number of pixels. To achieve this it is possible to use a linear stage, if a prime lens is used, or a zoom lens. To verify if the correct grid sampling is achieved the images can be processed with MATLAB. The image has to be acquired as an array, and then re-visualised considering a single pixel for every period. If the image appears uniformly coloured each grid period is sampled by an exact and integer number of pixels, as shown in Figure 2.25 b).

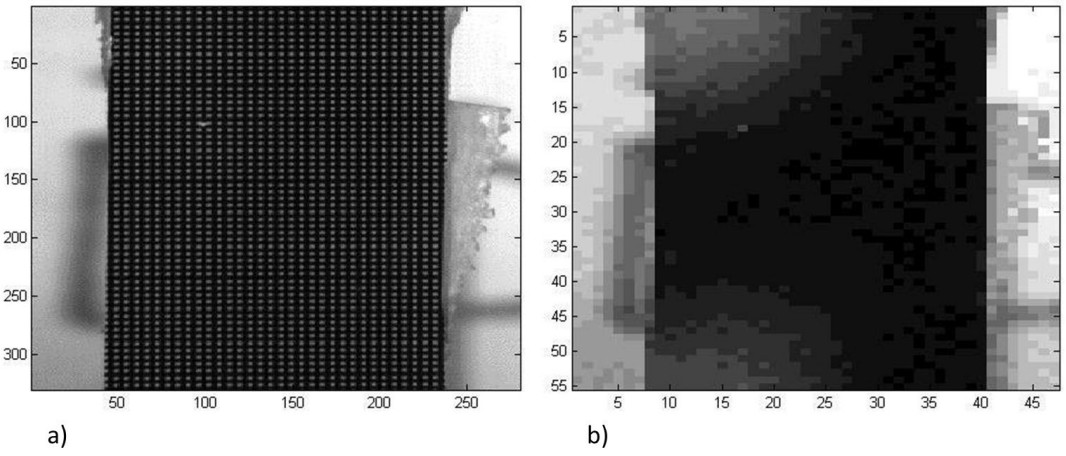

Figure 2.25: GM set-up:
a) Acquired image, the grid is aligned with the sensor array
b) Under-sampled image, the uniform colour indicates a correct grid sampling

2.4.5 Grid Method code development

No commercial software is available to perform the GM, therefore a MATLAB code was developed for this purpose starting from the code provided by Professor Pierron for the Experimental Mechanics course at the University of Southampton [36]. As described in Section 2.4.1 the GM relies on the analysis of the changes of phase in light intensity between consecutive images to extrapolate the strain. The code that was developed works in the following way:

1. The phase of the light is calculated using a discrete Fourier transformation algorithm, developed by Professor Pierron. To avoid phase wrapping the phase change is calculated between consecutive images and not relative to a reference image. This process is known as temporal phase unwrapping.

2. The data are then processed performing a spatial phase unwrapping. It is possible to choose along which axes to perform the unwrapping first.

3. The data close to the grid edges cannot be used so they are discarded.

4. The displacement is calculated using the sensitivity, as in Equation 2.4, and the strain are extrapolated, as described by Equation 2.5.

5. Since it is almost impossible to transfer the grid onto the specimen without any imperfection the GM data present a high level of noise. To reduce the noisiness, Thompson's τ method is applied to detect and eliminate the outliers. This can be done only if the strain field is expected to be uniform.

6. The code developed for this research also features a virtual strain gauge that calculates the strain average over a selected area and with functions to print the strain maps.

The developed code was tested performing a quasi-static tensile tests on a steel dog-bone specimens and using strain gauges for control purposes. The GM has been used to evaluate the strain along the longitudinal ϵ_{xx}, Figure 2.26, and the transverse direction ϵ_{yy}, Figure 2.27. The time-strain graph were produced using the virtual strain gauge feature of the code.

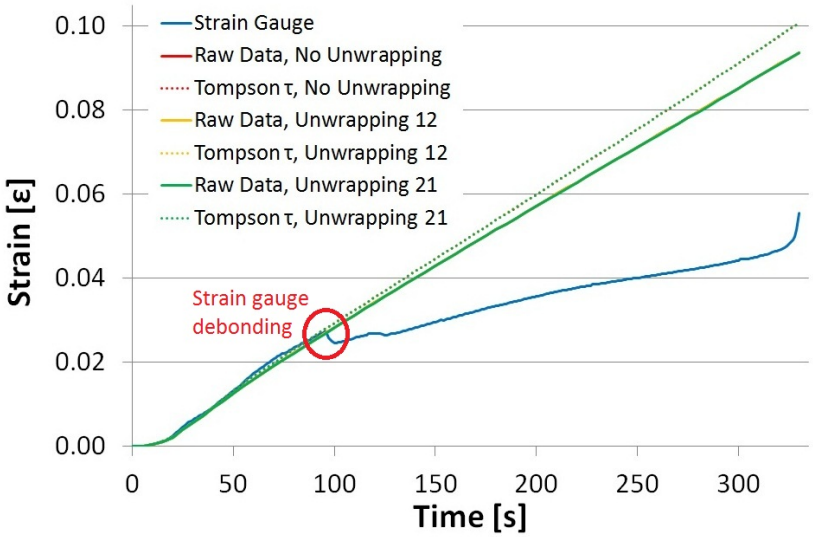

Figure 2.26: Virtual Strain Gauge: Longitudinal Strain vs. Time

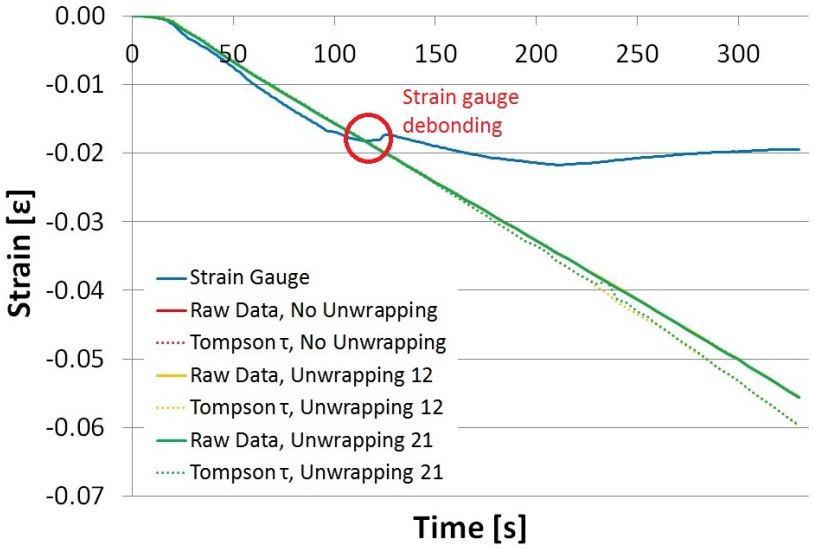

Figure 2.27: Virtual Strain Gauge: Transverse Strain vs. Time

Observing Figures 2.26 and 2.27 it appears evident that the strain data obtained with the GM are in good accordance with the ones recorded with the strain gauge. Furthermore the GM was able to record the strains well after the strain gauge debonding, at about 90 s, and in the plastic deformation region. Furthermore changing the axis along which the spatial unwrapping is performed first does not affect the results, the lines are superimposed. The difference between the raw data and the data after the outlier elimination arises only after the necking of the specimen, when the strain field is not uniform any more.

The obtained strains were used to draw the Stress-Strain curves shown in Figure 2.28.

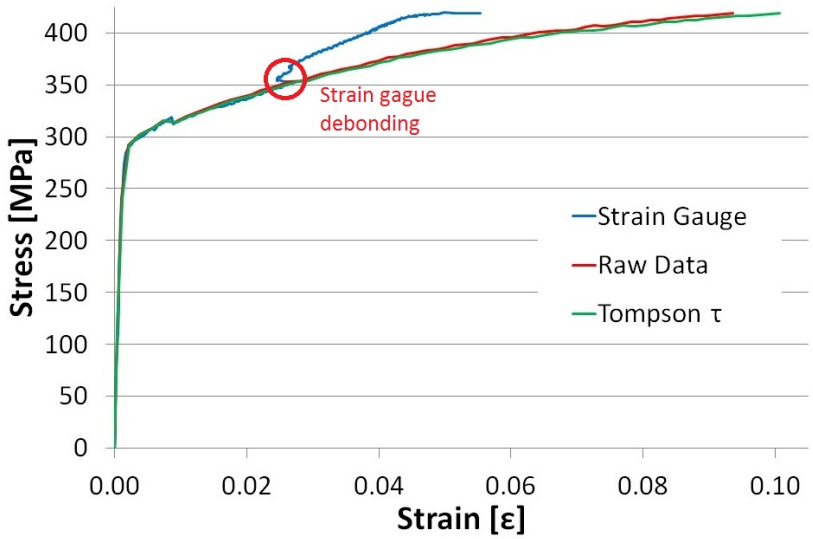

Figure 2.28: Stress-strain curve of aluminium specimen from GM and strain gauge

2.5 Imaging conditions that affect the measurement results

DIC and GM are affected by common issues that might lead to incorrect strain reading. The common link of these techniques is that both rely on sensors to capture digital images of the event, which are then post processed to evaluate the strain. Various causes might lead to the acquisition of distorted images, potentially producing incorrect measurement of strain values:

- **Background noise** Heat waves from the illuminating system, vibrations from the machine or the environment, voltage fluctuation in the imaging sensor and other random phenomena cause each pixel detector to have biased image acquisition. It is possible to identify the sources of the background noise and to mitigate its effect. It is also possible to quantify the the measurement resolution. To do so, a series of images of the unloaded specimens must be processed to obtain the displacement and strain maps from which fundamental information can be obtained:
    - The presence of localised areas of inhomogeneous strain or displacement is symptomatic of an incorrect imaging set-up, the noisiness should be uniformly distributed.
    - Average value of the maps: when the imaging set-up is correct these values are zero.
    - The standard deviation of the displacement and strain values give a first evaluation of the displacement and strain resolutions of the measurement

system.

- **Out of plane movement** 2D DIC and GM are not able to detect the movement of the specimen in the third direction and account for it during the processing. During the test, the specimen may be subjected to movements and rotations that vary the distance between the imaging sensor and the specimen, resulting in a change of magnification interpreted as a strain when analysing the images. Out of plane movement of the specimen results from compliances in the specimen clamping, realignment of the specimen with the load, torsion of the specimen during the test and testing equipment vibrations. In the experiment design stage it is important to reduce the out of plane movement as much as possible. The relationship between out of plane movement and the parasitic strain induced in a DIC by the out of plane movement is [15]:

$$Parasitic\ \epsilon_{xx} = \frac{dz}{z} \tag{2.8}$$

$$Parasitic\ \epsilon_{yy} = \frac{dz}{z} \tag{2.9}$$

$$Parasitic\ \epsilon_{xy} = 0 \tag{2.10}$$

  where z is the distance between the specimen and the lens and dz is the out of plane movement. For example, considering an imaging distance of 500 mm and an out of plane movement of 0.75 mm a parasitic strain of the 0.15% is to be expected. The same formula was used by Pannier *et al.* [19] to evaluate the effects of out of plane movement on GM measurement. To minimise the effects of the out of plane movement the suggested solutions are:

  - Minimise the out of plane movement of the specimen, dz, by acting on the specimen clamping;
  - Increase the stand-off distance, z;
  - Use of a telecentric lens, solution made inconvenient by other issues such as lighting, cost and lack of flexibility [19].

- **Camera misalignment** When performing 2D DIC and GM it is important that the imaging sensor is parallel to the target. If this condition is not respected a distortion in the images is introduced and errors in the displacement and strain values have to be expected, [37] and [38]. When setting-up the experiment a spirit level can be used to verify the pitch and roll angles (using aeronautical jargon) of the camera, while the reflection of a laser pointer on a mirror, provisionally mounted on the target surface, can be used to verify the pitch and yaw angles [15]. Furthermore, for DIC, the misalignment can be detected

processing the images of a rigid body motion [38] and compensated performing a calibration [39].

- **Lens distortion** Lenses introduce a distortion in the captured images, this ultimately affects the evaluated displacement and strain fields [40] and [41]. For Stereo DIC this is automatically compensated by the calibration process, that Lava *et al.* in [41] recommend also for 2D DIC.

Before each test steady images of the specimens should be taken to evaluate the imaging set-up quality. A first evaluation of the measurement resolution can be identified as the higher value between the system resolution and the parasitic strain caused by the out of plane movement. In this research maximum care was taken in the camera-specimen alignment, using the approach described above. The lens distortion was not taken in consideration: the lens distortion resulted in errors lower than the strain and displacement resolution hence there was no impact on the measurement.

2.6 Conclusions

In this chapter important preliminary information that will guide the experimental set-up at high speed have been collected. The noise sources for full-field optical technique have been identified. This will allow the selection of the best clamping device to be used when testing on Instron VHS in Section 3.3.2. The information about the best positioning of the illumination devices identified in Section 2.3.4 have been applied to the GM and will be used in Section 3.4.4.

3 Background to high speed testing approaches and development of methodology

3.1 Introduction

A complete, but somewhat dated, review of the techniques used to test composite materials at high strain rate was published by Hamouda and Hashmi [42]. It must be noted that most of the testing methodologies have not significantly changed in the last decades. The different techniques suitable for assessing the mechanical behaviour of composite materials at different strain rates are summarised in Table 3.1.

Table 3.1: Experimental techniques for high strain rate tensile testing as in [42] integrated with [43]

Technique	Strain rate [s^{-1}]
Conventional Machine	Quasi-Static (QS)-≤ 0.1
Drop weight machine (DW)	≤ 10
Servo hydraulic machine (SH)-VHS	$0.1 \rightarrow 100$
Charpy pendulum	≤ 100
SHB	$100 \rightarrow 10^4$
Expanding ring	10^4
Flyer plate and ballistic impact	$\geq 10^5$

From a survey of the literature it emerges that the most widely used technique to investigate the high rate behaviour of composite materials is the SHB. On one hand this technique generates considerably high strain rates, on the other hand it presents some issues in the specimens connection to the machine and limits the dimensions of the specimen, e.g. 12 mm in [44] with a threaded connection and 11 mm in [45] with a dovetail connection.

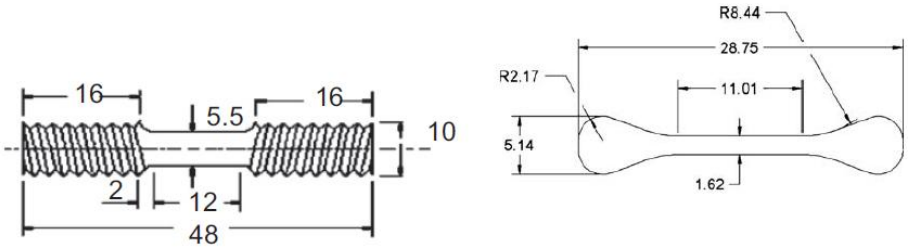

Figure 3.1: SHB specimens in [44] and [45]

Bardenheider and Rogers [11] stated that servo hydraulic machines give access to intermediate strain rates, difficult to access with the other testing techniques. Nowadays servo-hydraulic high rate machines allow a cross-head displacement speed that ranges from quasi-static to 25 m/s, that means a characteristic test duration that ranges from 10 to 10^{-5} s and a strain rate between 10^{-3} and 10^{3} s^{-1}, as shown in Figure 3.2.

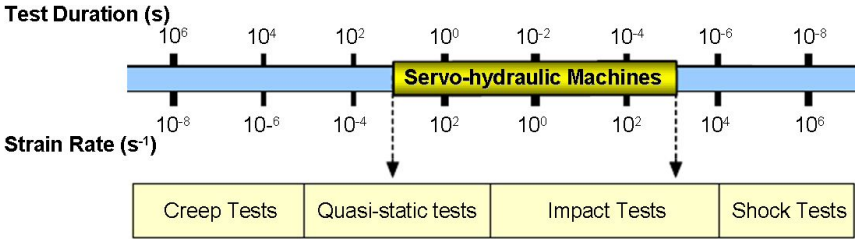

Figure 3.2: Test duration and strain rates achievable with different test devices, from [11]

Despite the advantages offered by a servo-hydraulic machine for high rate testing, not many research groups are known to use this kind of machine for testing composite materials. Table 3.2 summarises the available literature reporting high rate experiments on composite materials using servo-hydraulic testing machines.

Table 3.2: Available literature on high rate tests with servo-hydraulic machines

Year	Material	Cross-head speed [m/s]	Reference
2004	GFRP	$1 \rightarrow 20$	[46]
	CFRP		
2005	Glass-$CaCO_3$-Polyester	Not Known	[47]
	CFRP		
2009	GFRP	QS $\rightarrow$ 2	[48]
2009	GFRP	QS $\rightarrow$ 2	[49]
2009	GFRP	QS $\rightarrow$ 2	[50]
2011	GFRP	QS $\rightarrow$ 2	[51]
2013	CFRP	QS $\rightarrow$ 2	[52]

The behaviour of composite materials within the strain rate range achievable with servo-hydraulic machines has not been deeply investigated regardless of the fact that it could be an interesting point of view for understanding and interpreting composite

materials strain rate dependence. Furthermore servo-hydraulic machines allow the use specimens with dimensions comparable with those used for quasi-static tests, offering a suitable surface for full-field strain measurement techniques. Moreover the development of high speed cameras has made it possible to capture images with high temporal resolution during an intermediate strain rate test duration. These cameras make the application of optical strain measurement techniques suitable for the characterisation of composite materials in the strain rate range achievable with high-speed servo-hydraulic machines. This identifies an interesting research gap that can be filled with the equipment available to the author of this thesis.

This chapter is opened by a review of the published investigations on the strain rate dependent behaviour of carbon and glass FRP unidirectional laminates, Section 3.2. In the rest of the chapter a testing set-up to perform high speed tensile tests with the aid of full-field optical strain measurement techniques is devised. In Section 3.3 the usage of Instron VHS to perform high speed tests with FRP materials is discussed. While the issues related to the application of the full-field strain measurement techniques to high speed testing,particularly the data synchronisation and the specimen illumination, are discussed in Section 3.4.

3.2 Strain rate dependent composite material behaviour

A review article on the effect of strain rate on the mechanical properties of FRP was presented by Jacob *et al.* [53], this constitutes the starting point of the present section. The review presented here is focused on the experimental works on unidirectional glass and carbon reinforced epoxy laminates.
Harding and Welsh in [54] used a modified version of the SHB to conduct a study to determine the mechanical properties of CFRP and GFRP materials under tensile impact loading. The relevance of this article to the present work is limited to the CFRP materials that were tested in a unidirectional layup. Experiments were run from strain rates of 10^{-4} up to 10 s^{-1} using a standard tensile testing machine while the SHB allowed to reach strain rates of 10^{3} s^{-1}. The authors observed that a strain rate variation of over seven orders of magnitude did not affect the tensile modulus. This represents the first effort to characterise the strain rate dependence of FRP.
Hsiao and Daniel conducted extensive work to investigate the effects of strain rate on the compressive and shear behaviour of CFRP materials. Strain rates below 10 s^{-1} were generated using a standard servo-hydraulic machine and strain rates up to several hundred s^{-1} were generated through a drop tower apparatus. The beha-

viour of the CFRP loaded in compression along the fibre direction was investigated from the quasi-static up to 110 s^{-1}, and a slight increase of the values of the modulus was observed. The transverse and shear behaviour, that according to the authors are governed by the matrix, were investigated respectively up to 160 and 300 s^{-1}. From the obtained stress strain curves it was possible to conclude that the transverse modulus increased in the investigated strain rate range by 37%. The authors did not provide a quantitative value of the stiffening of the shear modulus. The same conclusions about the matrix-dominated behaviour of CFRP were drawn in a consecutive paper by Hsiao *et al.* [55]. Three different machines were used to apply compressive load at different strain rates: a standard servo-hydraulic for strain rate below 10 s^{-1}, the drop tower apparatus for the range between 10 and 300 s^{-1}, a SHB to generate strain rates between 500 and 1800 s^{-1}. The stress-strain curve for the tests conducted on specimens with a 90° fibre orientation showed a stiffening of 37% with the increase of the strain rate from 0.0001 to 1800 s^{-1}. The authors proposed two explanations for this phenomenon: the visco-elastic behaviour of the polymeric matrix and the time-dependent nature of the accumulating damage. Shear behaviour compressive tests were run on specimen with 15, 30, 45 and 60° fibre orientation. The authors observed an increase of the stress level of the plateau region before the material failure, also the initial shear modulus was observed to increase by about 18% over the investigated strain rate range.

Lowe [56] conducted a study on the strain rate and temperature effect on unidirectional CFRP laminates using a standard servo-hydraulic machine. The explored strain rate range was limited as the cross-head displacement speed ranged between 10^{-2} and 10^{2} $mm \cdot min^{-1}$, but the temperature range between -50 and 150°C makes this study an interesting and valuable confirmation of the fact that the transverse and shear behaviour of composite materials are dominated by the matrix behaviour. Melin and Asp in [57] found the transverse mechanical properties of CFRP to have a weak or negligible dependence on the strain rate. The authors loaded dog-bone specimens in a SHB at strain rates between 100 and 800 s^{-1} and quasi-statically in a hand-driven loading frame. The true strain field was measured by the Moiré technique. It was observed that the average transverse modulus is independent from the strain rate whereas the the initial transverse modulus decrease slightly with the increase of the strain rate. The authors concluded that when loaded in the transverse direction, in a strain rate range between 10^{-3} and 10^{3} s^{-1}, CFRP materials show a weak dependence on the strain rate.

A study about the strain rate dependence of the longitudinal and transverse behaviour of CFRP was carried out by Hosur *et al.* in [58]. Unidirectional laminates were tested in the direction parallel and perpendicular to the reinforcement fibres at strain rates of 82, 164 and 817 s^{-1}. An increase of the transverse and longitudinal

moduli of 50% and 86% respectively from the static values to the maximum investigated strain rate was observed.

Gilat *et al.* in [6] studied the strain rate tension behaviour of CFRP unidirectional specimens with fibres oriented at 90° 10° 45° and a ±45° cross-ply. A servo-hydraulic machine was used to achieve strain rates between 10^{-5} and 1 s^{-1}, while strain rates between 400 and 600 s^{-1} were achieved using a tensile SHB. A non quantified increase of the material stiffness was observed with the increase of the strain rate. The authors suggested that the sensitivity to strain rate in composite materials is driven by the resin behaviour.

In their work Taniguchi *et al.* [59] found that the longitudinal modulus in a strain rate range from the quasi-static up to 100 s^{-1} remains constant. In contrast the matrix dominated shear and the transverse moduli showed an increase of 13% and 77% respectively within the investigated strain rate range. Taniguchi *et al.* draw the same conclusions in [60], where the behaviour of CFRP unidirectional materials with fibre orientations at 10, 30, 45, 60 and 90° was studied. A tensile SHB was used to reach strain rates up to 150 s^{-1}. The unidirectional off-axis specimens were prepared using oblique end-tabs to minimise the extension-shear coupling effect. The moduli were observed to increase by about 20% in the investigated stain rate range. The authors attributed this behaviour to the visco-elastic behaviour of the resin.

Koerber *et al.* in [61] investigated the compression and shear-compression behaviour of unidirectional specimens with 15, 30, 45, 60, 75, and 90° fibre orientation angles. Strain rate up to 350 s^{-1} were achieved using a SHB ans the strain was measured using DIC. An increase of 12% in the transverse compression modulus of elasticity and of 25% in the in-plane shear modulus of elasticity were observed over the investigated strain range. For combined transverse compression and in-plane shear loading the off-axis modulus of elasticity increased by 20%.

The variation of longitudinal tensile modulus over a strain rate range from 10^{-4} up to 87.4 s^{-1} of CFRP was studied by Al-Zubaidy *et al.* in [62] using standard and high-speed servo-hydraulic test machines. The modulus was observed to increase by about 20% almost linearly over the strain rate range. The authors attribute this to a combination of the visco-elastic behaviour of the polymeric matrix.

Berthe *et al.* [52] conducted a study aimed at the identification of a sample geometry that allows consistent mechanical tests results at various strain rates to be obtained to inform a visco-elastic mesoscopic model to describe CFRP strain rate dependence from creep to dynamic loadings. Transverse modulus was observed to be insensitive to a strain rate variation between 0.0009 and 21 s^{-1}; while the shear modulus increased by 30% between 0.001 and 88 s^{-1}.

A complete investigation work on the behaviour of CFRP materials subjected to different strain rate deformation was undertaken by Shokrieh and Omidi in a series

of four articles, [48], [49] [50] and [51]. The authors, using a servo-hydraulic test machine equipped with a strain rate increase mechanism, achieved strain rates between 0.001 and 100 s^{-1}. The longitudinal modulus was studied both in tension and in compression: the tensile Young's modulus was found to increase by about 12% [48], while the compressive Young's modulus was found to increase by about 53% [49], over a strain rate range of five orders of magnitude. Furthermore the authors proposed a regression function to describe the effect of the strain rates on the material properties in the form of:

$$M\left(\dot{\epsilon}\right) = \alpha + \beta\dot{\epsilon}^{\chi} \tag{3.1}$$

where M is a generic material property, $\dot{\epsilon}$ is the strain rate and α, β and χ are material constants obtained by fitting the curve to the obtained experimental results. It has to be remarked that the quasi-static compressive and tensile longitudinal moduli differ by about 50%. Even though the authors used the same clamping fixtures and designed the specimens to allow a smooth load transfer from the grip to the specimens, the difference between the longitudinal moduli calculated in tension and in compression may be attributable to the test boundary conditions. Furthermore, also the shapes of the regression functions that describe the strain rate dependent behaviour of the moduli are different, as shown in Figure 3.3 and by the obtained material constants presented in Table 3.3.

Table 3.3: Material constants for curve fitting describing the strain rate dependence of the longitudinal modulus, from [48] and [49]

Constant		Tensile	Compressive
α	[GPa]	37.243	7.223
β	[GPa·s]	1.139	24.449
χ		0.276	0.0529

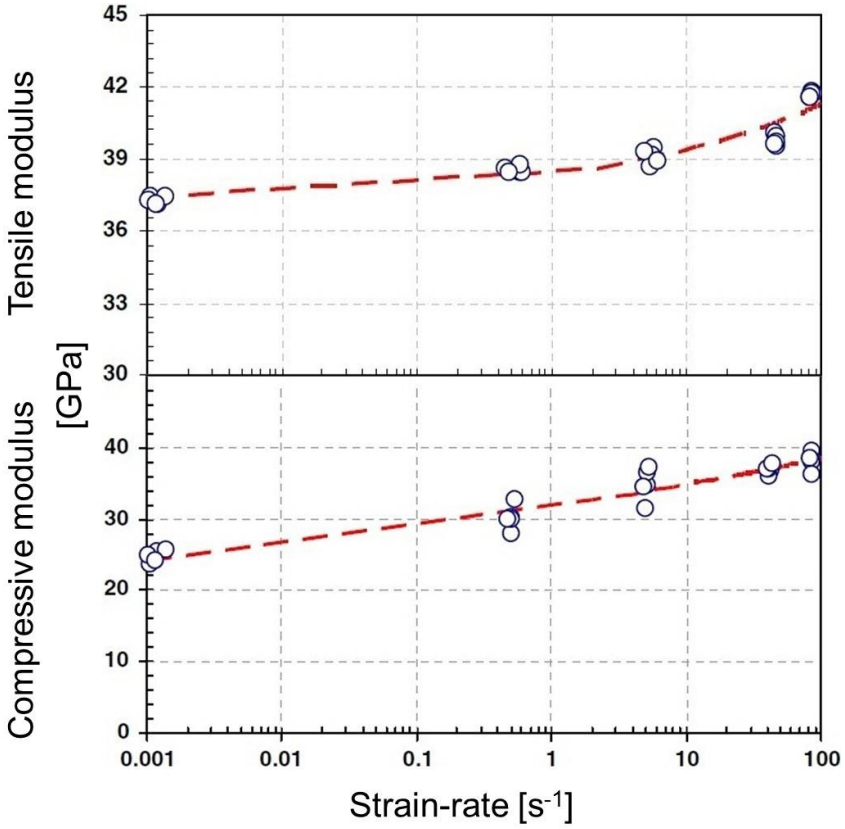

Figure 3.3: Effect of the strain rate on the longitudinal moduli from [48] and [49]

Another example of the different behaviour of the material under compressive and tensile load can be found in the work of Shokrieh and Omidi about the transverse behaviour of the same CFRP material, [51]. The compressive and tensile transverse moduli differ by about 11%. The same testing apparatus of the articles presented previously was used and the same strain rate range was explored. This led to an increase of the tensile transverse modulus of about 14% and of the compressive transverse modulus of about 23%. Also the material constants obtained from the regression function, Equation 3.1, are different for the tensile and the compressive load, as shown in Figure 3.4 and in Table 3.4.

Table 3.4: Material constants for curve fitting describing the strain rate dependence of the transverse modulus, from [51]

Constant		Tensile	Compressive
α	[GPa]	10.037	11.419
β	[GPa·s]	0.4370	0.0259
χ		0.2624	1.0216

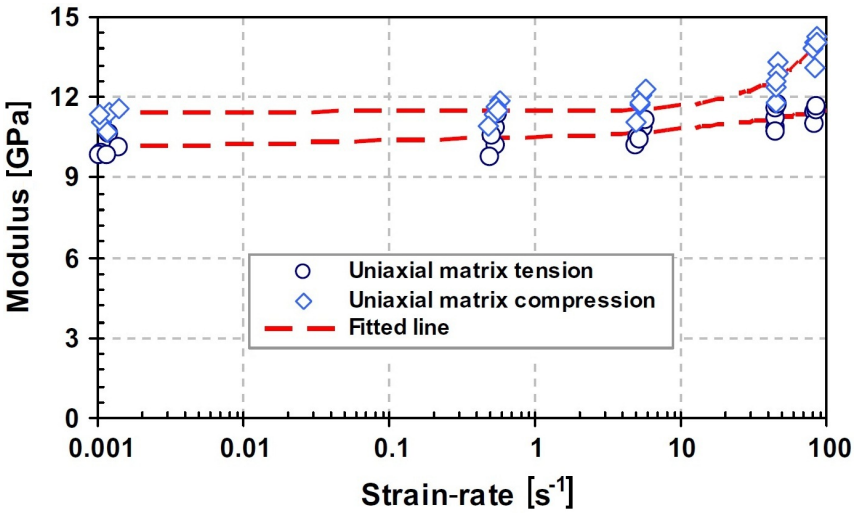

Figure 3.4: Effect of the strain rate on the transverse moduli from [51]

The number of the significant figures of the values presented in Tables 3.3 and 3.4 might appear to be excessive, it has to be remarked that these values are quoted from [48], [49] and [51]. Finally Shokrieh and Omidi in [50] studied the strain rate dependence of the shear behaviour of a $\pm 45°$ angle-ply laminate. In this case a 15% decrease of the elastic shear modulus was observed over the investigated strain rate range. This result are in contradiction with the literature presented so far. Berthe *et al.* in [52] found a monotonic increase of the shear modulus with the strain rate with a similar lay-up. While Gilat *et al.* in [6] recorded a similar shear modulus in the low and moderate strain rate range, between 9.10^{-5} to 2 s^{-1}, and a higher one at 600 s^{-1}. Shokrieh and Omidi do not provide an explanation to this inconsistency with the existing literature.

Data regarding the Poisson's ratio is not widely reported in the literature. A study was conducted by Okoli and Smith in [63] on GFRP cross-ply laminate. The material was loaded in a strain rate range between quasi-static and 3 s^{-1}. The authors concluded that the Poisson's ratio is strain rate insensitive. It has to be remarked that these results are not of direct interest for the present work, as the material has a different structure from the one considered here with fibres both parallel and perpendicular to the load direction, but represent the only reliable information about the strain rate dependence of Poisson's ratio. Also Taniguchi *et al.* [60] considered the Poisson's ratio in their study about the dynamic tensile properties of CFRP loaded in matrix-dominant directions. The authors, testing pure resin coupons equipped with strain gauges, concluded that the Poisson's ratio decreased with the strain rate. Also this results is of limited interest for the present study: here the effect of the fibre on the general composite behaviour is not taken into account and again it is not possible to relate these result to the behaviour of plastics reinforced with unidirectional fibres.

The publications discussed above are summarised in Tables 3.5, 3.6 and 3.7. In the tables below the acronyms are the same as those used in Table 3.1, 'Tens' and 'Comp' identify a tensile or a compressive load.

Before concluding this review it is important to mention also the work conducted to characterise the strain rate dependent behaviour of pure resin epoxy specimens. Tay *et al.*, [66] conducted a study on pure epoxy specimens (Ciba-Geigy LY5052 cured with alkylamine HY5052 hardener) subjected to compressive loading over a strain rate range from 5 to 2500 s^{-1} using a servo-hydraulic machine and a SHB observing a two to three-fold increase in the initial elastic modulus. Buckley *et al.* [67] conducted a comparative study on the compressive behaviour of three different thermosetting resins (Hexcel Composites CT200, 3M-PR500 and Cytec 5250-4) in a strain rate range from 10^{-3} to 5^{3} s^{-1} using a SHB. The authors observed an increase of the elastic modulus of the order of 70% for the CT200 and 3M-PR500 resins, that are based on a bisphenol compound. The elastic modulus of Cytec 5250-4, a bismaleimide resin, showed an increase of four times over the investigated strain rates. Gilat *et al.* [68] [69] used a servo-hydarulic and a SHB to investigate the shear and tensile response of E-862 and PR-520 resins over a strain rate range from 5^{-5} to 700 s^{-1}. The authors observed for both the resins a stiffer material response, i.e. a moduli increase, with increasing strain rate in both tension and shear loadings. Naik *et al.* [70] studied the shear properties of epoxy LY-556 in a strain rate range from 385 to 880 s^{-1} using a torsional SHB observing a 22% increase in the shear modulus from the quasi-static value. Al-Zubaidy *et al.* [71] investigated the mechanical properties of Araldite 420 epoxy under quasi-static and medium impact tensile loads using a drop weight machine. The authors observed an increase of 85%, 98% and 106% form the quasi-static value of the modulus for strain rates of 54.2, 67.2 and 87.5 s^{-1} respectively. From the presented papers it can be concluded that, for epoxy resin, an increase in the strain rate leads to an increase of the material stiffness. The review indicates that the magnitude of the strain rate induced stiffening is dependent on the resin chemical composition.

The publications discussed above are summarised in Table 3.8. In the tables below the acronyms are the same as those used in Table 3.1.

Table 3.5: Summary of publications on the effects of strain rate on longitudinal modulus of composite materials

Year	Reference Author		Material Type	Test Strain rate [s^{-1}]	Test Machine	Test Direction	Strain rate effect on E_{11}
1983	Harding and Welsh	[54]	CFRP	QS - 10^3	SH,SHB	Tens	Not influenced
1998	Hsiao and Daniels	[64]	CFRP	QS - 110	SH,DW	Comp	Slight increase
2001	Hosur *et al.*	[58]	CFRP	QS - 10^3	SHB	Comp	Increase
2001	Hall and Guden	[65]	CFRP	QS - 10^3	SHB	Comp	Slight decrease
2007	Taniguchi *et al.*	[59]	CFRP	QS - 10^2	SHB	Tens	Not influenced
2009	Shokrieh and Omidi	[48]	GFRP	QS - 10^2	SH	Tens	Slight increase
2009	Shokrieh and Omidi	[49]	GFRP	QS - 10^2	SH	Comp	Slight increase
2012	Al-Zubaidy	[62]	CFRP	QS - 10^2	SH	Tens	Increase

Table 3.6: Summary of publications on the effects of strain rate on transverse modulus of composite materials

Year	Reference Author		Material Type	Test Strain rate [s^{-1}]	Test Machine	Direction	Strain rate effect on E_{22}
1996	Lowe	[56]	CFRP	QS	SH	Comp	Increase
1998	Hsiao and Daniels	[64]	CFRP	QS - 10^3	SH,DW	Comp	Increase
1999	Melin and Asp	[57]	CFRP	QS - 10^3	SH,SHB	Tens	Not influenced
1999	Hsiao *et al.*	[55]	CFRP	QS - 10^3	SH,DW,SHB	Comp	Increase
2001	Hosur *et al.*	[58]	CFRP	QS - 10^3	SHB	Comp	Increase
2001	Hall and Guden	[65]	CFRP	QS - 10^3	SHB	Comp	Not influenced
2002	Gilat *et al.*	[6]	CFRP	QS - 600	SH,SHB	Tens	Increase
2007	Taniguchi *et al.*	[59]	CFRP	QS - 10^2	SHB	Tens	Increase
2008	Taniguchi *et al.*	[60]	CFRP	QS - 10^2	SHB	Tens	Increase
2010	Koerber *et al.*	[61]	CFRP	QS - 10^2	SHB	Comp	Increase
2011	Shokrieh and Omidi	[51]	GFRP	QS - 10^2	SHB	Comp-Tens	Increase
2013	Berthe *et al.*	[52]	GFRP	QS - 20	SH	Tens	Not influenced

Table 3.7: Summary of publications on the effects of strain rate on shear modulus of composite materials

Reference			Material		Test			Strain rate
Year	Author		Type	Fibres orientation [°]	Strain rate [s^{-1}]	Machine	Direction	effect on G_{12}
1998	Hsiao and Daniels	[64]	CFRP	30-45	QS - 10^3	SH,DW	Comp	Increase
1999	Hsiao *et al.*	[55]	CFRP	15-30-45-60	QS - 10^3	SH,DW,SHB	Comp	Increase
2002	Gilat *et al.*	[6]	CFRP	±45 10-45	QS - 600	SH,SHB	Tens	Increase
2007	Taniguchi *et al.*	[59]	CFRP	15-30-45-60-75	QS - 10^2	SHB	Tens	Increase
2008	Taniguchi *et al.*	[60]	CFRP	10-30-45-60	QS - 10^2	SHB	Tens	Increase
2009	Shokrieh and Omidi	[50]	GFRP	±45	QS - 10^2	SH	Tens	Decrease
2010	Koerber *et al.*	[61]	CFRP	15-30-45-60-75	QS - 10^2	SHB	Comp	Increase
2013	Berthe *et al.*	[52]	GFRP	±45	QS - 90	SH	Tens	Increase

Table 3.8: Summary of publications on the effects of strain rate on epoxy resin

Year	Reference Author		Material Type	Test Strain rate [s^{-1}]	Test Machine	Studied Modulus	Strain rate Effect
1995	Tay *et al.*	[66]	Ciba-Geigy LY5052	5 - 2500	SH,SHB	E_{11}	Increase
1998	Buckley *et al.*	[67]	Hexcel Composites CT200 3M-PR500 Cytec 5250-4	10^{-3} - 5000	SHB	E_{11}	Increase
2007	Gilat *et al.*	[69]	Shell Chemical E-862 Cytec PR-520	QS - 700	SH,SHB	E_{11}, G_{12}	Increase
2010	Naik *et al.*	[70]	LY-556	385 - 880	SHB	G_{12}	Increase
2010	Al-Zubaidy *et al.*	[71]	Araldite 420	QS - 87.5	DW	E_{11}	Increase

Concluding this review, it is important to summarise some aspects of the work conducted so far in determining the strain rate dependent behaviour of fibre reinforced polymers:

- All the authors agree that the transverse and shear behaviour of FRP is controlled by the behaviour of the matrix.
- Not all the findings are in agreement between each other:
  - Observing Table 3.5 it appears evident how the majority of the author agree that, both for CFRP and GFRP, the longitudinal Young's modulus increase with the strain rate. However Harding and Welsh in [54] and Taniguchi *et al.* [59] found it to be strain rate independent, while Hall and Guden in [65] observed a slight decrease with the increase of the strain rate.
  - Observing Table 3.6 the general trend of the results suggests that the transverse Young's modulus increases with the strain rate. Three papers (Melin and Asp [57], Hall and Guden [65] and Berthe *et al.* [52]) indicate the transverse Young's modulus as strain rate independent.
  - Observing Table 3.7 the only paper in contrast with the general trend, is the one from Shokrieh and Omidi [50] that describes a decrease of the shear modulus with the increase of the strain rate.
- Even though all the authors present non linear shear stress-strain curves, none of them clearly states how the shear modulus was deduced from these curves.
- Observing Table 3.8 all the authors agree in identifying a stiffening of the epoxy resin with the increase of strain rates, this is dependent on the resin chemical composition.

3.3 High speed testing with Instron VHS

The advantages of using a high speed servo-hydraulic machine for testing at intermediate strain rates with full-field strain measurement techniques, have been discussed above. The use of this machine poses the challenges of designing a clamping system and a specimen suitable to correctly withstand the shock load imposed by its working mechanism.

3.3.1 VHS Description

The high speed tests are performed using an Instron VHS 1000, servo-hydraulic test machine. The machine works by accumulating oil at a pressure of 280 bar in an accumulator regulated by proportional valves. These valves are controlled by a system that releases the amount of oil needed to move the actuator at the required speed. The actuator is capable of moving at a maximum displacement speed of 20 m/s. To reach the operating test speed the actuator requires an acceleration travel of 150 mm. The maximum load capacity is 80 kN. A schematic of the Instron VHS is shown in Figure 3.5.

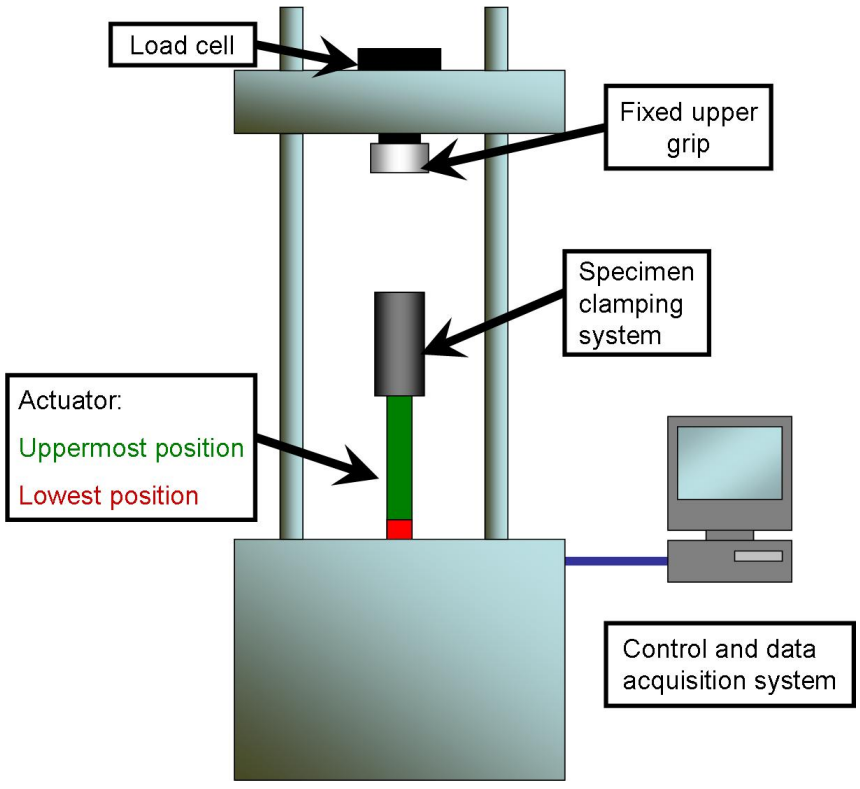

Figure 3.5: Schematic of Instron VHS

The data acquisition system of Instron VHS has the ability to record 4 simultaneous signals at sampling frequencies up to 1 MHz. The load is recorded with

a 100kN Kistler 9071A washer type piezoelectric load cell attached to the cross-head and coupled a Kistler Type 5011B charge amplifier. Two channels of the data acquisition system are always used to record the actuator displacement and the load.

3.3.2 Specimen clamping

The test machine actuator must be accelerated to reach the desired displacement speed. During the actuator acceleration phase the specimen must not be clamped or loaded until the desired test speed is achieved, upon which the specimen must be instantly loaded. To overcome this issue, the Instron VHS was originally fitted with a fast jaw system, whose working principle is shown in Figure 3.6

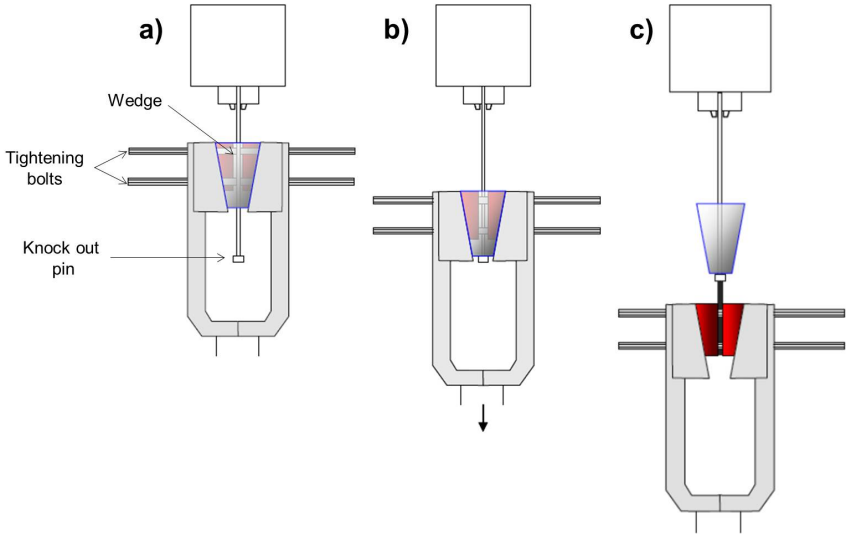

Figure 3.6: Fast jaw system:
a) The actuator accelerates, the specimen is not loaded.
b) The wedges hit the knock out pins, the specimen is clamped
c) The specimens is clamped and loaded

The jaw faces are kept apart by two wedges that are subjected to a closure force generated by tightening four bolts. Initially the actuator accelerates with the jaw faces that slide along the specimen without loading it, Figure 3.6a). At the desired position two knock out pins, that are rigidly connected to the test machine, stop the wedges (Figure 3.6b)) and the jaws are free to clamp the specimen (Figure 3.6c)).

In the work of Wang *et al.* [46] an Instron VHS servo-hydraulic test machine was used to test glass and carbon reinforced epoxy specimens at strain rates between 15 and 43 s^{-1}. The specimen's dimensions are shown in Figure 3.7.

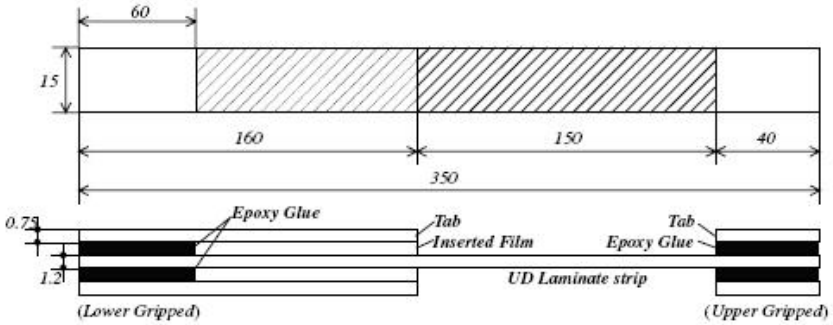

Figure 3.7: Specimen configuration in [46]

The specimen was loaded using the fast jaw system, described above. The extended end-tabs on the left side of the specimen were designed to allow the actuator acceleration travel before the fast jaw system loads the specimen. Such a specimen has a surface of 15 by 150 mm, which is considerably larger than the specimens used in SHB, this simplifies the application of full-field optical measurement techniques.

To use of the fast jaw system an adaptor, based on the working principle of to the extended end-tabs used by Wang *et al.* shown in Figure 3.7, was designed to provide a metallic surface for the jaw faces to clamp on. Two parameters have to be taken into account when setting-up the system before every test:

- Distance of the jaw faces from the adaptor;
- Bolts pre-load.

These parameters cannot be easily and reliably controlled and therefore the repeatability of the tests cannot be ensured. Furthermore if these parameters are not correct the jaw faces slip along the adaptor resulting in an incorrect loading of the specimens that ultimately affects the stress-strain curve defintion and the characterisation of the material. The effects of this slippage on the load history can be seen in Figure 3.8 that shows the time-load plot of tensile test run at 1 m/s on a CFRP specimen.

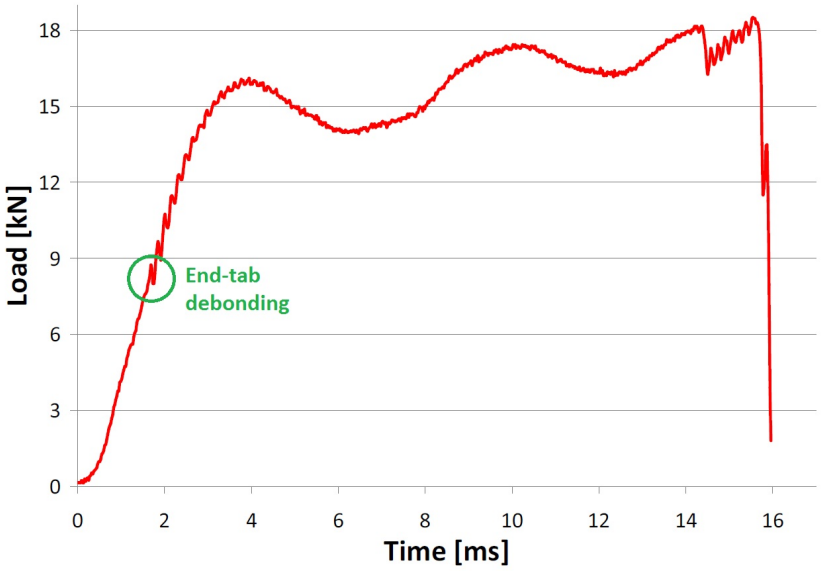

Figure 3.8: Effect of the fast jaw slippage on the load history

At about 8 kN the load trace starts to oscillate as effect of the end-tab debonding, this issue will be discussed below. Furthermore, after 15 kN, a change in the load rate appears, this is due to the fact that the jaw faces are slipping on the specimens, and the actuator is moving without loading the specimen. The following issues that affect the quality of the results are identified:

1. Low repeatability of the experiments;
2. Slippage between the jaw faces and the adaptor;
3. High out of plane movement of the specimen;
4. Long set-up time for each experiment.

In the work of Fitoussi *et al.* [47], a servo-hydraulic machine was used to achieve strain rates between 0.5 and 60 s^{-1}. An experimental methodology that allowed the micro and macroscopic characterisation of composite materials was defined. To allow the actuator to accelerate before loading the specimen a slack adaptor was used. Also, to be able to observe damaged but not failed specimens, a sacrificial fuse-specimen, intended to break at a lower load than the tested specimen, was positioned between the specimen and the actuator.

To overcome some of the issues related to the fast jay system, a slack adaptor system was developed at the University of Southampton, based on the design of Fitoussi *et al.* [47]. Its working principle is shown in Figure 3.9.

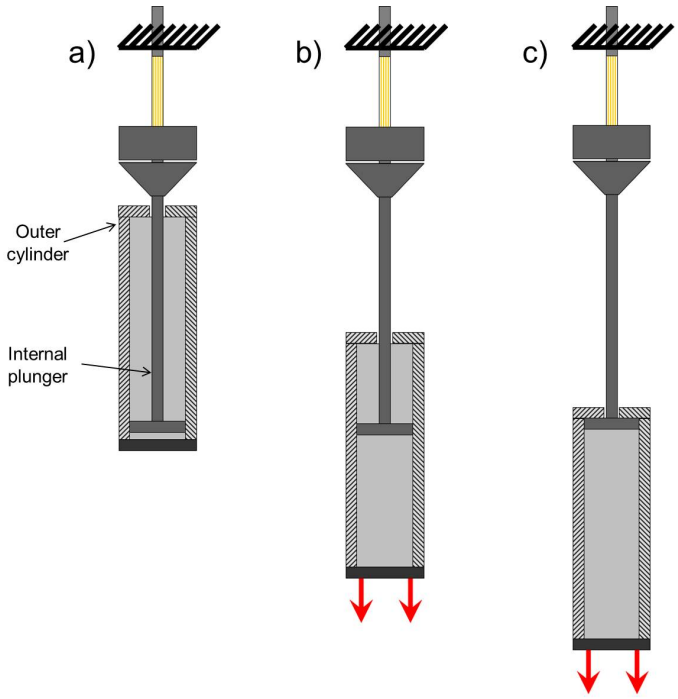

Figure 3.9: Slack adaptor system:
a) The actuator is in the uppermost position, the specimen is not loaded.
b) The actuator accelerates, the cylinder and the plunger are not engaged, the specimen is not loaded.
c) The actuator reaches the desired speed, the cylinder engages with the plunger, the specimen is loaded.

The specimen is clamped, using a jaw system, to a plunger fitted inside a cylinder connected to the tensile test machine actuator (Figure 3.9a)). When the actuator moves the cylinder is driven along with it but freely moves around the plunger, i.e. the specimen is unloaded (Figure 3.9b)). When the cylinder reaches the end of the plunger the two elements engage and the specimen is loaded (Figure 3.9c)).

The slack adaptor system is an efficient solution both to reduce the set-up time of each test and increase the repeatability of the experiments. Importantly it circumvents the slippage issue that exists with the fast jaw system, thereby providing a repeatable rate of loading. The slack adaptor also allows a reduction of the out of plane movement of the specimen. Figure 3.10 shows two representative curves of the out of plane movement caused by the two different systems on GFRP specimens, calculated using Stereo DIC.

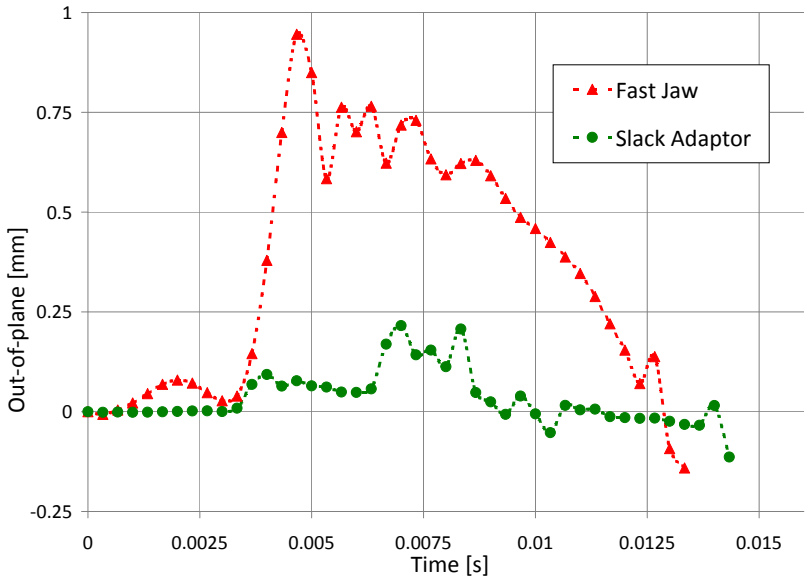

Figure 3.10: Out of plane movement during high speed testing

It can be easily seen how the slack adaptor allows a better loading of the specimen with moderate out of plane movement. Considering a camera stand-off distance of 900 mm, using Equation 2.10, it can be calculated that the parasitic strain caused by the fast jaw system and the slack adaptor are 1111 and 278 µεrespectively. It can therefore observed that the parasitic strain caused by the out of plane movement generated using the fast jaw system is above value of the strain resolution of the full-field strain measurement techniques used in the research, and therefore unacceptable.

Figures 3.11 and 3.12 show the stress-strain graph obtained with strain gauges bonded on the front and on the back of GFRP specimen and with Stereo DIC.

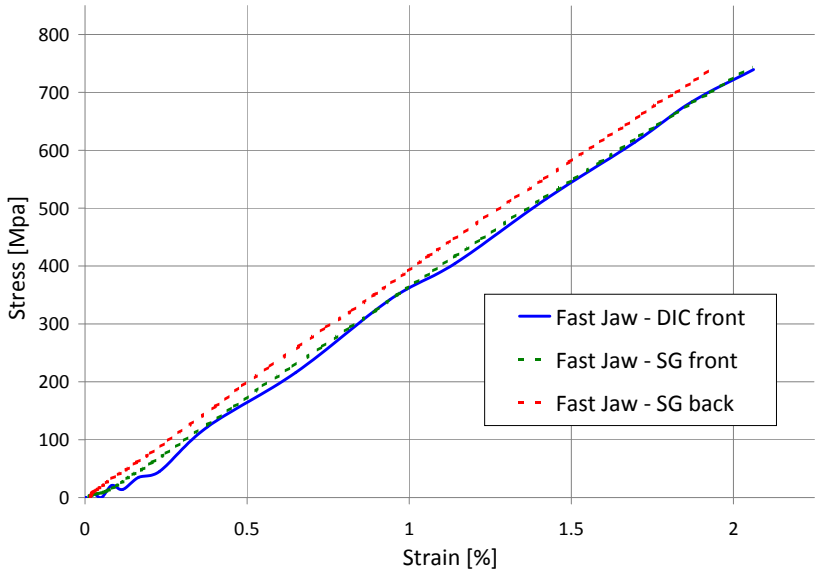

Figure 3.11: Stress-Strain curves obtained from a high speed test run using the fast jaw system

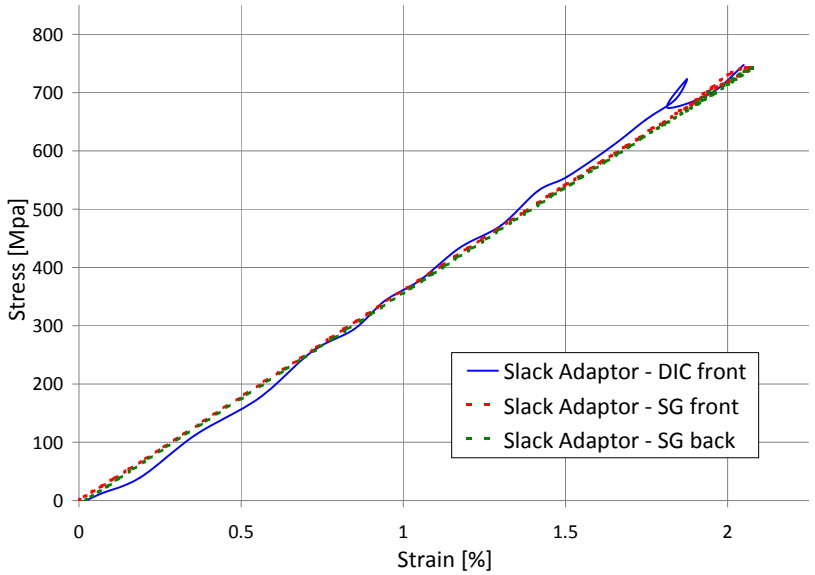

Figure 3.12: Stress-Strain curves obtained from a high speed test run using the slack adaptor system

Comparing the two graphs it appears evident how the fast jaw system causes a bending of the specimen that results in different shape of the stress strain curve evaluated using the strain gauges on the front and on the back of the specimen as shown in Figure 3.11. For slack adaptor, the curves obtained from the front and the back strain gauge can be perfectly superimposed meaning that there is no bending of the specimen caused by the clamping system.

In conclusion, by reducing slippage and out of plane movement, it is thereby shown that the slack adaptor offers better control and repeatability of high rate uni-axial tensile tests on standard size specimens. In addition, the set-up time is reduced, improving test efficiency. As this system was developed in parallel with the research presented here, different versions of this system are used in the various tests that are presented below, although operationally identical.

Slack adaptor dynamic response study

Ansys 14.0 is used to study the dynamic response of the slack adaptor system. An idealisation of the slack adaptor system is shown in Figure 3.13.

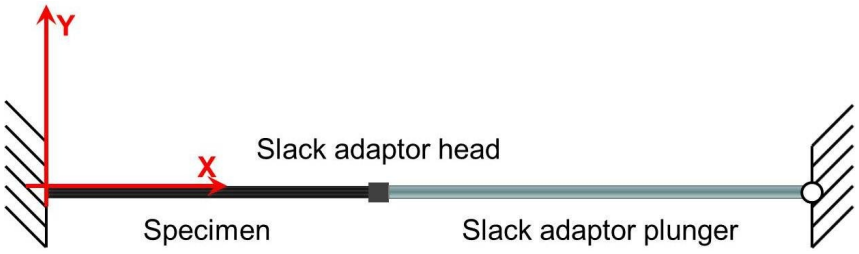

Figure 3.13: Idealisation of the slack adaptor for dynamic response study

The specimen and slack adaptor plunger assembly, shown in Figure 3.9, can be seen as two beams in series connected by the clamping system, mounted on the head of the slack adaptor plunger, where the majority of the mass is concentrated. 150 BEAM4 elements are used to model the specimen and the plunger of the slack adaptor defining the inertial and stiffness properties. Element MASS21 is used to model the concentrated mass. The free end of the specimen is constrained as fixed, all rotations and all displacements are prevented, the free end of the slack adaptor is hinged, all the rotations are free and all the displacement are prevented. Two analyses are run to understand the behaviour of the specimen-slack adaptor system to a dynamic load. A preliminary modal analysis is run to identify the fundamental frequencies of the system, a harmonic response analysis is then run to identify the impulse response of the system. During the work described in this thesis specimens with various inertial and stiffness characteristics are used: it is impossible to present all the situations. By means of example two studies are presented, with unidirectional CFRP and GFRP specimens whose characteristics are presented in Table 3.9. Analyses are presented at a later stage where the experimental results require an interpretation involving the dynamic response.

Table 3.9: Geometric and mechanical characteristics of the model

		Slack adaptor plunger	CFRP specimen	GFRP specimen
Length	[mm]	200	120	120
Width	[mm]	-	15	15
Thickness	[mm]	-	1	1
Diameter	[mm]	20	-	-
Density	[kg/m^3]	2810	1500	2500
Young's modulus	[GPa]	72.5	125	40
Poisson's ratio		0.3	0.3	0.3

The results of the modal analysis are presented in Table 3.10, where the first 10 natural frequencies and their characteristics are summarised. In the column 'Part', when both the plunger and the specimen are involved in the dynamic this is noted as 'All', when only the specimen is involved this is label 'Spc'. 'Flex' identifies flexural and 'Tors' torsional responses. 'Uy' and 'Uz' are the directions of the vibrations as identified in Figure 3.13.

Table 3.10: Modal analysis results

	CFRP				GFRP			
Mode	Freq. [Hz]	Part	Shape	Dir.	Freq. [Hz]	Part	Shape	Dir.
1	5.5	All	Flex	y	3.1	All	Flex	y
2	59.7	Spc	Flex	y	27.1	Spc	Flex	y
3	78.2	All	Flex	z	45.4	All	Flex	z
4	162.0	Spc	Flex	y	72.9	Spc	Flex	y
5	316.2	Spc	Flex	y	141.8	Spc	Flex	y
6	521.7	Spc	Flex	y	233.8	Spc	Flex	y
7	553.3	All	Tors	x	321.0	All	Tors	x
8	778.3	Spc	Flex	y	348.7	Spc	Flex	y
9	797.6	All	Flex	z	396.0	All	Flex	z
10	1006.4	All	Flex	y	486.7	Spc	Flex	y

The mechanisms that could trigger the natural response of the slack adaptor and specimen system can be identified in the locking between the internal plunger and the outer cylinder of the slack adaptor, as shown in Figure 3.14. The possible fulcrum of the moment is marked with the letter F and the consequent moment is identified as M. It is important to remark that the natural modes with a natural frequency lower than 100 Hz cannot be observed as the characteristic time of the vibration is comparable with the observation time, i.e. the duration of the high speed tensile test.

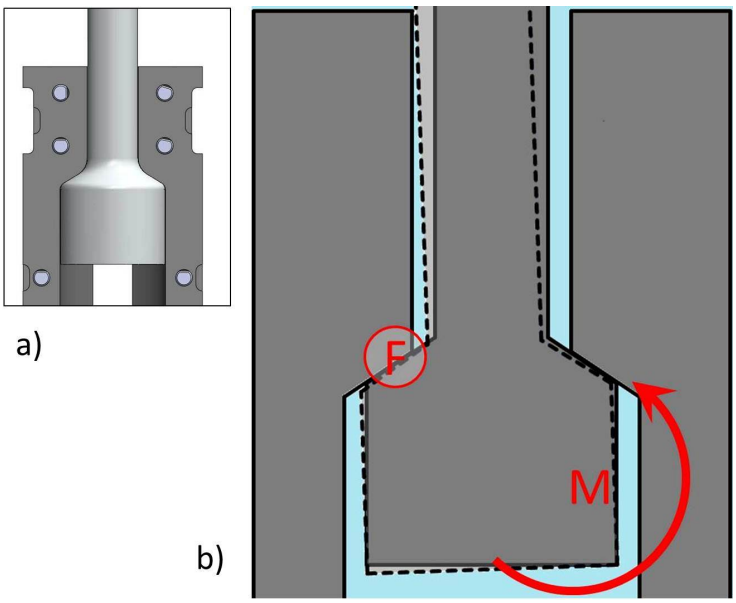

Figure 3.14: Plunger and outer cylinder contact point:
a) Drawing
b) Idealisation of the moment generation

There are two kinds of loads that are created by the locking of the internal plunger and the outer cylinder: the tensile load that is the goal of this experiment, and a moment that can be caused by a misalignment of the two parts. A harmonic analysis is therefore run to identify how and which one of these loads are affecting the dynamic response of the system. In the harmonic analysis the tensile load, modelled as a 20 kN force acting along the x axis, does not trigger any of the natural responses of the system. It has to be remarked that in this case the constrain on the displacement along the x axis at the free end of the plunger has been removed. The effects of the moment that can be generated by the locking of the two parts of the slack adaptor are simulated by applying a M_y and a M_z 400 Nm moment (considering a 20 kN force acting on a lever-arm of 20 mm) at the hinged end of the slack adaptor, as shown in Figure 3.15. No damping is used in the analysis. The results of the harmonic analysis are calculated at the nodes corresponding to the concentrated mass, the half and the two thirds of the specimen length (A, B and C in Figure 3.15).

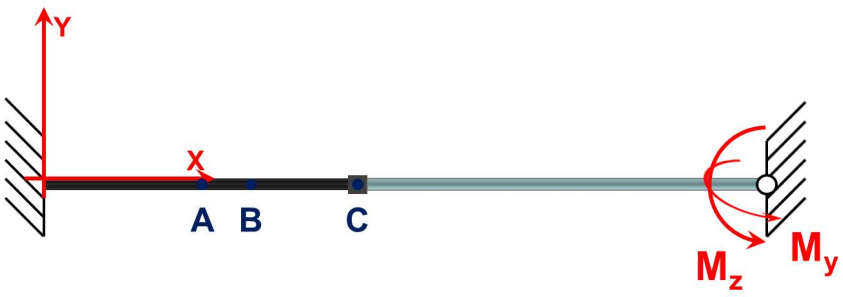

Figure 3.15: Slack adaptor dynamic response study

The frequency of the peaks of response to the applied moments from the harmonic analysis are shown in Table 3.11.

Table 3.11: Modal analysis results: frequency of the peaks of response as consequence of the applied moment [Hz]

Mode	CFRP		GFRP	
	M_y	M_z	M_y	M_z
	[Hz]		[Hz]	
1	-	5.5	-	3.1
2	-	59.7	-	27.1
3	78.2	-	45.4	-
4	-	162.0	-	72.9
5	-	316.2	-	141.8
6	-	521.7	-	233.8
7	-	-	-	-
8	-	778.3	-	348.7
9	797.6	-	396.0	-
10	-	1006.4	-	486.7

It can be concluded that all the natural modes of the slack adaptor-specimen system are triggered by a moment generated at the root of the plunger when engaging with the outer cylinder. To mitigate the problem of the dynamic response of the slack adaptor a rubber damper is placed between the plunger and the outer cylinder of the slack adaptor. This damps the vibrations, but only partially resolves the problem of generating a moment when slack adaptor engages. The effects of the rubber dumper on the initial loading rate are negligible. The effects of the slack adaptor dynamic response on the experimental outputs will be discussed further in Section 5.4.5.

It is also possible to calculate the frequency, ω_{Long}, of the longitudinal stress wave travelling trough the system as:

$$\omega_{Long} = \frac{1}{2\ L}\sqrt{\frac{E_M}{\rho_M}} \tag{3.2}$$

Where L is the travelling length, E_M and ρ_M are the material Young's modulus and density. It is expected that, when the plunger and the outer cylinder engage, a stress wave starts to travel through the plunger. When the wave reaches the end of the plunger it is partially reflected back into the plunger and partially transmitted to the specimen. It is possible to calculate the frequency of the waves travelling in the plunger and in the specimen and in the whole assembly. The results are reported in Table 3.12.

Table 3.12: Longitudinal resonance frequencies in [kHz]

CFRP specimen	Slack adaptor plunger	GFRP specimen
Parts		
30	12.7	16.7
CFRP specimen and plunger assembly		
9.5		-
GFRP specimen and plunger assembly		
-	7.2	

During this research the effects of the stress waves were never observed. The frequency of the stress waves in the specimen is comparable with the frame rate of the cameras and therefore, accordingly to the Nyquist-Shannon sampling theorem, they cannot be observed. Moreover stress waves are damped when they are transmitted from the plunger to the specimen and when they are travelling through the system, reducing the duration of their effects and making it difficult to be detected with optical measurement techniques. Finally, also in the signals recorded with the data acquisition systems of Instron VHS the effects of the stress waves was never observed during this research.

Furthermore when the plunger and the outer cylinder engage, the former is accelerated and, because of its mass, responds with inertia. This affects the load and strain rate, as will be shown in Section 4.2.4.

3.3.3 Specimen Design

When using traditional bonded end-tab specimen in high speed testing the early debonding of the end-tab from the specimen has an effect on the specimen loading, as already mentioned when commenting on Figure 3.8. During the debonding phase the energy that the actuator displacement transfers to the specimen is not used in deformation, but instead for the creation of the new debonded surface, the specimen therefore experiences a rigid body motion but is not deforming, as show in in Figure 3.16. Furthermore when the end-tabs shears off the specimen, part of the elastic energy stored in the end-tabs is released back to the load cell. This perturbs the load signal, as can be observed in Figure 3.8.

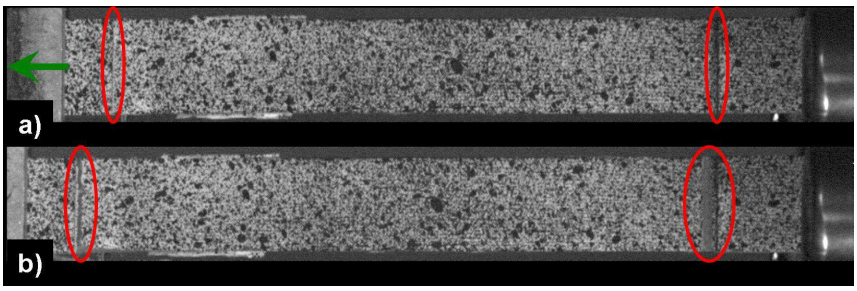

Figure 3.16: End-tab debonding:
a) The end-tabs are bonded to the specimen;
b) The specimens shears against the end-tab.

To mitigate the effect of the end-tab debonding a co-cured end-tab specimen was devised adding extra plies in the stacking sequence at the two extremities of the specimen. In this way the two extremities, after the curing, are thicker than the gauge area and offer a suitable area to grip the specimen to the machine. To be able to cure a laminate with a variable thickness the vacuum bag lay-up is adapted by adding an extra tool to maintain adequate curing pressure to the whole laminate surface and to avoid bending in the gauge area. The vacuum bag lay-up is shown in Figure 3.17.

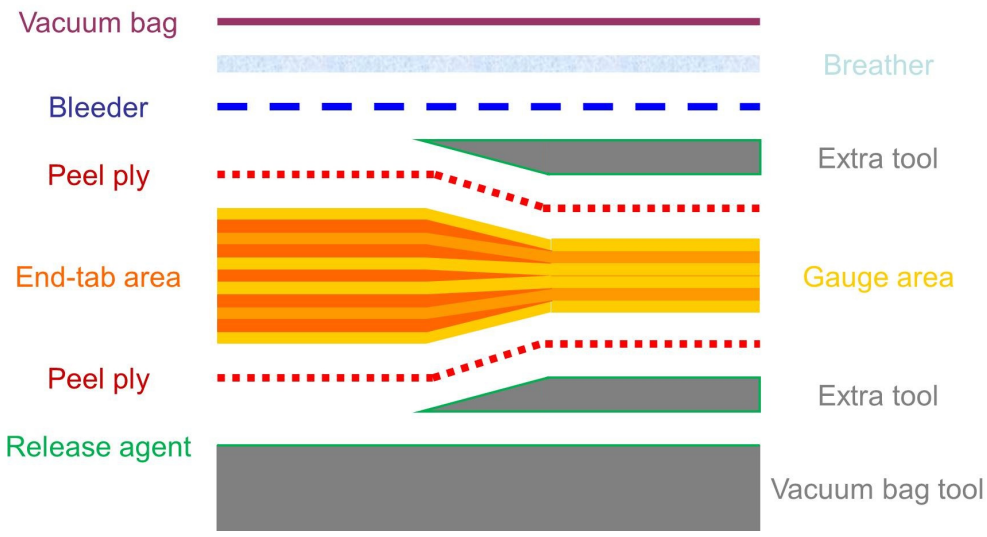

Figure 3.17: Schematic of the vacuum bag lay-up to produce co-cured end-tab specimens.

Time-stress curves obtained from GFRP specimen with bond and co-cured end-tabs are shown in Figure 3.18.

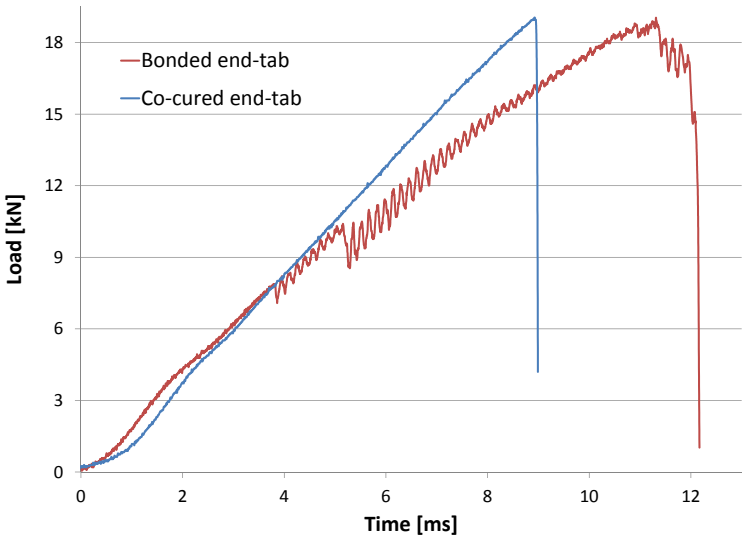

Figure 3.18: Time-Load curves for bonded and co-cured end-tab specimens

The benefits of the co-cured end-tab specimen appear evident. Considering the curve relative to the bonded end-tab specimen the linear elastic part is interrupted by a kink in correspondence with the debonding of the end-tab from the specimen. After this moment the load is oscillating around a linearly growing value, this is due to the fact that, after the debonding, the stiffness of the system changes and energy is realised into the load cell that is subject to ringing. The load curve relative to the co-cured end-tab does not show anomaly: co-cured end-tabs allow a better loading of the specimen, the load is correctly applied to the specimen during the test entire duration, the load cell ringing is significantly reduced during the test, and better stress-strain curves are obtained.

3.4 Optical techniques integration

3.4.1 High speed imaging devices

To perform material characterisation experiments at high strain rate using optical techniques to measure strain it is necessary to acquire images at high frame rates. Before the introduction of electronic photography, mechanical devices, such as rotary prisms and rotating mirrors, were used to impress images at high frequency on photographic film. Nowadays various electronic devices are used to capture and digitise images:

- CCD: charge-coupled device are constituted by a photo-active region where an electric charge proportional to the light intensity is accumulated on a capacitors array. The charge is then dumped into a charge amplifier, which converts the charge into a voltage. The image that is projected on the focal plane of the

device is therefore discretised in an array of digital signals, i.e. pixels, each one corresponding to one of the sensors of the CCD array. Several solutions are used to improve the quality of the captured images and the achievable frame rates:

  - Gated Intensified CCD: an image intensifier is used to amplify the image signal before it is recorded by the CCD sensor.
  - IS-CCD: In Situ storage CCD chips, the charge of each pixel is locally recorded on memory units located on the CCD sensor.
  - Rotating Mirror CCD: an array of CCD sensors is arranged around a rotating mirror that projects the images of the event to each one of them.

- CMOS: arrays of complementary metal-oxide semiconductors based sensors are used to capture light energy at high frame rates and convert it to a voltage that is further converted in a digital image. These sensors allow the reduction of the level of noisiness in the images avoiding the overflow of the capacitors, as it might occur in CCDs based sensors.

All the high frame rate cameras used during this research, listed in Table 2.1, are equipped with CMOS based sensors.

3.4.2 Application of DIC and GM to FRP testing at high speed

Despite the advantages of full-field optical techniques not many studies on composite materials have been carried out with the aid of DIC at intermediate or high strain rates.

Lee *et al.* in [72] and [73] conducted a study on the fracture behaviour of CFRP materials. A 2D DIC method was used to obtain time-resolved, full-field, in-plane surface displacements on specimens subjected to quasi-static and impact loads. A drop tower apparatus was used to impact notched specimens at low-velocity, the notches were oriented to produce mode-I or mixed-mode (mode-I and -II) fracture. The images were recorded using a rotating mirror ultra high speed camera, DIC was performed with an in-house developed software based in Matlab. The authors were able to extract the stress intensity factor and define the crack extension histories from the full-field displacement fields, proving the feasibility of studying stress-wave induced crack initiation and rapid crack growth in fibre-reinforced composites using DIC and high-speed photography. In a following work Lee *et al.* [74] carried out, using the same apparatus and methodology, dynamic fracture tests to compare the fracture parameters of unidirectional IM7/PETI-5 and T800/3900-2.

DIC has been used by Hufner and Accorsi [75] to experimentally validate their progressive failure theory for woven FRP materials subjected to dynamic load. The

proposed theory, capable of predicting fully non-linear, rate dependent, anisotropic behaviour for dynamic loading, was experimentally validated using basic tension and open hole tension experiments with the aid of DIC. A servo-hydraulic test machine was used to generate strain rates between 0.0001 and 0.1 s^{-1}, while images were captured with a high speed camera at frame rate ranging from 10 to 2000 Hz. The authors identify the benefits of DIC as:

- the availability of the full strain-displacement field;
- the possibility to experimentally determine all the components of strain (normal and shear) on the measured surface;
- the ability to accurately measure low strains, as well as extremely large strains, within a single test.

These characteristics were deemed particularly helpful in developing a constitutive theory. The knowledge of strain components, and their spatial variation, on the fully measured surface is better than the local values obtained for example with strain gauges. This technique allowed the acquisition of data that are accurate enough to extract the material constitutive parameters and model the material behaviour. To gather these data using strain gauges a high number of sensors and experiment repetitions would have been required. It has to be remarked that these benefits are associable with other full-field strain measurement techniques.
Koerber *et al.* [61] used DIC to investigate the strain rate effects on CFRP, as described in Section 3.2. A SHB was used to load the specimen at strain rates up to 350 s^{-1}, while images were recorded with a high speed camera operated at a frame rate of 100 kHz. DIC allowed the measurement of in-plane strain field on the surface of the specimen and to monitor the failure process.
Palanivelu *et al.* [76] used a high speed camera, operated at a frame rate of 2 kHz, to calculate the impact speed, the corresponding deceleration and impact force in their investigation on the behaviour of uni-directional pultruded composite tubes subjected to an impact load. The authors identified the benefits of DIC, compared to contact sensors, in the higher flexibility offered by this technique that avoided the risk of loss of sensors and equipment due to an improper selection.
The capability of Stereo DIC to measure out of plane movement and strain was exploited by Pankow *et al.* [77] to study the shock response of 3D woven composites. Using a shock tube loaded with high pressure gas and high frame rate cameras the authors were able to study the strains in the matrix and in the tow caused by a shock wave and, in particular, the role of the 3D structure in the failure initiation and damage containment.
Berthe *et al.* [52] used DIC for the validation of a new specimen geometry that allows

the visco-elastic behaviour characterisation of FRP in a strain rate range from 10^{-3} to 10^{2} s^{-1}. Stereo DIC allowed the measurement of the out of plane displacements and the strains from the displacement field. The homogeneity and the consistency of the strain on the surface of the proposed specimen was verified.
Broadening the application of DIC to non polymeric matrix composites, the strain field of fibre reinforced cement specimens during high speed tensile tests have been recorded by Silva *et al.* [78], allowing the observation of the rotation of part of the composite after crack formation resulting in different strain levels in different regions of the material. Zhu *et al.* [79] used DIC to verify the accuracy of a linear variable differential transformer (LVDT) mounted on the actuator of a servo-hydraulic high rate testing machine. In both [78] and [79], tensile tests were performed on sisal fibre reinforced cement composite at strain rates up to 25 s^{-1}, images were acquired at a frame rate of 10 kHz.
Finally, in their attempt to use Palmetto wood as a template to guide the development of more impact resistant polymer composites, Haldar and Bruck [80] used DIC to measure the flexural strain of a specimen during an impact three-point bending test, with strain rates up to 100 s^{-1}. the images obtained with a high speed camera were used to evaluate the projectile velocity, as well as the strains.

Even less application of the GM to FRP testing at high speed can be found in the literature. Moulart *et al.* [81] and [21] used a Cordin 550-62 rotating mirror ultra high speed camera to apply the GM to GFRP specimens tested in a SHB and to identify the dynamic material stiffness.

3.4.3 Data synchronisation

For the high speed tensile tests a major challenge is the synchronisation of the data collected from independent systems, i.e. strain gauge, Instron VHS and cameras. Various experimental set-up have been tried in the early stages of this project, as describe in Crump *et al.* [82]. The schematic of the experimental set-up used to perform the tests presented in this research is shown in Figure 3.19.

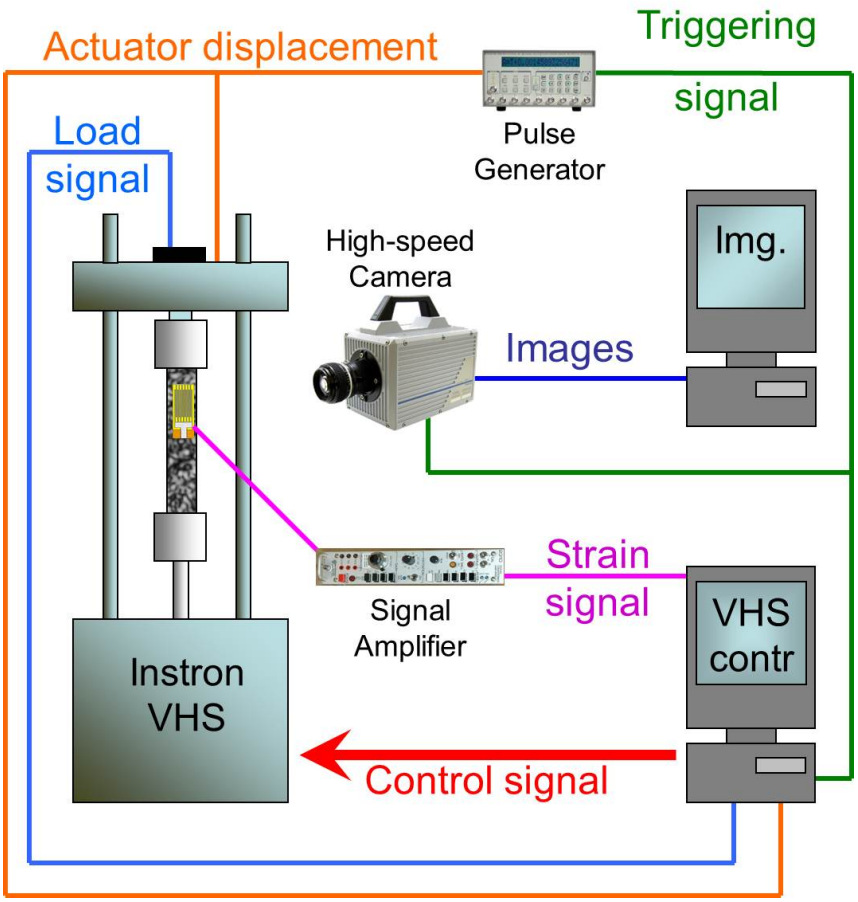

Figure 3.19: Schematic of the experimental set-up

In this configuration a pulse generator is used to generate a triggering signal that works as time-zero for the two systems. The actuator displacement signal is sent to the pulse generator, when a certain displacement is reached, i.e. the slack adaptor is about to engage, the pulse generator sends a triggering signal that starts the Instron VHS data recording system and the camera at the same time. In this way, knowing the sampling frequency of the two systems is possible to associate the image, and therefore the calculated strain, with the corresponding load.
One channel of VHS data acquisition system is used to record the the strain gauge signal, previously conditioned using a Vishay 2311 signal amplifier. A single strain gauge is used in a quarter Wheatstone bridge configuration to measure the tensile strains.

3.4.4 Illumination

The three different illumination systems described in Section 2.2.1 are here compared in terms of suitability to perform consistent and repeatable high speed tests. A simple experiment has been run illuminating one CFRP and one GFRP unidirectional specimen equipped with a Vishay CEA-06-240UZ-120 strain gauge. The

surface of the specimen has been prepared with a DIC speckle pattern. The temperature variation of the air around the specimen has also been recorded using a thermocouple. The results of the experiment run using three halogen light placed at a distance that assures a correct illumination of the specimens for high speed imaging are shown in Figure 3.20. The results for the fibre optic illuminators and the LED light are not reported as no significant increase in the temperature and strain drift have been recorded.

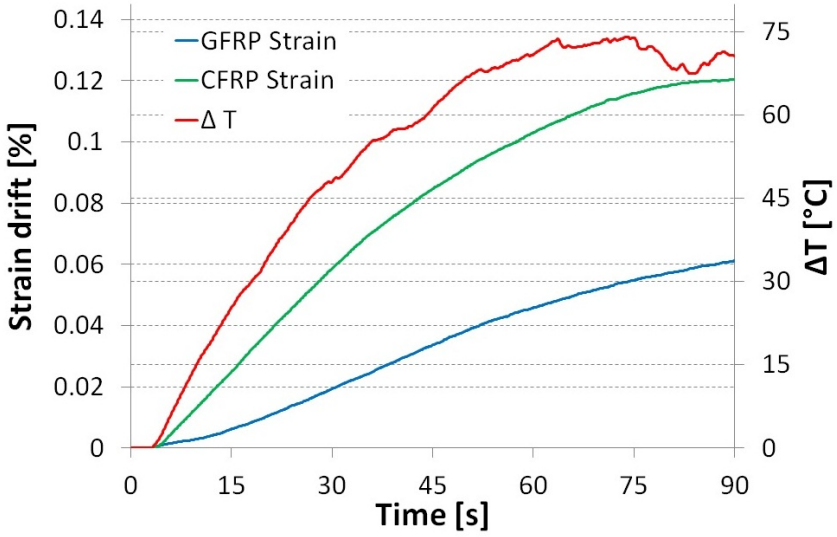

Figure 3.20: Thermal effects of the illumination with halogen light.

The temperature rapidly increases after the halogen lights are switched on, as shown by the red line in Figure 3.20. This leads to a heating of the specimens, dependent on the heat absorption factor of the material, that modifies the behaviour of the material itself. Furthermore a temperature dependent strain drift can be observed, this is cause in first instance by the heating of the strain gauge, and by the thermal expansion of the material. The usage of halogen lamps therefore affects the experimental results as it modifies the material behaviour and causes incorrect strain measurements. As it is not possible to control the time interval that the specimen is exposed to the illumination before the test is run and as the temperature varies during the experiment itself the halogen lights are not suitable to illuminate the specimens during high speed tensile tests. Moreover the halogen lights heat up the air between the cameras and the specimen, which causes the refractive index of the air to change, generating a distortion in the acquired images.

The considerations about the light positioning drawn in Section 2.3.4 are applied to high frame rate image acquisition using the cold light sources described in Section 2.2.1.

The high-speed test set-up with Schott KL 1500 fibre optic illuminator for 2D DIC and GM is shown in Figure 3.21.

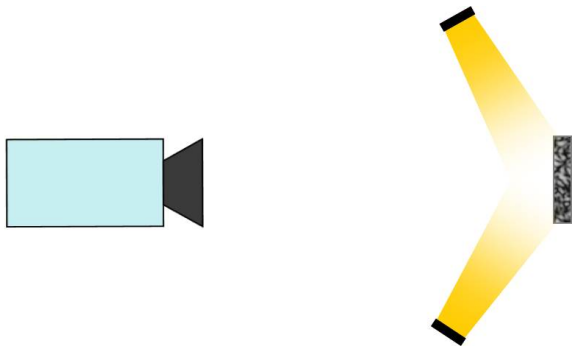

Figure 3.21: Schematic of the experimental set-up for 2D DIC and GM on Instron VHS with fibre optic illuminator

As explained above the fibre optic illuminator ensures that no heat is transferred to the specimen, the light source is placed outside the testing area therefore no heat waves affect the imaging process.

The high-speed test set-up with LED light for Stereo DIC is shown in Figure 3.22.

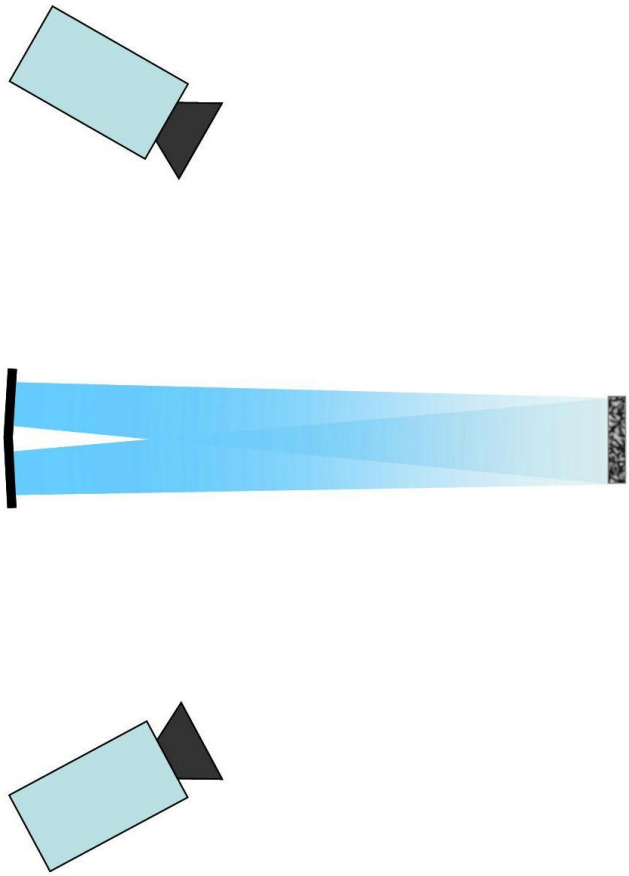

Figure 3.22: Schematic of the experimental set-up for Stereo DIC on Instron VHS with LED light

When positioning the LED light it must be taken into account that the heat-sinks of the illuminating system might produce heat waves that can distort the images. Therefore the light must be put in a position that does not interferes with the imaging process.

3.4.5 Final considerations

Among the parameters that have to be taken into account when collecting images for strain measurement three have particular relevance when performing high speed imaging:

- Resolution and frame rate compromise: the images have to be acquired with a sufficient resolution to perform image analysis but at a frame rate that allows useful stress-strain curves to be drawn.
- Shutter speed: the exposure time must be calibrated in such a way that allows sharp images to be acquired but also with an appropriate grey scale distribution to perform image analysis.
- Illumination: the fast shutter speed and the need of an aperture diameter that ensures a deep DOF make necessary to provide an illumination intense enough to acquire images with a correct grey scale distribution.

To maximise the quality of the images, it is suggested to use the most intense illumination possible and adjust the grey scale distribution by reducing the shutter speed and the lens aperture diameter.

3.5 Conclusion

The best solution for loading the specimen at high strain rate has been identified as the slack adaptor, that allows reproducible results to be obtained and avoids the experimental uncertainties introduced by the fast jaw system. Furthermore a novel manufacturing technique that allows the production of co-cured end-tab specimens suitable for high strain rate testing has been devised. The data synchronisation issues have been tackled and solved alongside the definition of an illumination system that ensures an unbiased behaviour of the specimen. The following guide lines can be given:

- The Slack adaptor system ensures a better loading of the specimen and reduces the out of plane movement of the specimen;

- To avoid the load cell ringing the effect of the end-tabs debonding must be eliminated using co-cured end-tab specimens;
- The pulse generator is a valuable instrument to guarantee a good data synchronisation and reliable stress-strain curves;
- As much as regards the image acquisition:
  - It is recommended to try to maximise the sampling frequency of the data acquisition system and the camera frame rate;
  - It is necessary to reach the right compromise between the spatial and the temporal resolution of the camera;
  - A high intensity cold light source reduces the alteration of the material behaviour and allows to set-up the camera to obtain a deep DOF and a fast shutter speed.

4 Experimental methodology validation through material characterisation

4.1 Introduction

The experimental methodology developed in the previous chapter is validated here through the identification of the longitudinal elastic modulus E_{11} of GFRP specimens. The experimental guidelines developed in Section 3.5 are here applied to a series of characterisation tests that rely on DIC and GM to measure the strain. Three different sets of specimen are used:

- Dual-technique specimens, with half of the surface prepared for DIC and half for the GM. These allow to directly compare the accuracy of the two strain measurement techniques while evaluating the out of plane movement of the specimen and its impact on the measurement error with Stereo DIC.
- DIC only specimens.
- GM only specimens.

The last two are used, in the same testing campaign, to compare the DIC and the GM in terms of data quality and user friendliness. The output of the tests are finally used to inform a model of the strain rate dependent behaviour of the GFRP material.

4.2 Experimental work

The results of the two different test campaigns, the one on the dual-technique specimens and the one on the DIC-GM only specimens, are presented. These are based on the same experimental set-up and the same specimen characteristics. Ultimately, the two experimental campaigns share the same aim to retrieve the Young's modulus of the investigated GFRP material.

4.2.1 Specimens preparation

The specimens are manufactured with MTM28-1/E-GLASS-200-32%RW (Advanced Composites Group - Umeco) pre-preg material stacked in a unidirectional lay-up and cured accordingly to the manufacturer's specification. A schematic of the specimen with the reference system used in this chapter is shown in Figure 4.1.

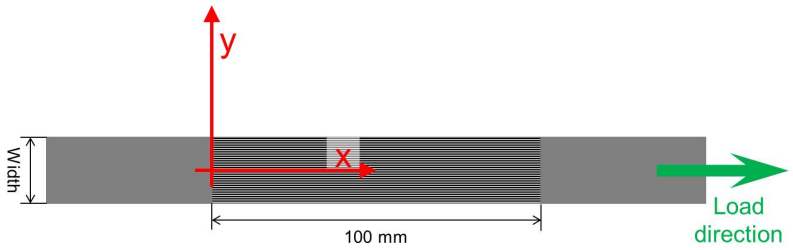

Figure 4.1: GFRP specimen and reference system

The dual-technique specimens have width of 15 mm while the DIC and GM specimens of 20 mm.

A Vishay CEA-06-240UZ-120 type strain gauge was bonded in the centre of the gauge area of each specimen. This kind of gauge is a standard strain gauge that can withstand strains up to 3-5% and are made of a 6 mm active grid on a polyimide backing. To ensure a correct adhesion between the strain gauge and the specimen the bonding surface was prepared accordingly to the strain gauge manufacturer's directions and bonded using a cyanacrilate based adhesive.

The number of specimens tested and the relative actuator speed are summarised in Table 4.1.

Table 4.1: GFRP specimens and actuator speed

Specimen type	Number of tested specimens	Actuator speed [m/s]
Dual-technique	4	0.001
	4	1
	4	3
Only DIC	2	Quasi-static
	4	0.008
	4	2
	4	8
Only GM	2	Quasi-static
	4	0.008
	4	2
	4	8

A dual-technique specimens is shown in Figure 4.2.

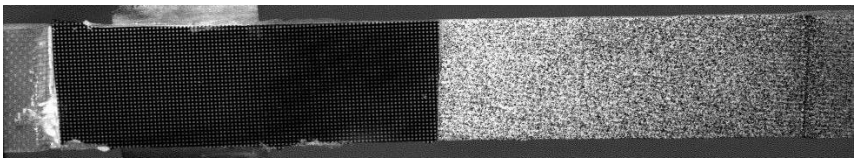

Figure 4.2: Dual-technique DIC-GM specimen

In Table 4.2 the surface preparation and the test set-up time for DIC and GM specimen are summarised.

Table 4.2: Experimental time

Task	Time [min]
DIC	
Speckle pattern application	10
Calibration images acquisition	15
Specimen alignment	5
Total	30
Grid Method	
Grid-specimen alignment	30
Epoxy resin curing	2400
Specimen alignment	15
Total	2445

The preparation of the specimens for the GM is both more labour intensive and time consuming. Beside the time required to cure the epoxy resin to transfer the grid on the specimen, it is necessary to align the grid to the specimen edge to make sure that the grid lines are parallel and perpendicular to the deformation directions. Beside this it can happen that the grid is not correctly transferred to the specimen surface, as shown in Figure 4.3, creating areas where the deformation cannot be evaluated.

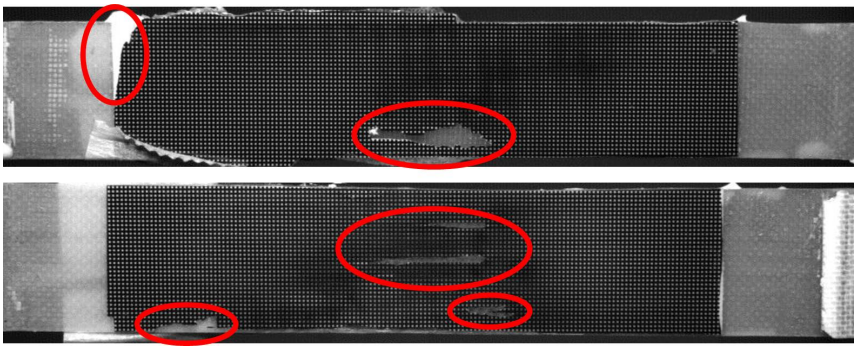

Figure 4.3: Grid transfer defects

Furthermore when each specimen is gripped on the machine it is necessary to control that the grid is sampled by an exact number of pixels and it is aligned with the array of pixels of the imaging sensor, as described in Section 2.4.5. When preparing the speckled surface of the specimen there is no risk of not covering the whole specimen surface, if the speckle pattern is not satisfactory it is always possible to clean the specimen surface and repaint it. The only delicate operation involved in the preparation of a DIC experiment, particularly for Stereo DIC, is to correctly acquire the images required for the calibration.

4.2.2 Experimental set-up

Dual-technique specimens

The general experimental set-up was the one described in Section 3.4.3 by Figure 3.19. The set-up was modified to control two sets of cameras to measure the strain, arranged as shown in Figure 4.4:

1. A pair of Photron SA1 operated at a frame rate of 10 kHz and with a resolution of 1024 x 512 pixel for Stereo DIC.

2. A Photorn SA3 operated at a frame rate of 5 kHz and with a resolution of 1024 x 128 pixel used for the 2D DIC and the GM.

White light was provided by the Fiber-Lite PL-900 fibre optic illuminator described in Section 2.2.1.

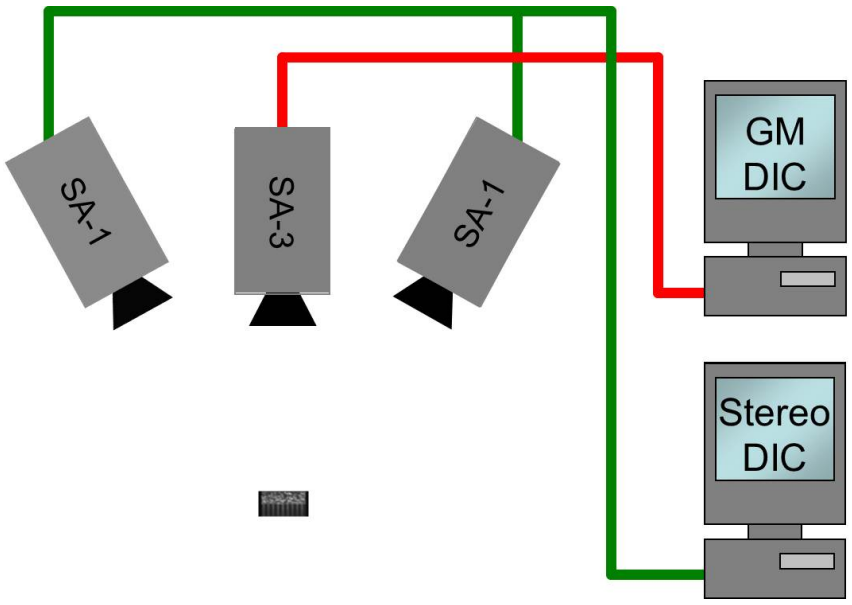

Figure 4.4: Cameras set-up for dual-technique DIC-GM specimens

Furthermore the strain was also measured using strain gauges. A Vishay 2311 signal amplifier and the Instron VHS data acquisition system, operated at a sampling

frequency of 100 kHz, were used to record the strain gauge signal.

The main characteristics of the used techniques are summarised in Tables 4.3, 4.4 and 4.5.

Table 4.3: Stereo DIC characteristics

Technique used	DIC
Subset size	31 x 31 pixels
Step size	10 pixels
Camera	Photron SA1, 8-bit
Lens	Nikkor 28-105mm f/3.5-4.5D
Resolution	1024 x 512 pixels
Field of view	112 x 56 mm
Frame rate	10 kHz
Spatial resolution	1.09 mm
Displacement resolution	0.0015 pixel
Strain resolution	33 με

Table 4.4: 2D DIC characteristics

Technique used	DIC
Subset size	15 x 15 pixels
Step size	15 pixels
Camera	Photron SA3, 8-bit
Lens	Nikkor 28-105mm f/3.5-4.5D
Resolution	1024 x 128 pixels
Field of view	13 x 104 mm
Frame rate	5 kHz
Spatial resolution	1.52 mm
Displacement resolution	0.0036 pixel
Strain resolution	155 με

Table 4.5: GM characteristics

Technique used	GM
Grid Pitch	0.254 mm
Sampling	5 pixel per period
Camera	Photron SA3, 8-bit
Lens	Nikkor 28-105mm f/3.5-4.5D
Resolution	1024 x 128 pixels
Field of view	13 x 104 mm
Frame rate	5 kHz
Spatial resolution	0.51 mm
Smoothing radius	13
Displacement resolution	0.0039 pixel
Strain resolution	477 με

For the 2D DIC the interrogation cell size was chosen to maximise the number of available data points, the interrogation cell overlapping to resemble the post-processing characteristics of the GM that does not consider any overlapping in the measurement points. The 2D strain measurement techniques, i.e. the 2D DIC and GM have comparable strain resolution.

DIC and GM only

The general experimental set-up was the one described in Section 3.4.3 by Figure 3.19. The images were taking using a single Photron SA1 high speed camera operated at a sampling rate of 20 kHz. White light was provided by the Fiber-Lite PL-900 fibre optic illuminator described in Section 2.2.1.

The main characteristics of the used techniques are summarised in Tables 4.6 and 4.7.

Table 4.6: DIC characteristics

Technique used	DIC
Subset size	16 x 16 pixels
Step size	16 pixels
Camera	Photron SA1, 8-bit
Lens	Nikkor 28-105mm f/3.5-4.5D
Resolution	1024 x 192 pixels
Field of view	115 x 17 mm
Frame rate	20 kHz
Spatial Resolution	1.46 mm
Displacement resolution	0.0042
Strain resolution	127 με

Table 4.7: GM characteristics

Technique used	GM
Grid Pitch	0.254 mm
Sampling	5 pixel per period
Camera	Photron SA1, 8-bit
Lens	Nikkor 28-105mm f/3.5-4.5D
Resolution	1280 x 192 pixels
Field of view	115 x 17 mm
Frame rate	20 kHz
Spatial resolution	0.51 mm
Smoothing radius	13
Displacement resolution	0.0026
Strain resolution	476 με

In this case the DIC post-processing parameters were modified to try to achieve a spatial resolution and a number of data point that is as close as possible to the values obtainable with the GM measurements.

A comparison of the two 2D strain measurement methodologies leads to conclude that, even if the GM is more labour intensive and time consuming both during the preparation of the specimens and in the set-up of the experiments, as explained in Section 4.2.1, it allows to obtain a higher number of data points, i.e. higher spatial resolution.

4.2.3 Experimental results

Dual-technique specimens: stress-strain graphs

Examples of the stress-strain curves obtained with the different optical strain measurement techniques are presented below. Figures 4.5 to 4.7 show the curves obtained for actuator displacement speed of 1 mm/s, 1m/s and 3 m/s.

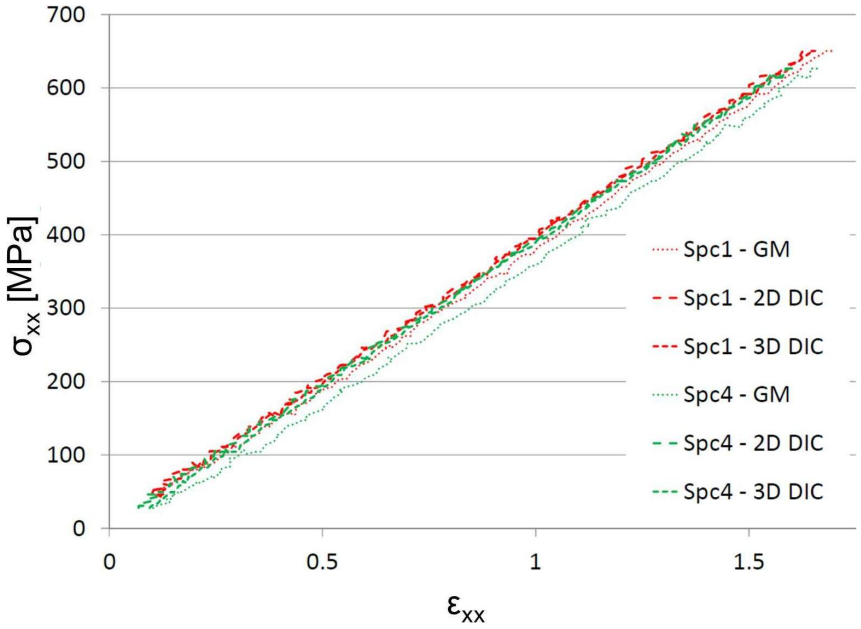

Figure 4.5: Stress-strain curves from dual-technique specimens for actuator displacement speed of 1 mm/s

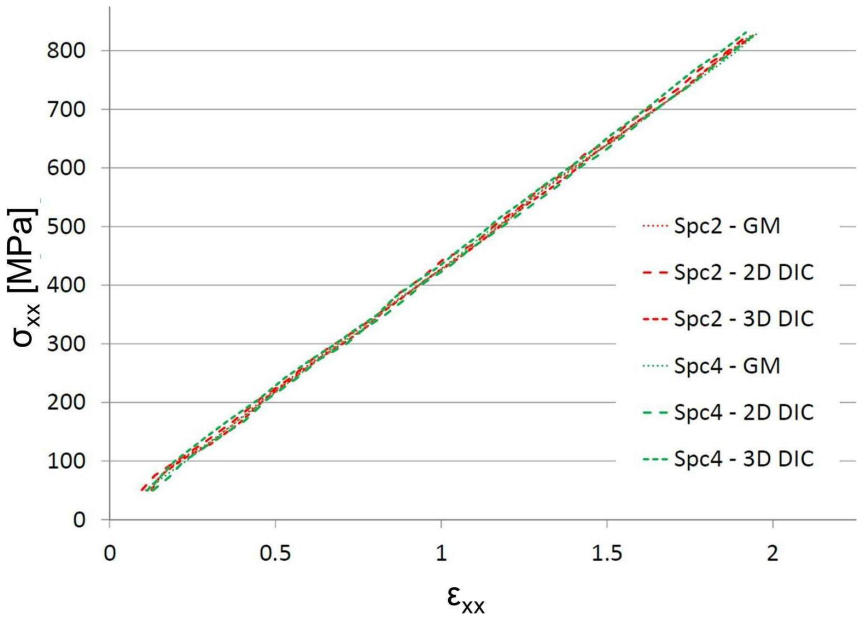

Figure 4.6: Stress-strain curves from dual-technique specimens for actuator displacement speed of 1 m/s

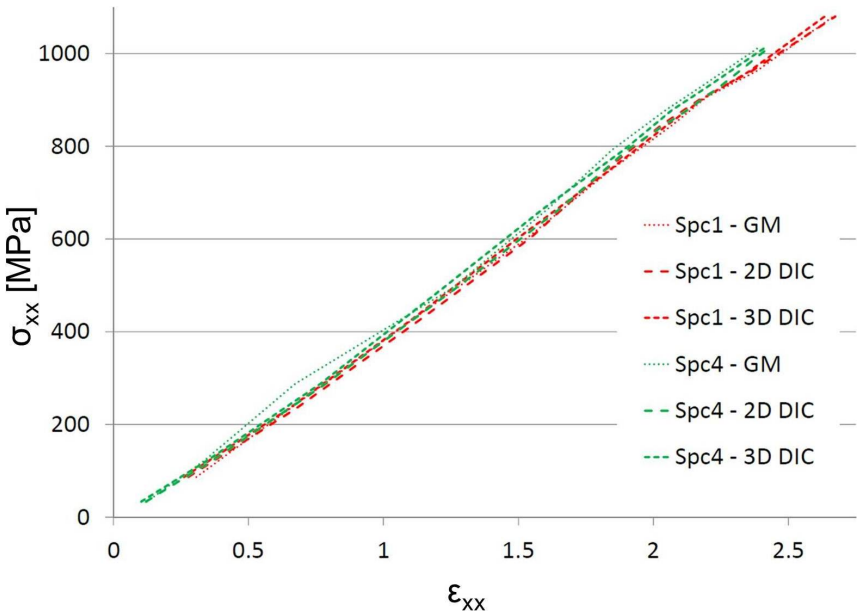

Figure 4.7: Stress-strain curves from dual-technique specimens for actuator displacement speed of 3 m/s

DIC and GM only: stress-strain graphs

Figure 4.8 to 4.10 show the stress-strain curves from the DIC and the GM data obtained for actuator displacement speed of 8 mm/s, 2 and 8 m/s.

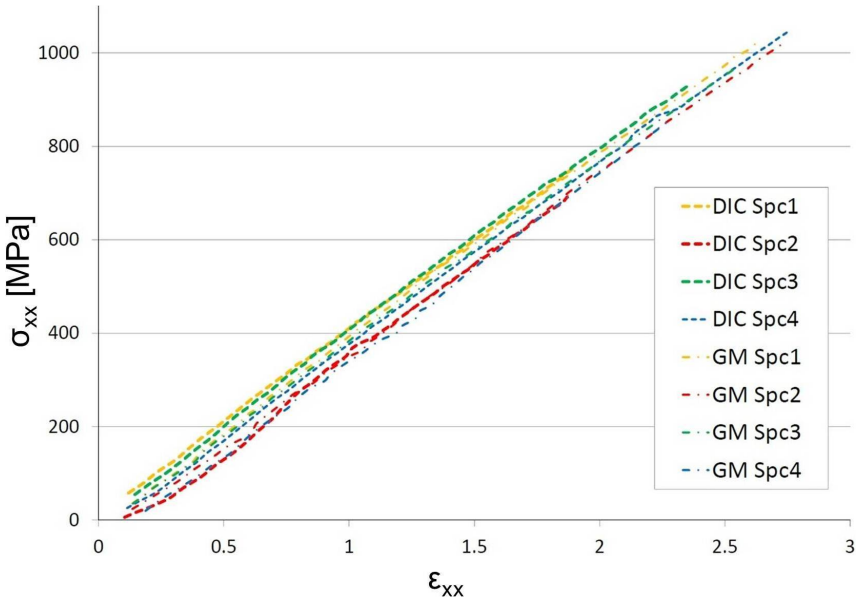

Figure 4.8: Stress-strain curve from DIC and GM data for actuator displacement speed of 8 mm/s

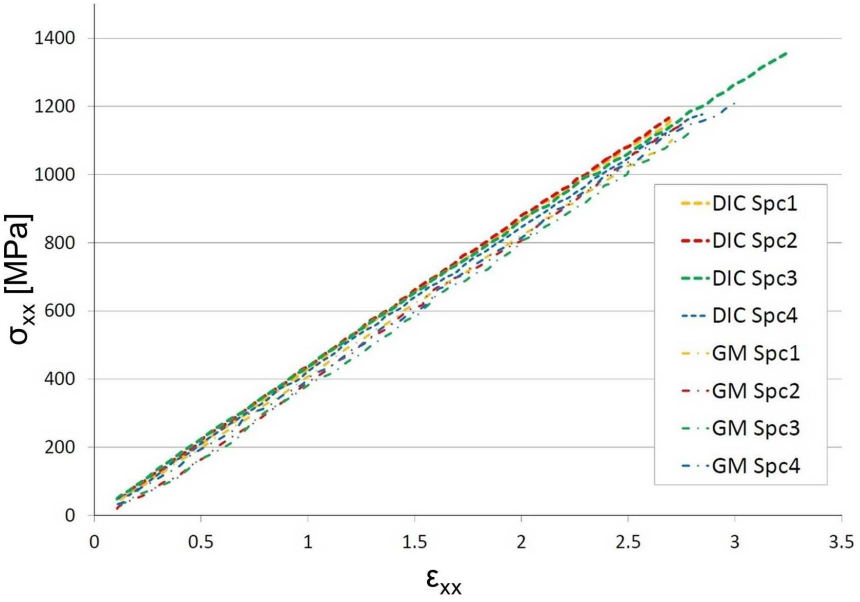

Figure 4.9: Stress-strain curve from DIC and GM data for actuator displacement speed of 2 m/s

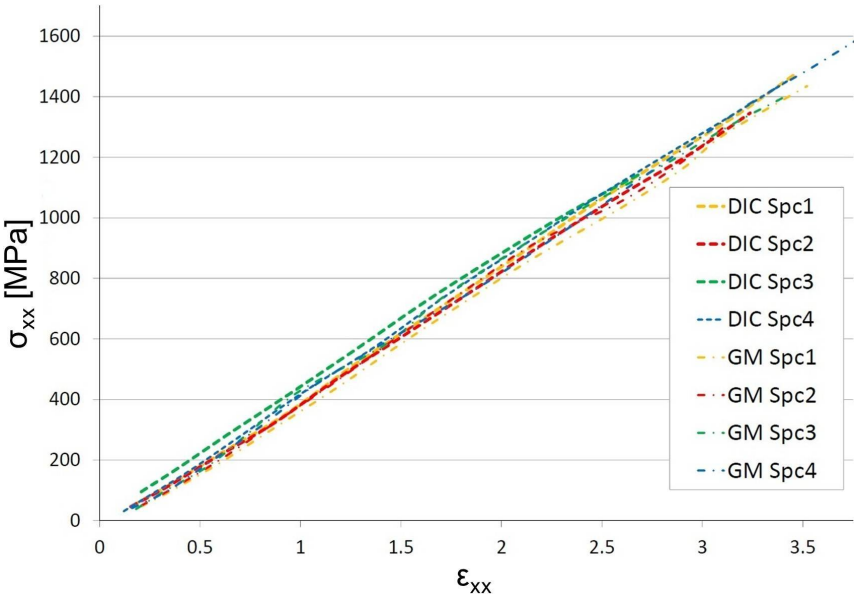

Figure 4.10: Stress-strain curve from DIC and GM data for actuator displacement speed of 8 m/s

Results summary

The maximum out of plane movement evaluated with the Stereo DIC on the dual-technique specimens are summarised in Table 4.8. Knowing that the distance the between the specimen and the imaging sensor is 1250 mm, it was possible to evaluate the parasitic strain caused by the out of plane movement with Equation 2.10 of Section 2.5, recalled below:

$$\epsilon_{parasitic} = \frac{dz}{z} \tag{4.1}$$

Where dz is the out of plane movement and z is the stand-off imaging distance.

The parasitic strain values are comparable with the strain resolution of the two 2D strain measurement techniques, and therefore the out of plane movement does not affect the strain measurement and the Young's modulus evaluation.

The Young's moduli obtained from the dual-technique specimens test campaign are summarised in Table 4.9, that allows to draw the following conclusions:

- The two 2D methods, DIC and GM, are in good agreement between each other, with a global CV lower than 0.75%.
- The results from the 2D methods are also in good agreement with the Stereo DIC, with a global CV lower than 0.75%.
- All the results are confirmed by the strain gauge readings.

The Young's moduli obtained from the DIC-GM only specimens test campaign are summarised in Table 4.10.

Table 4.8: Out of plane movement

	Actuator displacement speed					
	1 mm/s		1 m/s		3 m/s	
	Out of Plane Movement mm	Parasitic Strain με	Out of Plane Movement mm	Parasitic Strain με	Out of Plane Movement mm	Parasitic Strain με
Spc 1	0.15	120	0.39	310	0.37	290
Spc 2	0.11	90	0.48	380	NA	N.A.
Spc 3	0.16	130	0.37	290	0.69	550
Spc 4	0.19	150	0.11	90	0.11	90

Table 4.9: Young's moduli obtained from the dual-technique specimens test campaign [GPa]

	Actuator displacement speed											
	8 mm/s				2 m/s				8 m/s			
	Grid Method	2D DIC	Stereo DIC	Strain Gauge	Grid Method	2D DIC	Stereo DIC	Strain Gauge	Grid Method	2D DIC	Stereo DIC	Strain Gauge
Spc 1	38.7	39.0	38.9	38.9	42.3	42.5	42.8	42.7	42.3	42.6	42.4	42.4
Spc 2	38.9	39.3	38.4	39.4	42.0	42.3	42.0	41.8	NA	NA	NA	NA
Spc 3	38.8	39.1	39.0	38.6	42.0	42.3	42.1	42.2	42.5	42.7	42.5	42.4
Spc 4	39.0	39.3	38.8	39.2	42.2	42.4	42.7	42.5	42.7	43.1	42.9	43.0
Average	38.9	39.2	38.8	39.0	42.1	42.4	42.4	42.3	42.5	42.8	42.6	42.6
CV [%]	0.33	0.38	0.68	0.90	0.36	0.23	0.96	0.93	0.47	0.62	0.62	0.81

Table 4.10: Young's moduli obtained from the DIC and GM only specimens test campaign [GPa]

	Actuator displacement speed											
	Quasi-static			1 mm/s			1 m/s			3 m/s		
	DIC	GM	Strain Gauge	DIC	GM	Strain Gauge	DIC	GM	Strain Gauge	DIC	GM	Strain Gauge
DIC												
Spc 1	38.4	-	38.1	38.7	-	40.6	43.3	-	42.8	43.4	-	43.1
Spc 2	38.7	-	38.0	39.0	-	39.4	43.4	-	43.0	42.7	-	42.8
Spc 3	-	-	-	39.6	-	40.6	41.7	-	42.1	42.9	-	42.6
Spc 4	-	-	-	38.8	-	38.3	42.0	-	41.6	42.9	-	43.3
GM												
Spc 1	-	36.5	38.4	-	39.4	39.6	-	42.6	42.8	-	42.9	42.7
Spc 2	-	36.2	38.5	-	39.1	39.4	-	43.6	43.2	-	43.1	43.4
Spc 3	-	-	-	-	39.7	38.8	-	41.7	42.3	-	42.8	43.4
Spc 4	-	-	-	-	40.4	40.0	-	42.1	42.7	-	43.3	43.1
Average	38.6	36.6	38.3	39.0	39.7	39.6	42.6	42.5	42.6	43.0	43.0	43.1
CV [%]	0.55	0.58	0.62	1.03	1.40	2.04	2.06	1.93	1.24	0.69	0.52	0.73

The developed experimental methodology is a suitable means to study the strain rate dependent behaviour of FRP. The full-field strain measurement techniques offer a reliable mean to characterise the material behaviour at high strain rate. The slack adaptor, causes a limited out of plane movement of the specimen, that does not influence the results of 2D full-field strain measurement techniques. The co-cured end-tab allowed to avoid the load cell ringing and to obtain stress-strain curves suitable for material characterisation, as explained in Section 3.3.3. Also the cold light sources allowed to reduce the effect on the material behaviour of the illumination needed to perform full-field strain measurement techniques, as explained in Section 3.4.4. Furthermore the low coefficients of variation in Tables 4.9 and 4.10 are indicative of a good repeatability of the results obtainable with this experimental methodology. Moreover the two experimental campaign, dual-technique specimens and DIC-GM only specimens, conducted in two different times, lead to comparable results. This also proves the reproducibility of the results obtainable with the experimental methodology developed in this research.

It is possible to observe a trend in the Young's modulus value with the increase of the actuator displacement speed. The value constantly increases with the increment of the strain rate. These results are in agreement with the literature, and in particular with the work of Shokrieh and Omidi [48] and [49], presented in Section 3.2. These results will be further discussed in Section 4.3.1.

The results presented in Tables 4.9 and 4.10 will be used in Section 4.3.2 to describe the strain rate dependent behaviour of the studied GFRP material.

4.2.4 Full-field maps

From the images of specimens prepared with grids or speckle patterns, it is possible not only to obtain strain values to draw the stress-strain curves and characterise the behaviour of the material, but also to further analyse the behaviour of the specimen during the loading process. Unlike the traditional strain measurement techniques, it is possible to observe the effects of the loading over the whole specimen surface. Strain gauges, in fact, only allow to obtain punctual informations from the location where they are bonded. With full-field strain measurement optical techniques, it is possible to observe the deformation of the whole specimen while the load is applied. The displacement maps allow the evaluation of the strain maps. From the strain maps it is possible to obtain strain rate maps. The importance of these results for the experimental methodology definition and the analysis of the data is described below. Further discussion about the information that full-field data allows to obtain

will be presented in Section 5.4.4.

Displacement maps

Example of displacement maps obtained from 2D DIC and GM are shown in Figures 4.11 to 4.14 along with a schematic representing the surface area where the data are extracted.

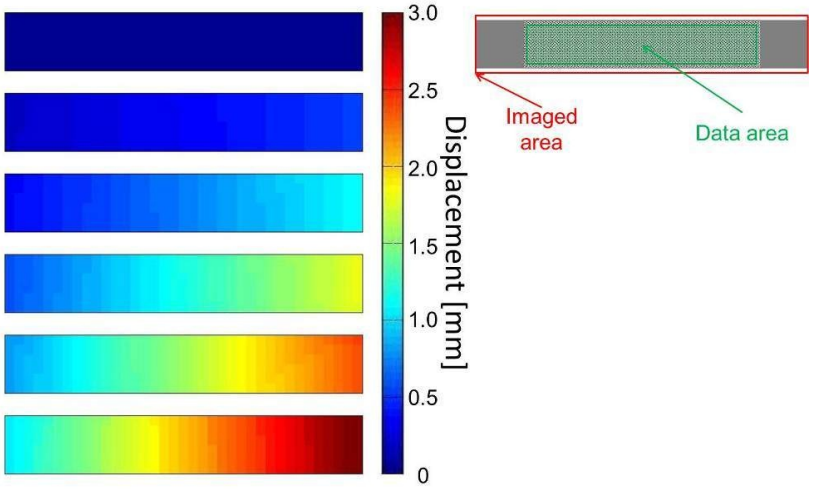

Figure 4.11: Longitudinal displacement maps from DIC for 2 m/s actuator displacement speed

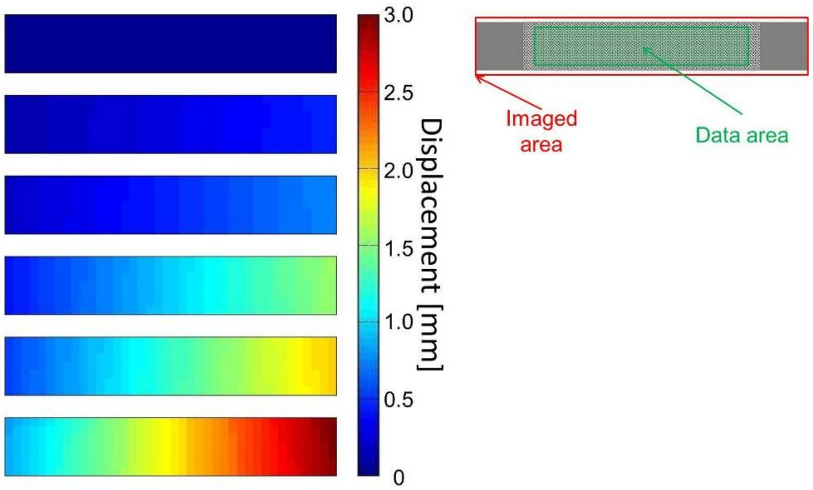

Figure 4.12: Longitudinal displacement maps from DIC for 8 m/s actuator displacement speed

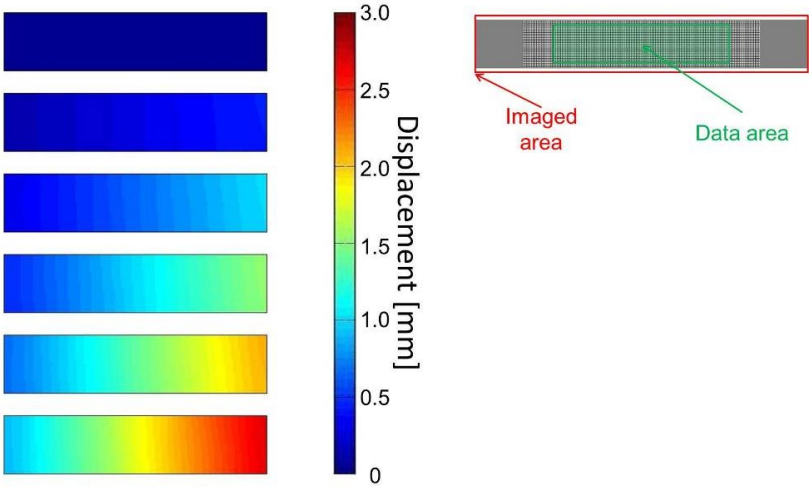

Figure 4.13: Longitudinal displacement maps from GM for 2 m/s actuator displacement speed

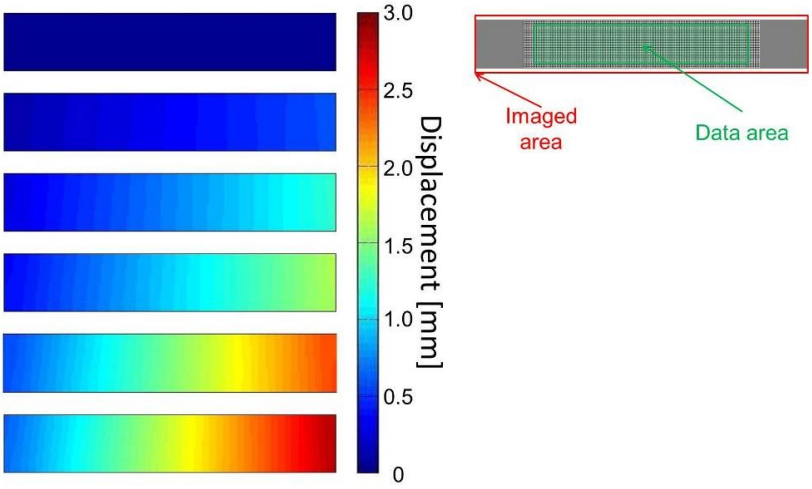

Figure 4.14: Longitudinal displacement maps from GM for 8 m/s actuator displacement speed

From the displacement map it is possible to observe how the specimen is deforming while loaded: this allows to understand if the specimen is loaded correctly. In this particular case the iso-displacement lines, i.e. the area where the displacement are identical, are expectable to be parallel between each other and perpendicular to the specimen edge. This can be observed in Figures 4.11 to 4.14, therefore the specimen is correctly loaded. This allows to conclude that the experimental set-up, and in particular the slack adaptor system, is well suited to perform high speed tensile tests for Young's modulus characterisation.

Strain maps

Representative strain maps, that are directly derived from the displacement with a spatial differentiation, are shown in Figures 4.15 to 4.18 along with the relative position on the stress-strain curve.

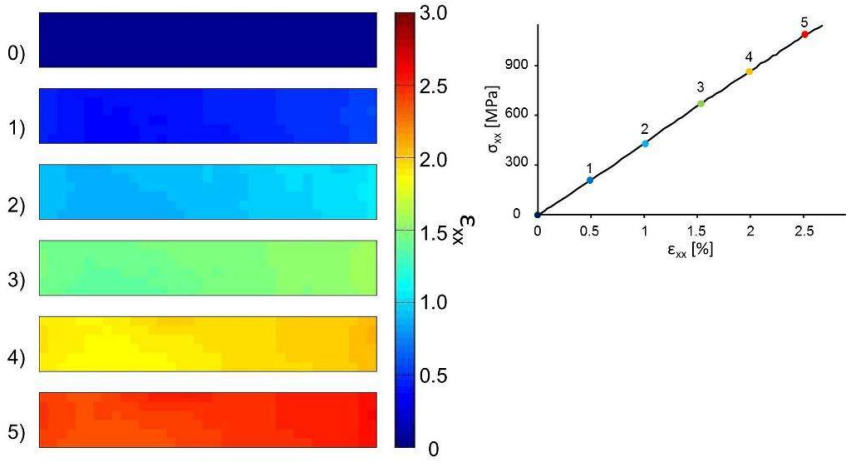

Figure 4.15: Longitudinal strain maps from DIC for 2 m/s actuator displacement speed

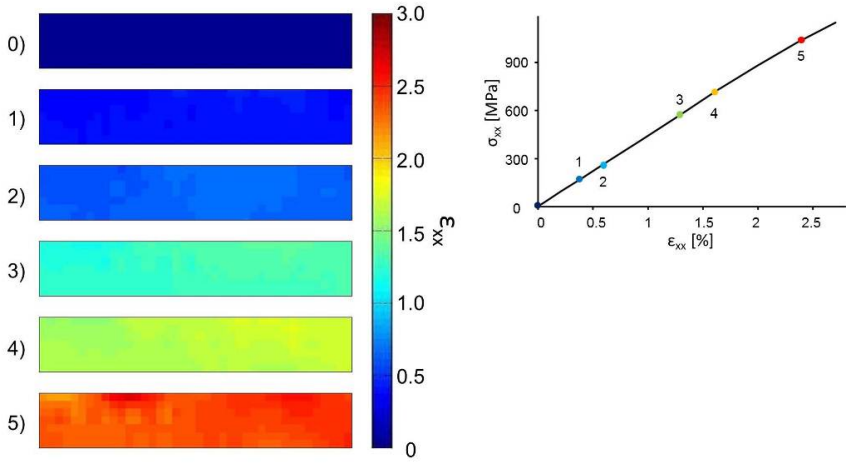

Figure 4.16: Longitudinal strain maps from DIC for 8 m/s actuator displacement speed

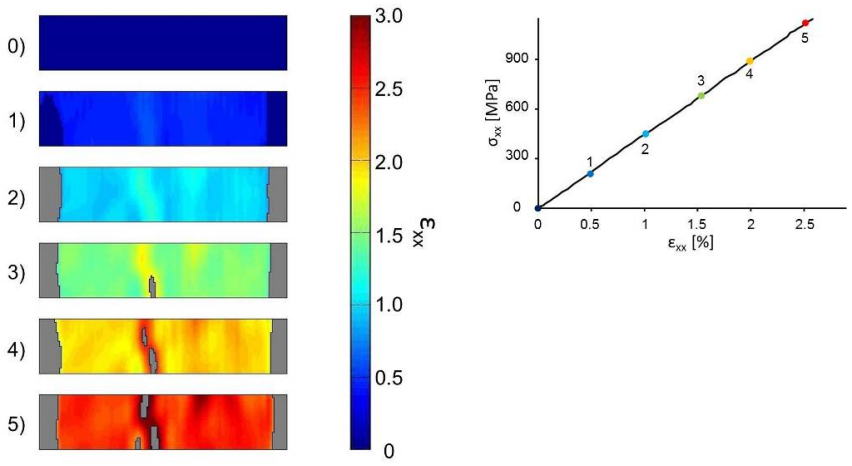

Figure 4.17: Longitudinal strain maps from GM for 2 m/s actuator displacement speed

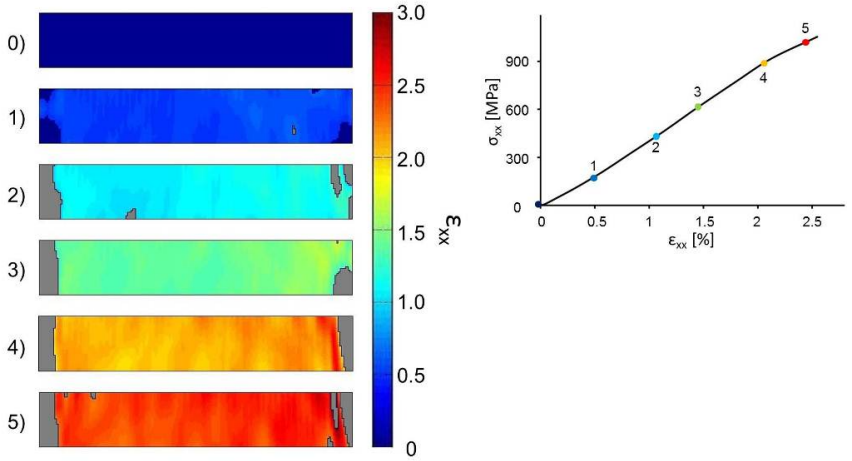

Figure 4.18: Longitudinal strain maps from GM for 8 m/s actuator displacement speed

The grey areas in the maps represents areas where the data are discarded as outliers, in particular because grid defects made impossible to calculate the strain. In the strain maps calculated with the GM the outlier region grows with the strain as the temporal phase unwrapping increases the data nosiness. It can be observed that the strain field is uniform over the specimen surface. This allows to confirm that the averaging of the strain over the whole specimen surface is a suitable procedure to identify the strain values to draw the stress-strain curve. Comparing the maps obtained with DIC and the GM, it is evident that the latter, thanks to its higher spatial resolution, allows to obtain a higher number of data points.

Strain rate maps

The strain rate maps, that are directly derived from the strain with a temporal differentiation, are shown in Figures 4.19 to 4.22 along with the relative position on the strain-strain rate curve.

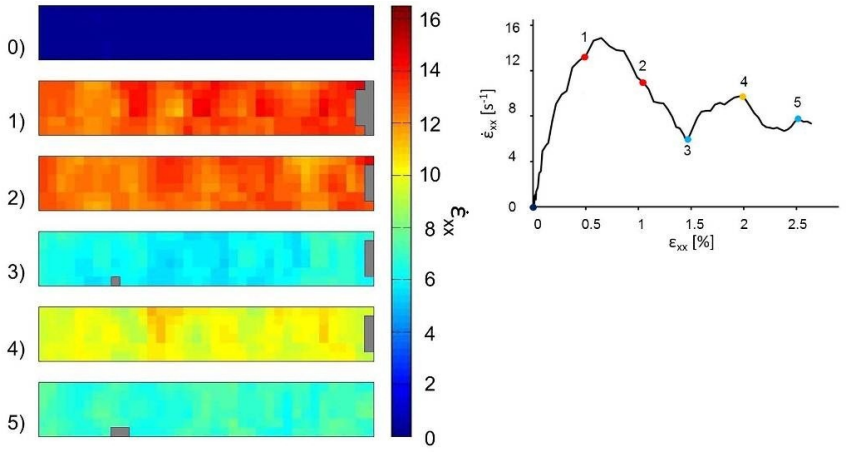

Figure 4.19: Longitudinal strain rate maps from DIC for 2 m/s actuator displacement speed

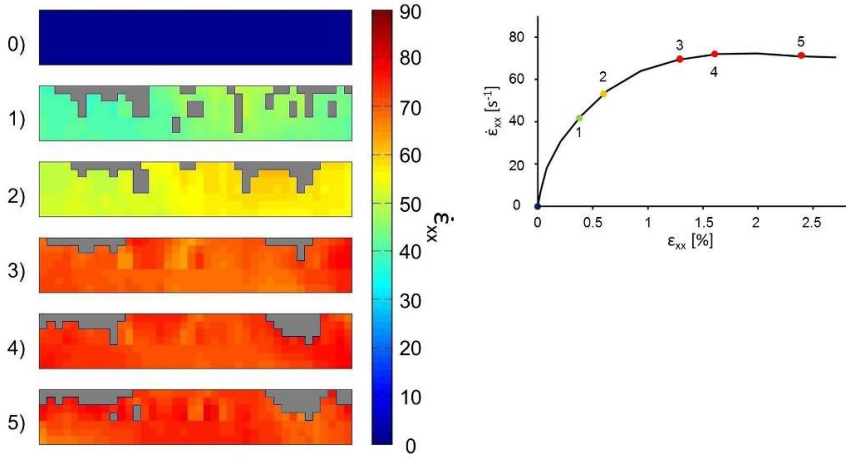

Figure 4.20: Longitudinal strain rate maps from DIC for 8 m/s actuator displacement speed

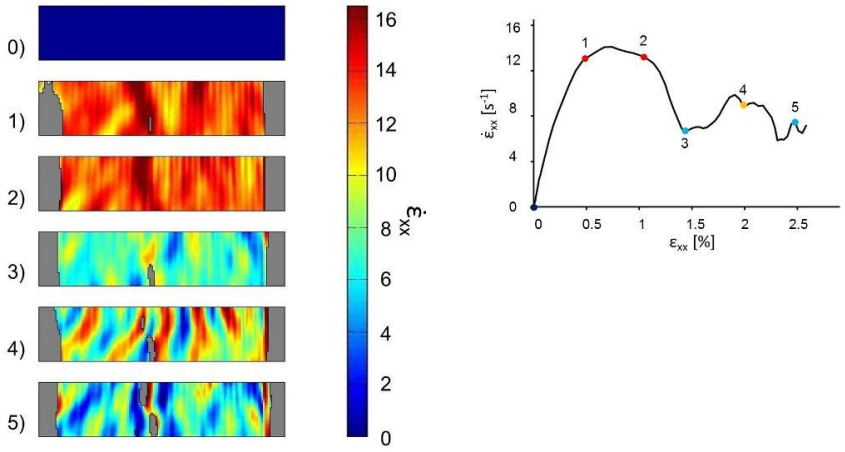

Figure 4.21: Longitudinal strain rate maps from GM for 2 m/s actuator displacement speed

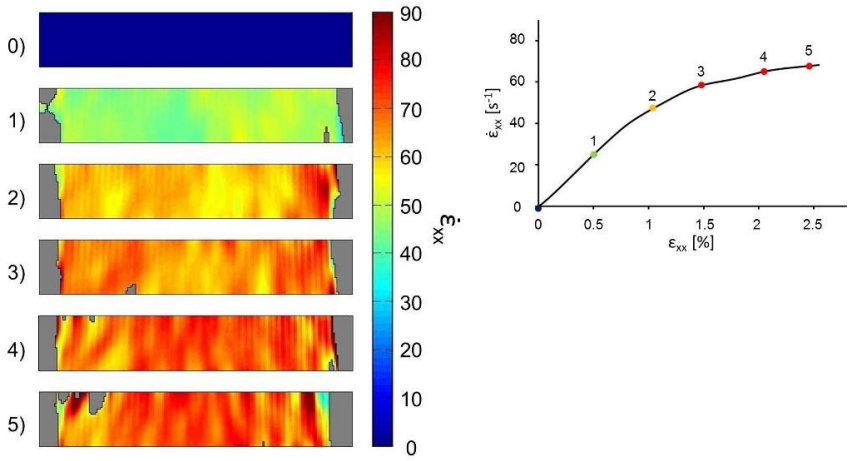

Figure 4.22: Longitudinal strain rate maps from GM for 8 m/s actuator displacement speed

The strain rate maps are strongly affected by the noisiness induced by the temporal differentiation, therefore the general appearance of the map is more noisy and a higher number of outliers is identifiable. High noisiness is particularly evident for Figure 4.21 (GM at 2 m/s actuator displacement speed), this can be explained considering the high spatial resolution of GM and the fact that the strain difference between to consecutive images is minimal. It can be observed that, considering the noisiness introduced by the differentiation, the strain rate field is approximately uniform over the specimen surface. This is another proof of the suitability of the developed experimental technique. However the strain rate is not uniform over the duration time of the experiment. Strain-strain rate curve, calculated from the average over the data area, are shown in Figures 4.23 and 4.24.

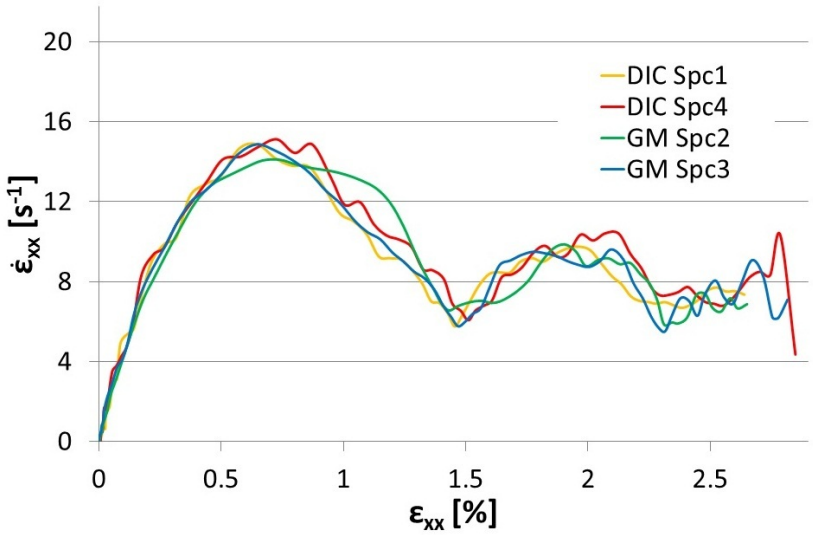

Figure 4.23: Strain rate graph for 2 m/s actuator speed

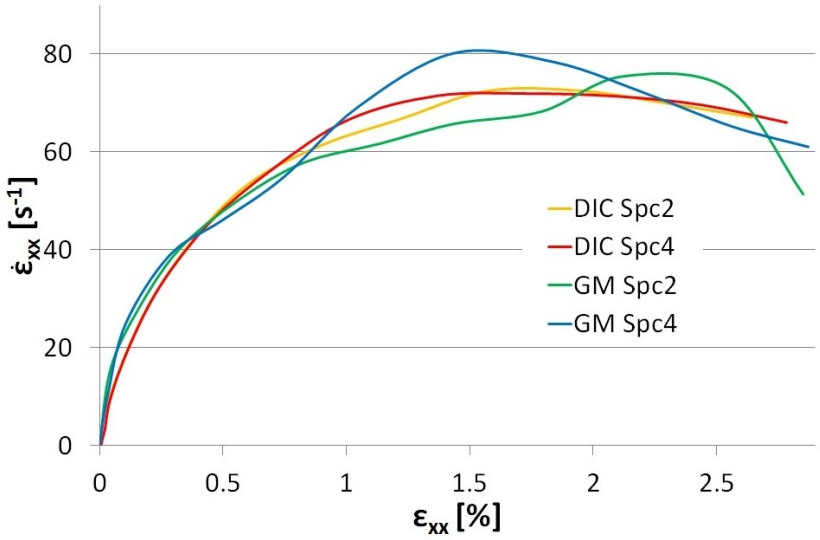

Figure 4.24: Strain rate graph for 8 m/s actuator speed

It has to be remarked that the strain rate curves calculated as average of the strain rate maps and the ones obtained from the temporal differentiation of the average values of the strain maps are superimposable. The non uniformity of the strain rate over the test duration is attributable to the working mechanism of the slack adaptor, described in Section 3.3.2. When the external cylinder, attached to the actuator that is travelling at the desired speed, engages with the inner plunger the latter needs to accelerate. The problem of the inertia of the gripping and loading device, is common in the literature, [50]. Observing Figures 4.23 and 4.24 it appears evident that it is not possible to identify a characteristic strain rate for the tests, it is therefore more appropriate to talk about nominal strain rate that can be calculated

with the formula:

$$\dot{\epsilon} = \frac{V}{L} \tag{4.2}$$

where V is the actuator displacement speed and L is the specimen gauge length. The obtained nominal strain rate values will be used in Section 4.3.2 to model the material behaviour.

4.3 Data analysis and modelling

4.3.1 Statistical analysis

The obtained Young's moduli are presented in Figure 4.11 as function of the nominal strain rate.

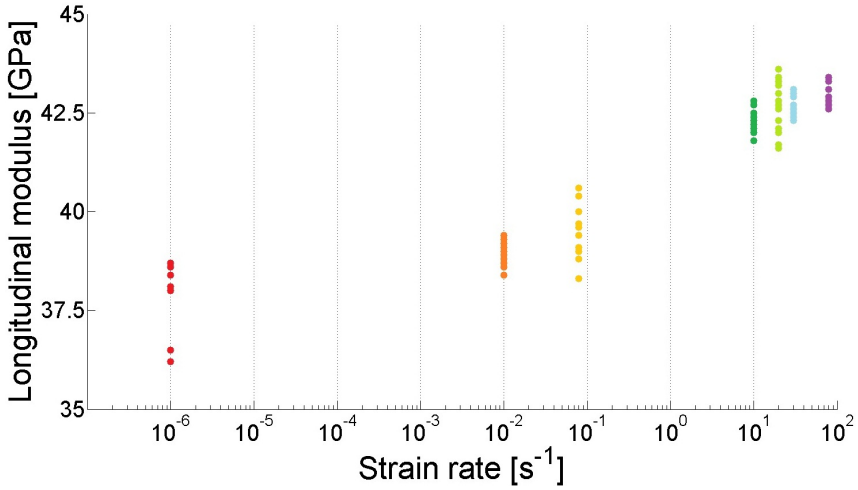

Figure 4.25: Obtained Young's moduli as function of the nominal strain rate

The average of the Young's moduli obtained with the different strain measurement techniques are summarised in Table 4.11 as function of the nominal strain rate.

Table 4.11: Young's moduli in GPa as function of the nominal strain rate

	Nominal strain rate [s^{-1}]						
Measurement Technique	Quasi Static	0.01	0.08	10	20	30	80
2D DIC	38.6	39.2	39.0	42.4	42.6	42.8	43.0
Stereo DIC	-	38.8	-	42.4	-	42.6	-
GM	36.6	38.9	39.7	42.1	42.5	42.5	43.0
Strain Gauge	38.3	39.0	39.6	42.3	42.6	42.6	43.1

Figure 4.25 suggests an increase of the Young's modulus with the strain rate. It is necessary to conduct a study to establish if the difference between the mean values of the Young's moduli calculated at the different strain rates is statistically significant.

This is done using the Kruskal-Wallis test [83], a non-parametric method for testing whether samples originate from the same distribution. Two analysis are performed:

- **Low vs. intermediate strain rate** The data are organised in two set, as shown in Figure 4.26, one for the low strain rate below 10^{-1} s^{-1}, in red in Figure 4.26, and one for intermediate strain between 10^{1} and 10^{2} s^{-1}, in green in Figure 4.26.

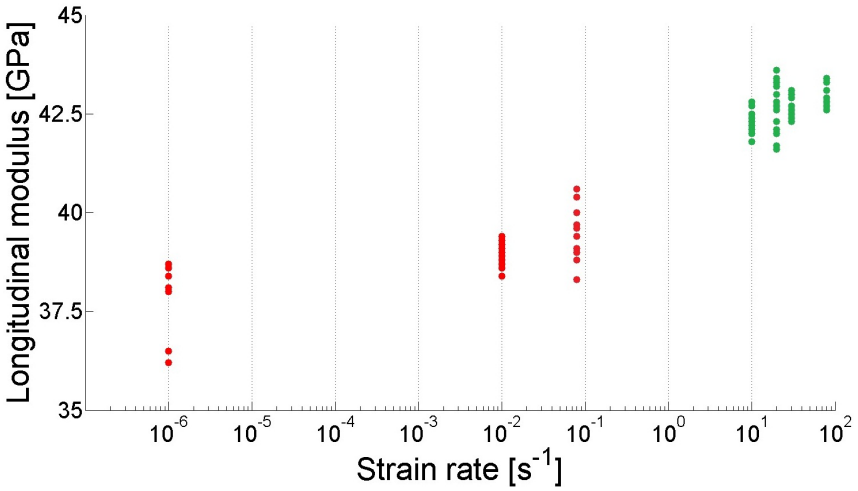

Figure 4.26: Data sets for low vs. intermediate strain rate results statistical analysis

  The analysis allows to conclude that there is a statistically significant increase in E_{11} value between the low and the intermediate strain rate region. This can be attributable to the activation of different deformation mechanism of the polymeric matrix that becomes stiffer when the load rate is increased.

- **In the intermediate strain rate region** The Young's moduli obtained in the intermediate strain rates range, between 10^{1} and 10^{2} s^{-1}, shown in Figure 4.27, are compared between each other to study if the is a statistically significant difference between the results obtained at different nominal strain rate.

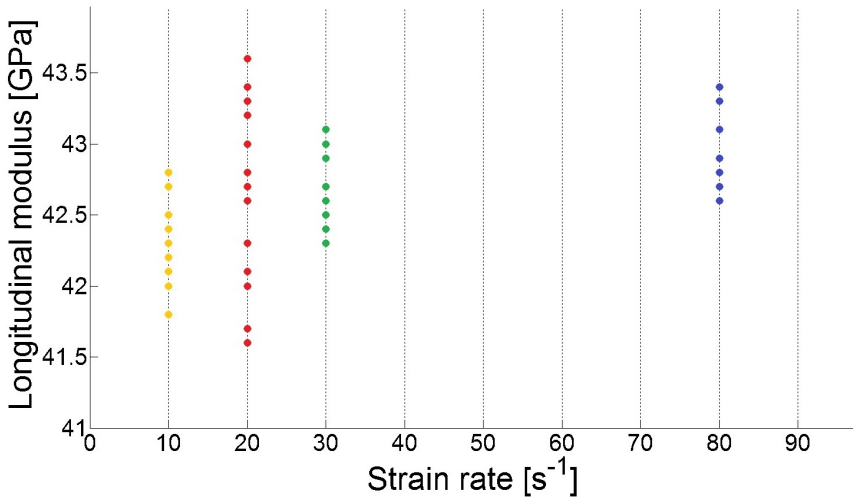

Figure 4.27: Data sets intermediate strain rate results statistical analysis

The results of the analysis are summarised in Table 4.12

Table 4.12: Statistically significant difference between Young's moduli results at intermediate strain rate

Nominal strain rate [s^{-1}]	10	20	30	80
10	-	No	No	Yes
20	No	-	No	Yes
30	No	No	-	No
80	Yes	Yes	No	-

The only set of results that can be considered statistically different from the others is the one relative to the 80 s^{-1}. Therefore, in the strain rate between between 10^1 and 10^2, it is only possible to speculate about an increase of the modulus. This imply that the deformation mechanism is the same in this strain rate region.

4.3.2 Material strain rate dependent tensile behaviour modelling

The results obtained from the tests presented in Section 4.2.3 are used to model the strain rate dependent behaviour of the Young's modulus of the GFRP used here. Accordingly to the results presented in the literature review in Section 3.2, E_{11} slightly increases with the nominal strain rate. The regression function described in Equation 3.1 (Section 3.2) proposed by Shokrieh and Omidi in [48], is used here to describe the strain rate dependence of E_{11}, Equation 4.3:

$$E_{11}\left(\dot{\epsilon}\right) = \alpha + \beta\dot{\epsilon}^{\chi} \tag{4.3}$$

where α, β, and χ are material constants, ϵ is the strain and $\dot{\epsilon}$ is the nominal strain rate calculated with Equation 4.2.
Several computational runs were performed using different sets of initial fitting parameters. The material constants converged to the values summarised in Table 4.13 and shown in Figure 4.28.

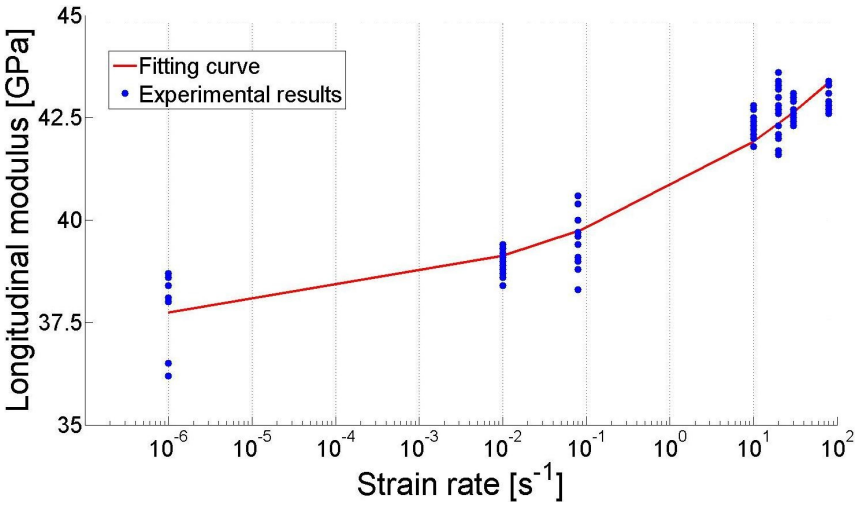

Figure 4.28: Strain rate dependence of Young's modulus

Table 4.13: Material constants for curve fitting describing Young's modulus behaviour

Constant		Value
α	[GPa]	37.1
β	[GPa·s]	3.60
χ		0.126

The coefficient of correlation R^2 is 0.986.
The shape of the fitting curve and the obtained material constants are in agreement with the ones obtained by Shokrieh and Omidi in [48] and [51]: the constant α is close to the quasi-static value of Young's modulus, while β and χ are representative of its strain rate dependence. In particular, β defines the rate of growth of the considered properties, while χ represents the curvature of the regression function.

4.4 Summary

The experimental methodology developed in this research was successfully applied to characterise the behaviour of GFRP unidirectional laminate subjected to deformation at different strain rates. This methodology allows to obtain repeatable and reproducible data.

The optical techniques results have been validated with strain gauge measurements. The deformation and strain resolution and the spatial resolution of the two methods have been compared: at the same resolution the GM offers a higher spatial resolution and therefore a higher number of data point to characterise the material behaviour. It must be anyway remarked that the specimen preparation and the experiment set-up time required to perform the GM is significantly higher than the one required for DIC. Furthermore the grid deposition process is laborious and quite often leads to unsatisfactory results. It can be concluded that, even if on one side the GM is a good optical full-field strain measurement technique, thanks to its high spatial resolution, it can hardly be seen as an efficient technique for the kind of material characterisation tests used in this research. The benefits of the full-field optical techniques were demonstrated showing the information that can be retrieved and how can be applied in the data interpretation. Moreover it can be foreseen the application of the developed experimental methodology to specimen that allow to obtain a non uniform stress-strain state, such as Brazilian disk or T-shaped specimen, and therefore to retrieve more than one material property with a single test. This will also make the GM a useful full-field strain measurement techniques, thanks to the higher spatial resolution achievable.

Finally the obtained results were fitted with a regression function that was proven to be suitable to describe the strain rate dependence of the longitudinal tensile modulus of the material.

5 Strain rate dependence identification of Carbon Fibre Reinforced Plastics stiffness

5.1 Introduction

An experimental methodology has been devised and applied to determine the tensile longitudinal modulus of GFRP material in the previous chapter. In this chapter a methodology for the full study of the strain rate dependent constitutive behaviour of FRP material is devised. The methodology described so far can be used to identify E_{11} and E_{22}. The selection of testing procedure suitable to identify G_{12} applicable to the available resources and the developed experimental methodology is more challenging.

Several techniques are available for the characterisation of the intralaminar shear behaviour of unidirectional fibre composites. The three point bending test [84] addresses mainly the identification of the inter-laminar shear strength and causes a non uniform shear stress distribution through the specimen thickness. Other standardised methodology are the rail shear test [85], and the V-notched specimen rail shear test [86]. In this case the testing rig used to perform the test causes a premature failure of the specimen, promoted by the presence of holes in the test plate. The Iosipescu double V-notched beam test [87] can also be used to identify both the shear stress/strain response and the ultimate strength and strain. This methodology requires a complex fixture to correctly load the specimen. Tensile tests on $\pm 45^{\circ}$ specimen [88] can also be used to identify the in-plane shear modulus and the ultimate stress and strain of the laminate. However these kind of tests leads to a complex fracture that does not allow the identification of the ply failure point. Another methodology is the thin tube subject to torsion, [89] and [90]. This methodology requires an expensive and time consuming specimen preparation that, in general, is not representative of the manufactured material. Furthermore there are difficulties in the correct application of the load and, generally, curved surfaces are difficult to image correctly for full-field optical strain measurement purposes. Ultimately all the

standardised methods are hardly usable with Instron VHS. For example rail shear tests and Iosipescu tests require complex fixtures, difficult to be integrated with the slack adaptor. The off-axis tensile test technique [91], that was developed in the late seventies, is deemed to be suitable to identify the in-plane shear properties of composite material with the aid of full-field optical strain measurement techniques and with the available testing machines. The specimen geometry is the same as the one used to identify E_{11} and E_{22}, allowing the use of the same fixture for all the characterisation tests. The use of oblique end-tab mitigates the effects of the stress concentration in proximity of the end-tabs, as discussed below. Furthermore the specimen dimensions are suitable to perform high speed imaging and obtain a suitable number of data points as it is similar to what is developed in Chapter 4.

The methodology used here to achieve a precise material characterisation from tensile tests is as follows:

1. Preliminary tests:
    - Tensile test at 0° fibre orientation to identify E_{11} and ν_{12};
    - Tensile test at 90° fibre orientation to identify E_{22};
    - Off-axis tensile test with square end-tabs to estimate G_{12}. Pierron *et al.* [92] recommended a procedure consisting of preliminary test using straight tabs to estimate the shear modulus before using oblique tabs.
2. Optimised off-axis tensile test with oblique end-tabs to identify G_{12}. The preliminary results obtained from the previous step are used to define the end-tab and the optimal off-axis angle.

This procedure can be applied for FRP materials characterisation at different strain-rates.

The theoretical background of the off-axis tensile tests for FRP material characterisation and the relevant literature are presented in Section 5.2. Particularly in Section 5.2.1 the use of oblique end-tab to mitigate the effects of the stress concentration in proximity of the end-tabs is discussed.

In Section 5.3 a preliminary study of the specimen design is presented with the aims of:

- Defining the preliminary off-axis angle for FRP of various type.
- Defining the impact of an incorrect estimation of the oblique end-tab angle on the G_{12} identification.

- Defining the impact of an inaccurate off-axis specimen manufacturing on the G_{12} identification.

In Section 5.4 the values of E_{11}, E_{22} and G_{12} of a CFRP material are reported for a strain rate range from quasi static to about 10^2 s^{-1}.

These values are then used in Section 5.5 to inform a model of the strain rate dependent behaviour of the considered CFRP material.

5.2 Theoretical background

The off-axis test was first introduced by Chamis and Sinclair, [91], who observed that a bi-axial state of stress, consisting of the combination of a tensile, transverse and shear stress state, is present in fibrous composite materials when an off-axis unidirectional specimen is subject to a uni-axial load, Figure 5.1.

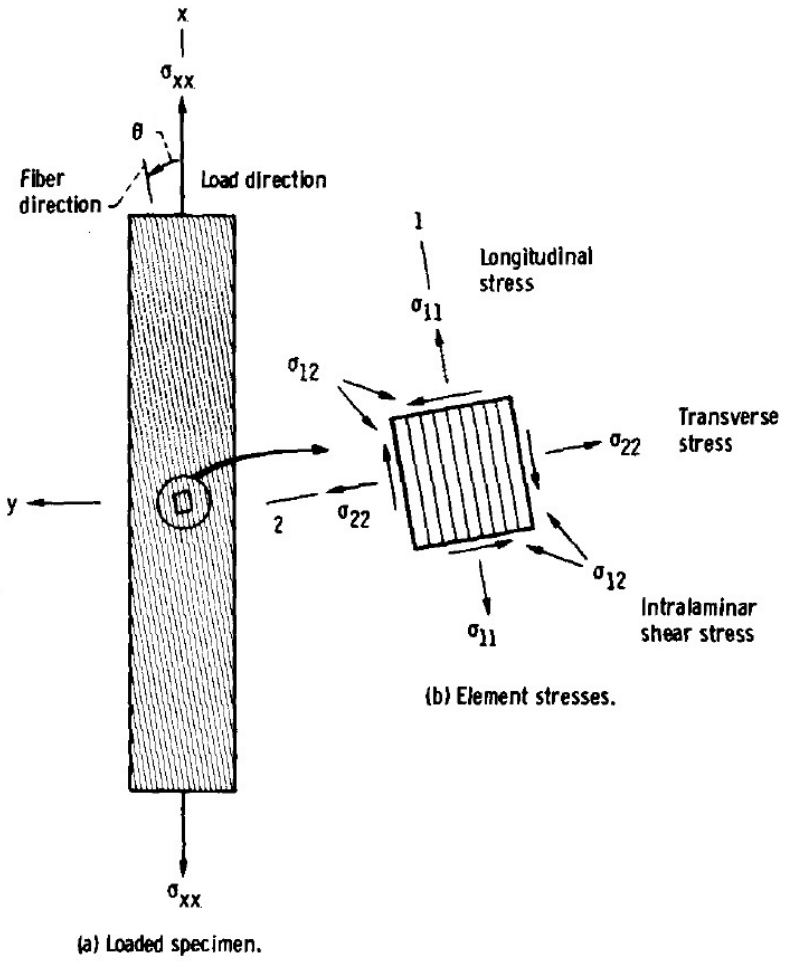

Figure 5.1: Off-axis tensile test schematic and representation of the biaxial stress state from [93]

The idea is to orientate the off-axis angle in such a way that the shear stress is the only one close to its critical value. From force equilibrium considerations the stresses in the ply, or material, orientation (σ_{11}, σ_{22} and σ_{12}) are identified as function of the off-axis angle ϑ and applied stress σ_{xx}:

$$\begin{aligned} \sigma_{11} &= \sigma_{xx} \cos^2 \vartheta \\ \sigma_{22} &= \sigma_{xx} \sin^2 \vartheta \\ \sigma_{12} &= \frac{1}{2} \sigma_{xx} \sin 2\vartheta \end{aligned} \tag{5.1}$$

The authors assessed how sensitive the material axes strains (ϵ_{11}, ϵ_{22} and ϵ_{12}) and stresses (σ_{11}, σ_{22} and σ_{12}) are to small errors in the load-orientation angle by plotting these, normalised by ϵ_{xx} and σ_{xx} against the orientation angle, as shown in Figures 5.2 and 5.3:

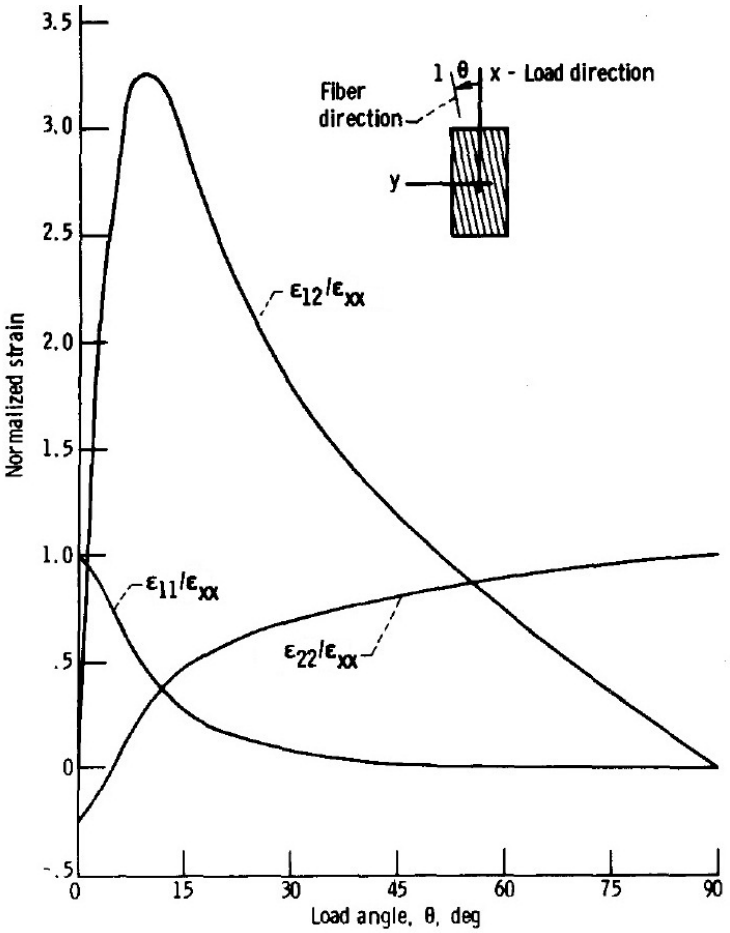

Figure 5.2: Variation of the strain in the material axes against the load direction from [93]

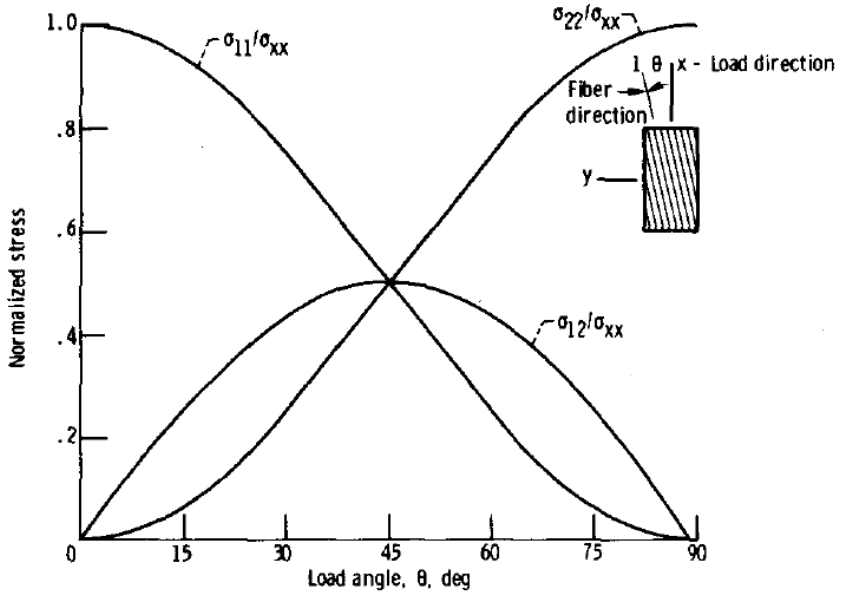

Figure 5.3: Variation of the stress in the material axes against the load direction from [93]

The authors then conducted a series of experiments on Mod-I/epoxy, T-300/epoxy, and S-glass/epoxy specimens instrumented with a strain gauge rosette to devise a procedure for generating the intralaminar shear stress-strain curve, that can be generalised as follows:

1. Calculate the strains in the specimen axes, ϵ_{xx}, ϵ_{yy} and γ_{xy}, from the strains given by a strain gauge rosette. The authors describe the use of a 60° delta rosette or a 0-45-90° rosette.

2. Calculate the intralaminar shear strain in the material axes by rotating the strains obtained in the specimen axes;

3. Calculate the ply intralaminar shear stress in the material axes, σ_{12}, using Equation 5.1;

4. Plot σ_{12} against γ_{12}.

The initial shear modulus is determined from the slope of the initial tangent to the plotted stress-strain curve. The tangent shear modulus at any other point is determined from the slope of the tangent to the curve at that point. The material intralaminar shear strength and failure strain are the values of σ_{12} and γ_{12} at fracture. The authors concluded that the 10° off-axis tensile test should be considered as a possible standard test for characterizing the intralaminar shear properties of unidirectional fibre composites. Compared to other methodologies, the off-axis tensile test offers several advantages:

- Use of a familiar tensile test procedure and equipment;

- Use of thin, narrow laminate specimens which save considerable material compared to thin tubes in torsion or other standardised methodologies;
- Specimens can be obtained from the same laminate as test specimens for longitudinal and transverse properties characterisation;
- Specimens are free of lamination residual stresses in contrast to the $\pm 45^{\circ}$ specimen.

The conclusions made by Chamis and Sinclair that have a high impact on the research work presented here are:

- Specimens are suitable for dynamic and impact loading characterization;
- The test yields the following off-axis properties:
  - Shear modulus;
  - Shear strength;
  - Coupling between extensional and shear deformations.
- The specimen can be successfully used for high strain rate intralaminar shear characterization;

The disadvantages reported by the authors in [91] which can now be easily solved with full-field optical techniques are:

- Need to measure the three strain components per data point;
- High precision required in the alignment of the strain gage rosette on the specimen.

5.2.1 Oblique end-tabs

The extension-shear coupling existing in anisotropic materials produces the deformed shape shown in Figure 5.4 a), which causes rotations and transverse strains at the extremities of the specimen. The deformed shape in a test with regular gripping system would have the form represented in Figure 5.4 b).

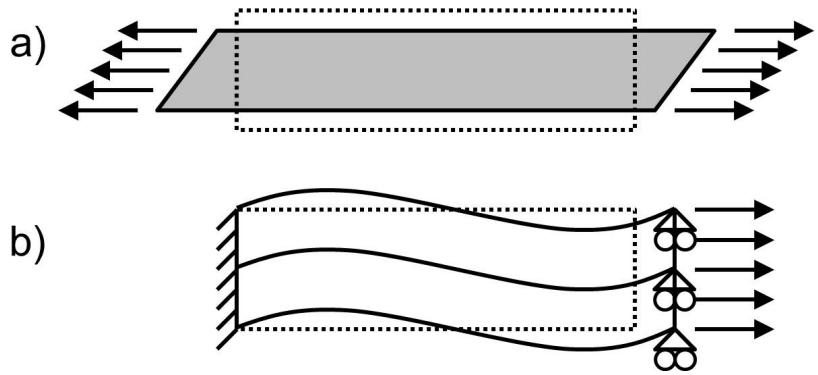

Figure 5.4: Schematic representation of off-axis specimen deformed shape as in [94]:
a) Ideal
b) Clamped ends

The main problem related to the use of off-axis tensile test on uni-directional composite materials to characterise the shear properties with off axis specimens was identified by Pagano and Halpin [95], and Rizzo [96] in the constraints imposed by the gripping system. Pagano and Halpin attributed the main cause of the non ideal deformed shape to the restriction of the lateral strain, while Rizzo attributed it to the restriction of the rotations at the extremities of the specimen. The solutions proposed in the literature can be divided in two radically different approaches, as done by Marín *et al.* [94]:

- The use of correction factors during the data post processing.
- The use of manufacturing and testing expedients to mitigate the stress concentration while performing the test.

Pindera and Herakovich [97] obtained an analytical formula to correct the apparent shear modulus through a tensile test performed with a gripping system that allowed the rotation of the specimen ends. Marín *et al.*, [94] and [98], presented a detailed review of the most significant works on the off-axis tests assessing the obtained results and devised new approach together with numerical and experimental studies. Also Mujika [99] proposed two analytical approaches to correct the experimental results. Even if these methodologies are well proved and suitable for the shear characterisation it is believed that simpler approaches are those that allow a uniform strain field in the gauge area to be obtained through a conveniently designed specimen.

Various approaches have been suggested for the test set-up or for the specimen preparation in order to achieve a uniform stress-strain field in the gauge area. The simplest, but impractical especially if applied to full-field stain measurement techniques, is to use high aspect ratio specimens with very long and tapered end-tabs,

[100] and [101]. It is worth remembering once again the work of Pindera and Herakovich [97] who suggested the use of rotating grips coupled with correction factors. Chang *et al.* [102] proposed the use of pinned-end fixtures, a solution also used by Xiao *et al.*, [103], to devise an integrated method suitable for off-axis tension and compression testing of unidirectional composites for intra-laminar shear characterization. Another proposed methodology aimed at the achievement of a uniform stress-strain state in the gauge area can be found in the work by Sun and Berreth [104] who used fibreglass knit and silicon rubber end-tabs to allow the shear deformation of the clamped section of the specimen. The most appealing solution is the oblique-shaped end-tab that ensures a uniform state of strain and stress in the gauge length of off-axis specimens, proposed by Sun and Chung, [105].

The idea of Sun and Chung is to orientate the edge of rigid end-tabs in such a way that it is parallel to the iso-displacement lines along which the off-axis deforms when subject to a uni-axial load. The end-tab angle can be easily defined. The strain status (ϵ_{xx} ϵ_{yy} γ_{xy}) of an off-axis uni-directional composite specimen under uni-axial stress is described by:

$$\begin{aligned} \epsilon_{xx} &= S_{xx}\sigma_{xx} \\ \epsilon_{yy} &= S_{yx}\sigma_{xx} \\ \gamma_{xy} &= S_{sx}\sigma_{xx} \end{aligned} \tag{5.2}$$

where S_{ab} are the compliance coefficients with respect to the $x-y$ coordinate system defined in Figure 5.1. It is possible to express the displacement as the spatial integration of strain, considering the constant strain field expressed in Equation 5.2, as:

$$\begin{aligned} u &= S_{xx}\sigma_{xx}x + C_1 y + C_3 \\ v &= S_{yx}\sigma_{xx}y + C_2 x + C_4 \end{aligned} \tag{5.3}$$

Where u and v are the longitudinal and the transverse displacement respectively and C_n are arbitrary constants. Considering that the specimen is not undergoing any rigid body translation C_3 and C_4 are zero. While imposing the condition that the transverse edge of the specimen remains parallel to itself it can be written that:

$$\frac{\partial v}{\partial x} = C_2 = 0 \tag{5.4}$$

The remaining constant C_1 can be determined by the known shear strain as:

$$\gamma_{xy} = \frac{\partial v}{\partial x} + \frac{\partial u}{\partial y} = C_1 = S_{sx}\sigma_{xx} \tag{5.5}$$

The displacement field of Equation 5.3 can be expressed as:

$$\begin{aligned} u &= S_{xx}\sigma_{xx}x + S_{sx}\sigma_{xx}y \\ v &= S_{yx}\sigma_{xx}y \end{aligned} \tag{5.6}$$

Therefore the longitudinal component of the displacement, u, can be maintained uniformly along a straight line that satisfies the equation:

$$u_0 = (S_{xx}x + S_{sx}y)\,\sigma_{xx} \tag{5.7}$$

The angle φ between the iso-displacement line and the specimen longitudinal edge therefore is:

$$\cot\varphi = \frac{S_{sx}}{S_{xx}} \tag{5.8}$$

that represents the angle of the oblique end-tabs that ensures a uniform longitudinal displacement that causes a uniform stress state in the specimen.

The finite element analysis and experiments conduct by Sun and Chung in [105] on carbon/epoxy specimens proved that the oblique end-tab is more suitable than the conventional rectangular tab for uni-axial off-axis testing. Pierron and Vautrin [106] showed that oblique tabs significantly increase the failure shear stress localising the failure in the gauge section through finite element modelling and experiments with carbon/epoxy specimens. This work is further developed by Pierron *et al.* [92] who showed with full-field optical techniques (in this case the GM) that the use of oblique end-tabs crates a homogeneous strain field in the gauge area. Furthermore, with numerical sensitivity study, it was demonstrated that the oblique angle is not very sensitive to the elastic moduli values. The value of oblique end-tab for uni-directional composite material shear behaviour characterisation was also demonstrated by Kawai *et al.* [107], who concluded that the oblique end-tabs significantly reduce the end-constraint effect and enable the achievement of a homogeneous strain field in specimens of aspect ratio as low as 4 as well as in the non-linear and non-elastic response region of the material. In the field of high strain rate material behaviour characterisation off-axis tensile test performed on specimens with oblique end-tabs were carried on by Taniguchi *et al.* on a tension-type SHB that defined the moduli and the strength of CFRP using a strain gauge rosette, [59] and [108].

5.2.2 Summary

The uni-axial off-axis tensile test methodology proposed by Chamis and Sinclair [91] in combination with the use of oblique end-tabs, as suggested by Sun and Chung

[105], is suitable to characterise the shear behaviour of composite materials. This technique can be easily integrated with the experimental methodology developed so far. Moreover the type of specimens used for uni-axial off-axis tensile tests are suitable for the application of full-field strain measurement techniques.

5.3 Specimen design

It is important to understand how the definition of the off-axis angle and end-tab angle affects the correct implementation of the off-axis tensile test. At this stage four materials are taken into account: two CFRP and two GFRP. The material properties are listed in Table 5.1.

Table 5.1: Engineering constants for the analysed materials, from [109]

	E_{11} [GPa]	E_{22} [GPa]	G_{12} [GPa]	ν_{12}
CFRP1	137.9	9.0	7.1	0.30
CFRP2	131.0	10.3	6.9	0.22
GFRP1	53.8	17.9	9.0	0.25
GFRP2	38.6	8.3	4.1	0.26

The reference coordinate systems used in this chapter are shown in Figure 5.5, where ϑ is the off-axis angle and φ the end-tab angle.

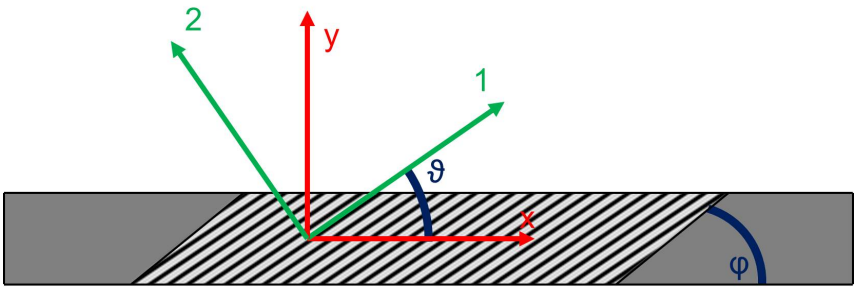

Figure 5.5: Reference coordinate systems: specimen and material axes

5.3.1 Definition of the optimal off-axis angle

As explained in Section 5.2, the off-axis angle for which the ratio between the material axes shear stain, ϵ_{12}, and the global tensile strain, ϵ_{xx}, is maximum, i.e. the optimal off-axis angle for G_{12} identification tests, depends on the material properties, [91]. Figures 5.6 and 5.7 plot the strains in the material axes normalised by the tensile strain in the specimen axes against the off-axis angle for two of the materials of Table 5.1.

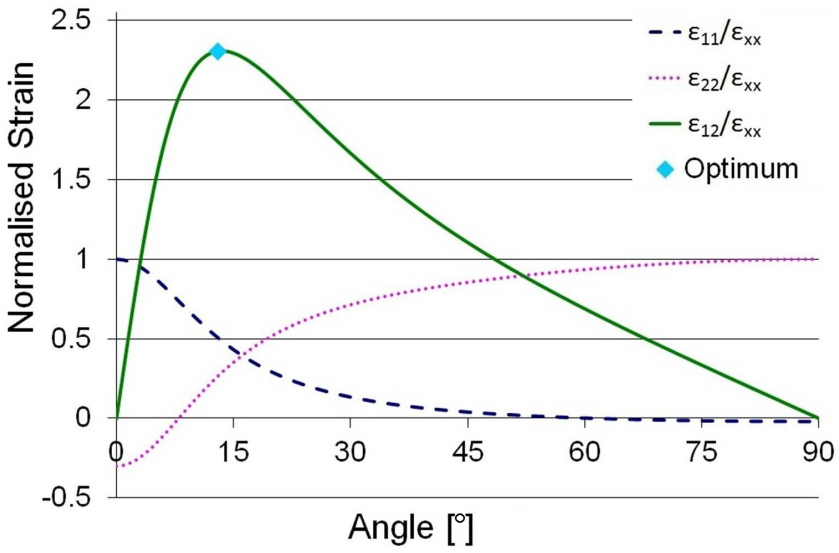

Figure 5.6: Variation of the normalised strains against the off-axis angle for the CFRP1 material

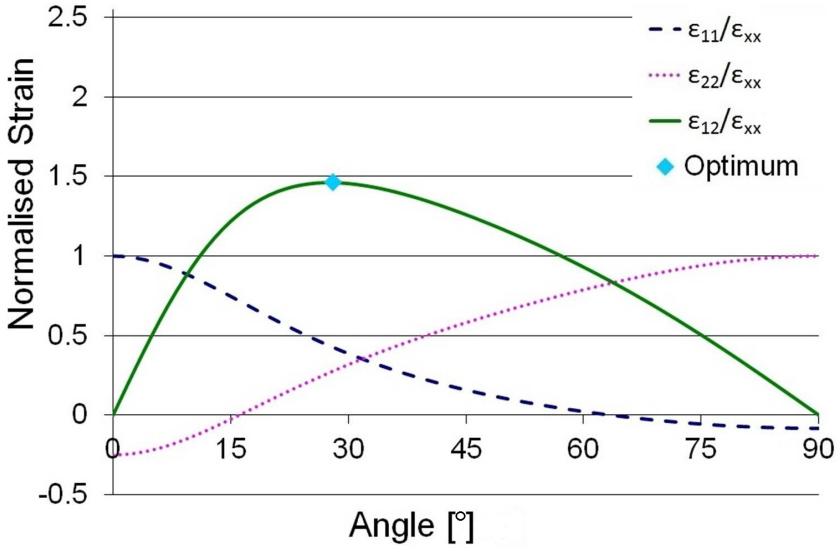

Figure 5.7: Variation of the normalised strains against the off-axis angle for GFRP1 material

The optimal off-axis angle values are reported in Table 5.2 along with E_{11}/E_{22} and E_{11}/G_{12} ratios.

Table 5.2: Material properties ratios and consequent optimal off-axis angle

	E_{11}/E_{22} ratio	E_{11}/G_{12} ratio	Optimal angle [°]
CFRP1	15.3	19.4	13
CFRP2	12.7	19.0	14
GFRP1	3.0	6.0	28
GFRP2	4.7	9.4	21

Observing Figures 5.6 and 5.7 it appears evident that the material shear strain is dominant in a region approximatively from -5° to +15° around the optimal off-axis angle. Testing around the optimal off-axis angle has particular meaning when measuring the strains with optical techniques, as this maximises the material shear strain value that will be beneficial when defining the σ_{12}-γ_{12} curves. The optimal off-axis angle, i.e. the off-axis orientation angle at which the normalised shear strain is maximum, is influenced by E_{11}/E_{22} and E_{11}/G_{12} ratios. A high E_{11}/E_{22} ratio has the effect of reducing the optimal angle, while high values of shear modulus G_{12} have the effect of increasing it. Furthermore low E_{11}/E_{22} and E_{11}/G_{12} ratios have the effect of reducing the normalised strain. These observations are important for the off-axis angle identification for the preliminary test with square end-tabs: values of 13° for CFRP and 24° for GFRP should be used. If this characterisation methodology is to be applied to composite material with lower E_{11}/E_{22} and E_{11}/G_{12} ratios, e.g. natural fibre composite, higher off-axis angle, around 25-30° , might be needed for the preliminary off-axis test. Moreover this study justifies the need to run a second off-axis tensile test: not only the accuracy of G_{12} and shear failure load is increased by the use of oblique end-tabs but also higher strains can be achieved and a better stress-strain curve can be drawn to identify initial and tangent shear moduli and to describe the non-linear shear behaviour at high strain.

Using the procedure described by Sun and Chung [105] and summarised in Section 5.2, it is also possible to calculate the oblique end-tab angle that allows to obtain a state of nearly uniform stress in the gauge area. The results are summarised in Table 5.3.

Table 5.3: Material properties ratios and consequent optimal off-axis angle

	Optimal angle ϑ [°]	End-tab angle φ [°]
CFRP1	13	27
CFRP2	14	28
GFRP1	28	55
GFRP2	21	42

These values will be used in Section 5.3.2 to evaluate the effect of inaccuracies in the preliminary tests on the evaluation of the end-tab angle and on the identification of G_{12}.

5.3.2 Effects of errors in the preliminary tests on the optimal off-axis and end-tab angle

The importance of the preliminary tests to define the optimal off-axis and end-tab angle has been explained previously. It must be taken into account that the three moduli and Poisson's ratio evaluated with the preliminary tests can be inaccurate. It is therefore necessary to understand how these inaccuracies affect the definition of the test parameters and the final results. The testing parameters that are affected by an inaccurate material characterisation in the preliminary phase are the off-axis and the oblique end-tab angle. Two of the four materials presented in Table 5.1, CFRP1 and GFRP1, are taken into consideration.

Effects of errors in the preliminary tests on the optimal off-axis angle

The relative error on the off-axis angle definition as function of the relative error, i.e. $\frac{Modulus_{Measured}}{Modulus_{Real}}$, in E_{11}, E_{22} and G_{12} are shown in Figures 5.8 and 5.9.

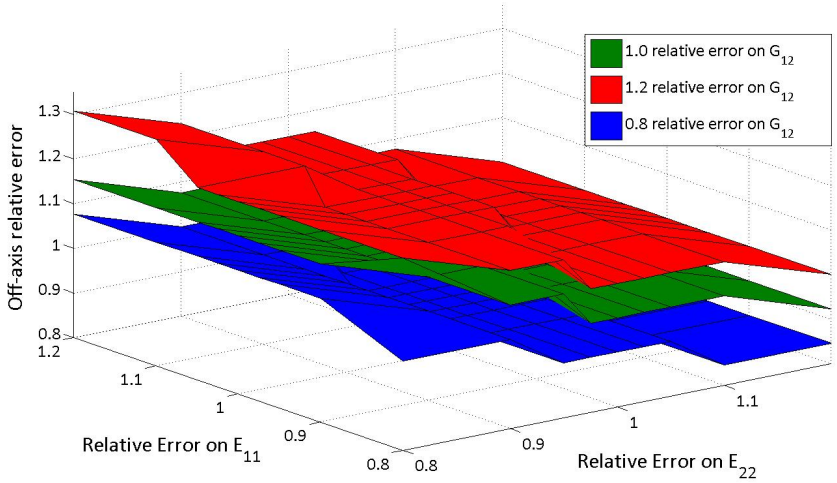

Figure 5.8: Off-axis angle error as function of the relative error in the preliminary moduli identification experiments for the CFRP1 material

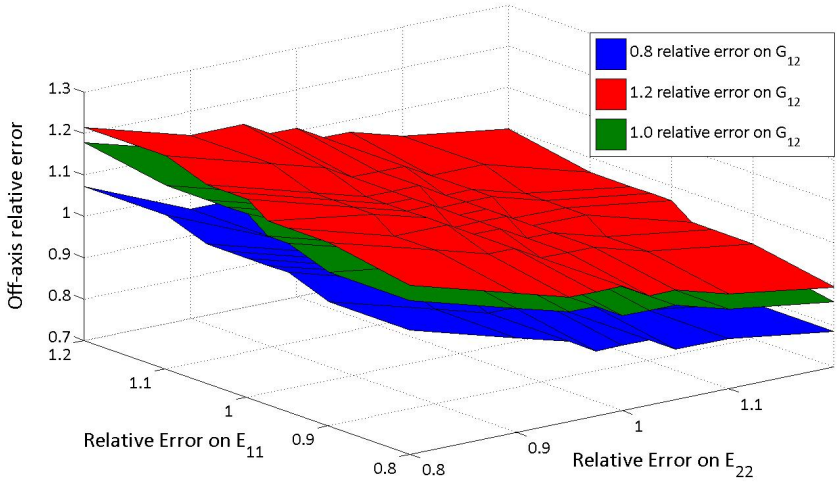

Figure 5.9: Off-axis angle error as function of the relative error in the preliminary moduli identification experiments for the GFRP1 material

For the CFRP1 material, i.e. high E_{11}/E_{22} and E_{11}/G_{12} ratios, errors of the order of $\pm 20\%$ in the moduli estimation leads to errors of the order of -15% and +31% in the optimal off-axis angle. While for the GFRP1 material, i.e. lower E_{11}/E_{22} and E_{11}/G_{12} ratios, lead to errors of the order of $\pm 21\%$. It can be concluded that inaccuracies in the definition of the optimal off-axis angle does not affect the shear moduli identification test that would still be performed at an off-axis angle for which the $\epsilon_{12}/\epsilon_{xx}$ is still around its maximum. The repercussions of errors in the preliminary tests are more severe in the oblique end-tab angle identification.

Effects of errors in the preliminary tests on the end-tab angle

The effect of an inaccurate preliminary assessment of the material moduli on the oblique end-tab angle is shown in Figures 5.10 and 5.11 as difference between the end-tab angle evaluated with the wrong moduli values and the correct at the assumed off-axis angle.

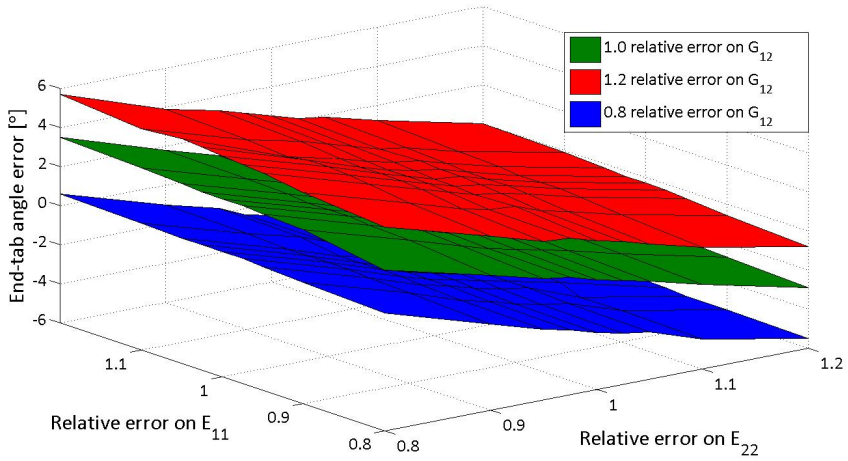

Figure 5.10: End-tab angle error as function of the relative error in the preliminary moduli identification experiments for the CFRP1 material

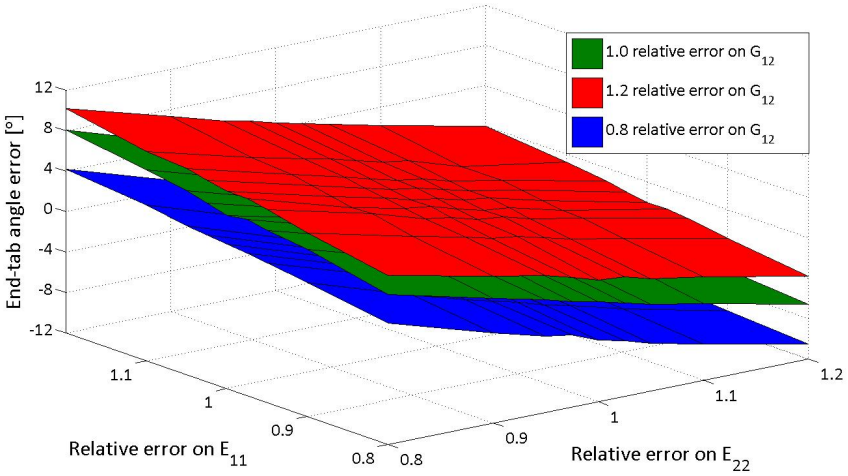

Figure 5.11: End-tab angle error as function of the relative error in the preliminary moduli identification experiments for the GFRP1 material

Errors of the order of ±20% in the moduli estimation leads to an error of the order of ±20% in the oblique end-tab angle for both materials. These correspond to 5.5° for the CFRP1 material and 10° for GFRP1. A discussion about the effects of a wrong end-tab angle on the G_{12} modulus identification is provided below, and shown in Figure 5.17. In [92], Pierron *et al.* observed that in a CFRP specimen for modulus measurement purposes an error up to 3° in the end-tab can be considered acceptable. According to the authors an error up to 7° still generates a stress state that can be assumed to be homogeneous at the centre of the specimen even if it leads to significant stress concentrations near the end-tabs.

Effects of errors in the specimen manufacturing on the end-tab angle

Even if the optimal off-axis angle and the corresponding end-tab angle are correctly defined, they might not be matched during the specimen manufacturing process. Particularly for this research, where the specimens are hand cut with a tile cutter equipped with a rotating diamond blade, higher than normal tolerances in the off-axis and end-tab angle are to be expected. An error in the off-axis angle, caused by cutting tolerance, leads to the use of an incorrect end-tab angle. The error on the end-tab angle, φ_{Err}, originating from cutting the specimens at a wrong off-axis angle, plotted in Figure 5.12, is calculated as:

$$\varphi_{Err} = \varphi_{Tol} - \varphi_{Nom} \tag{5.9}$$

where φ_{Tol} is the end-tab angle required by the off-axis angle at which the specimen is cut, and φ_{Nom} is the end-tab angle required by the nominal off-axis angle.

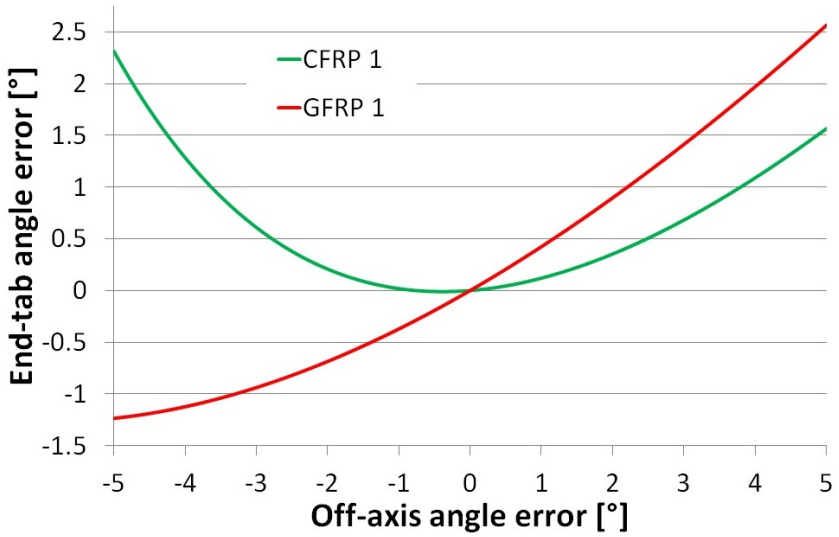

Figure 5.12: Error in the end-tab angle as function of an incorrect off-axis angle

It is fair to assume an error on the off-axis angle of maximum $\pm 2°$, this will cause an error in the end-tab not higher than $1°$. Ultimately, manufacturing errors on the off-axis and end-tab angle cause on the G_{12} modulus evaluation the same effects as an incorrect end-tab angle definition. These effects are discussed below.

Effects of errors in the end-tab angle on G_{12} identification

A finite element model is used to assess how an error in the oblique end-tab angle influences the uniformity of the strain field generated in the off-axis tensile test with oblique end-tab.

A model of the off-axis specimen is created using Ansys 14.0. The Shell 181 element is used to model the laminated composite material. This element is a four-node element with six degrees of freedom at each node and has the capability of modelling laminar composites. Furthermore Shell 181 allows the definition of the orientation angle of the orthotropic material, used to model CFRP1 and GFRP1, with respect to the model coordinate system. The optimised mesh size is defined through an optimisation process and 2000 elements are used to model the gauge area, as shown in Figure 5.13.

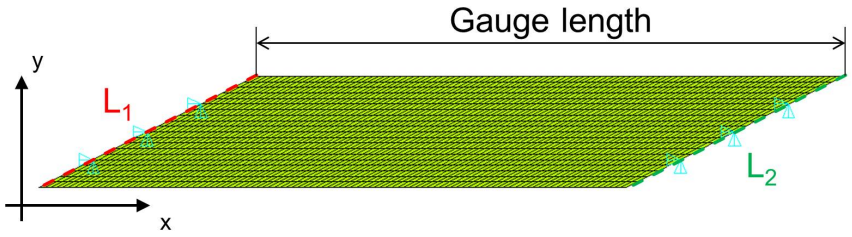

Figure 5.13: Ansys model of the off-axis specimen with oblique end-tabs

To model the experimental conditions, the line defined as L_1 is constrained in the x and y directions, while L_2 is constrained in the y direction and a displacement of 1 mm is applied on the x direction.
The analyses are run varying the end-tab angle from -7° to +7° around the correct end-tab angle for the CFRP1 and GFRP1 materials. The gauge length is kept constant. The presented results are the value of ϵ_{xx} normalised respectively by the global applied ϵ_{xx}.

The results for the CFRP1 material are shown in Figure 5.14.

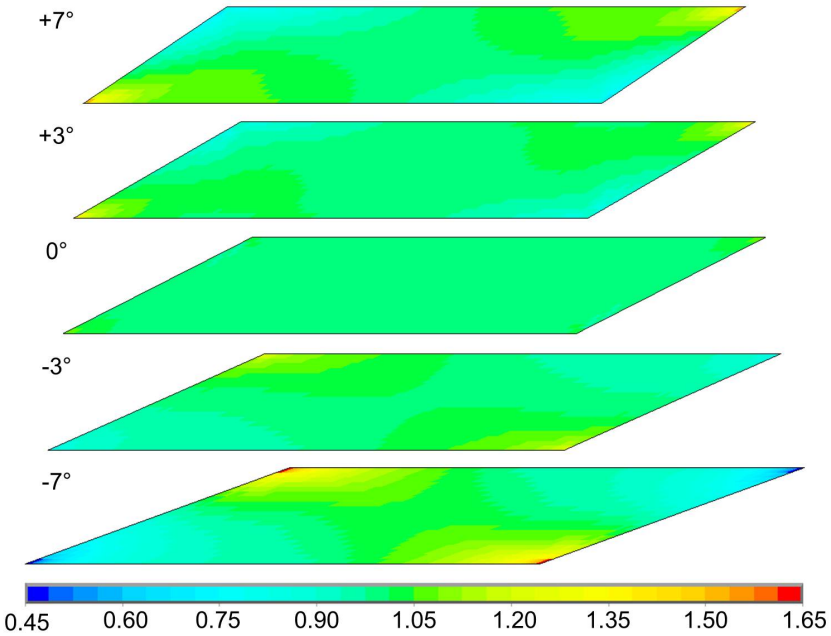

Figure 5.14: Normalised ϵ_{xx} strain for the CFRP1 material

The results for the GFRP1 material are shown in Figure 5.15.

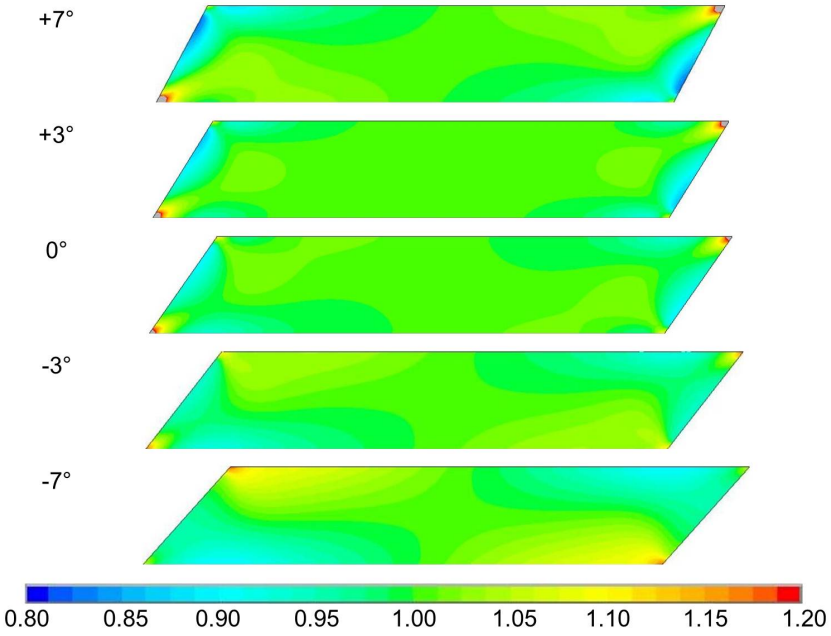

Figure 5.15: Normalised ϵ_{xx} strain for the GFRP1 material

From the strain data obtained with the model it is possible to evaluate the value of G_{12} as function of the error on the end-tab angle. Figure 5.17 plots the value of $\frac{Modulus_{wrong\ angle}}{Modulus_{correct\ angle}}$ against the error on the end-tab angle. The strains are extracted as average from an area in the centre of the gauge length.

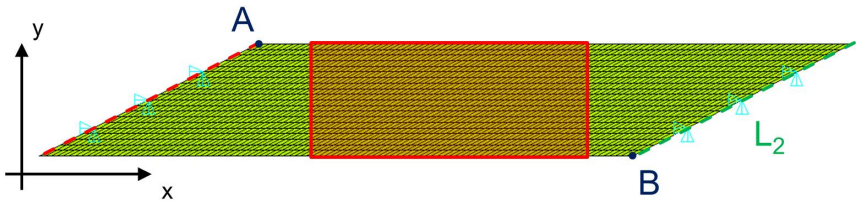

Figure 5.16: Ansys model: area of strain extraction for G_{12} calculation

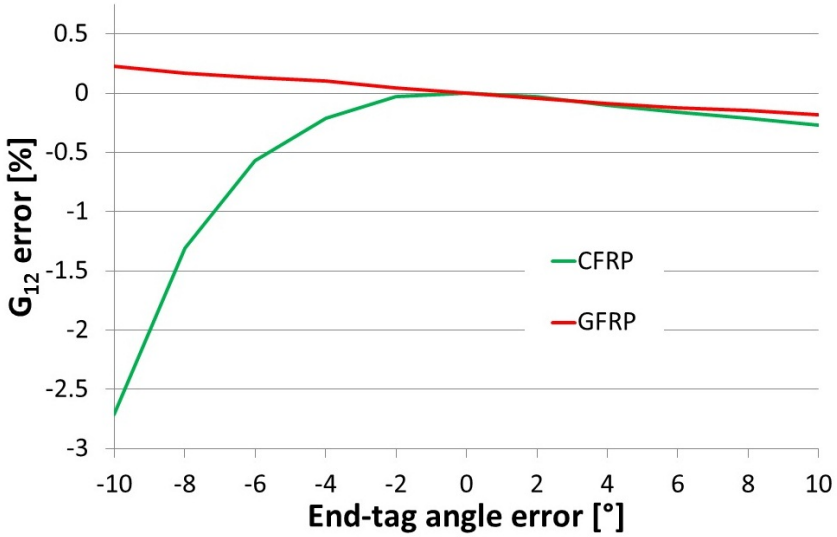

Figure 5.17: Error on G_{12} as function of the end-tab error

For the CFRP1 material, representative of composite materials with high E_{11}/E_{22} and E_{11}/G_{12} ratios, an error of $+7°$ in the end-tab estimate leads to significant values of strain concentration near the end-tab, even if the strain state in the centre of the specimen can still be assumed to be homogeneous. An error of -7° in the end-tab estimate leads to significant values of strain concentration near the end-tab that has an effect also in the centre of the specimen. This is caused by the fact that the gauge length is kept constant and therefore the distance between the strain concentration points, A and B in Figure 5.16, is reduced and the strain concentration areas interact. This effect can be observed also in the error on G_{12}, as shown in Figure 5.17.

For the GFRP1 material, representative of composite materials with low E_{11}/E_{22} and E_{11}/G_{12} ratios, the effects of the errors in the end-tab are less severe. The central part of the specimen presents homogeneous stress and strain states with errors on the end-tab up to $\pm 7°$. It can be observed in Figure 5.17 that G_{12} is mildly affected by errors on the end-tab angle estimation.

5.4 Experimental work

5.4.1 Preliminary tests

The specimens were manufactured with MTM58FRB/HS(24K)-450-38%RW (Umeco) pre-preg material stacked in a unidirectional lay-up and cured accordingly to the manufacturer's specification. According to the procedure devised in Section 5.1, three batches of specimens were used in the preliminary test phase. The characteristics of these are summarised in Table 5.4.

Table 5.4: Specimen characteristic for preliminary tests

Fibre orientation angle ϑ	Gauge length [mm]	Thickness [mm]	Width [mm]
0°	80	0.9	15
10°	80	1.8	15
90°	80	4.5	15

Square end-tabs were used. The specimen were manufactured with co-cured end-tabs to exploit the advantages offered by this configuration, as explained in Section 3.3.3. The specimen thickness of the 0° and 10° was chosen to guarantee a failure load of about 20 kN. For the 90° specimens, where a significantly lower failure load was expected, the thickness was the maximum value that allowed the end-tabbed specimen to be fitted in the machine clamping system.

Low speed testing

The test set-up is described in Figure 2.19 of Section 2.3.4. The specimens were loaded using a Series 5560, servo-electric, dual column, Instron test machine. The strain results obtained from the front and the back of the specimens were averaged and used to plot the stress-strain curves. The characteristics of the measurements performed on the front and the back of the specimen are reported in Table 5.5 and 5.6.

Table 5.5: Imaging characteristics for Stereo DIC on the front of the specimen for low speed preliminary tests

Technique	DIC
Software	DaVis 8.0.8
Subset size	31 x 31 pixels
Step size	10 pixels
Camera	AVT Manta G-504
Lens	AF NIKKOR 50 mm
Resolution	2452 x 2056 pixels
Field of view	96 x79 mm
Frame rate	1 Hz
Spatial Resolution	0.384 mm
Displacement Resolution	0.02 pixels
Strain Resolution	0.27 mε

Table 5.6: Imaging characteristics for Stereo DIC on the back of the specimen for low speed preliminary tests

Technique	DIC
Software	DaVis 8.0.8
Subset size	31 x 31 pixels
Step size	10 pixels
Camera	AVT Manta G-504
Lens	AF NIKKOR 50 mm
Resolution	2452 x 2056 pixels
Field of view	98 x 80 mm
Frame rate	1 Hz
Spatial Resolution	0.391 mm
Displacement Resolution	0.021 pixels
Strain Resolution	0.25 mε

The stress-strain curves obtained from the preliminary tests at a actuator displacement speed of 0.6 mm/min are shown in Figures 5.18 to 5.19.

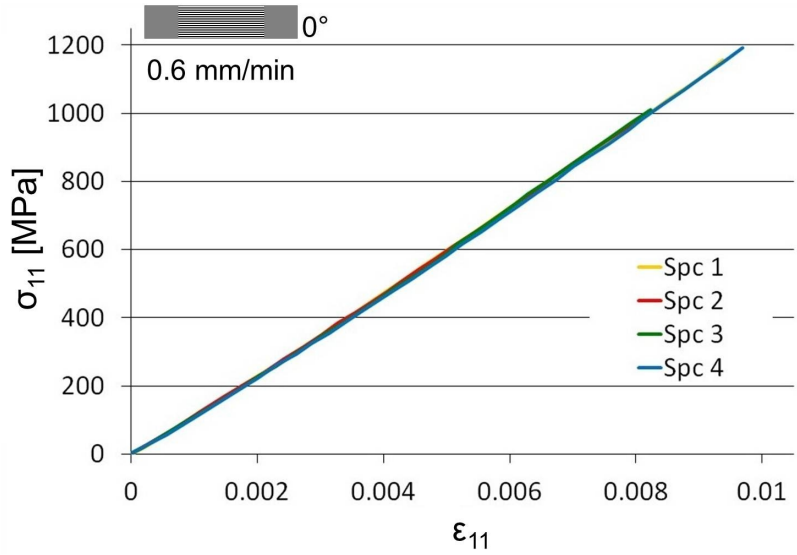

Figure 5.18: Stress-strain curve for the identification of E_{11} at 0.6 mm/min

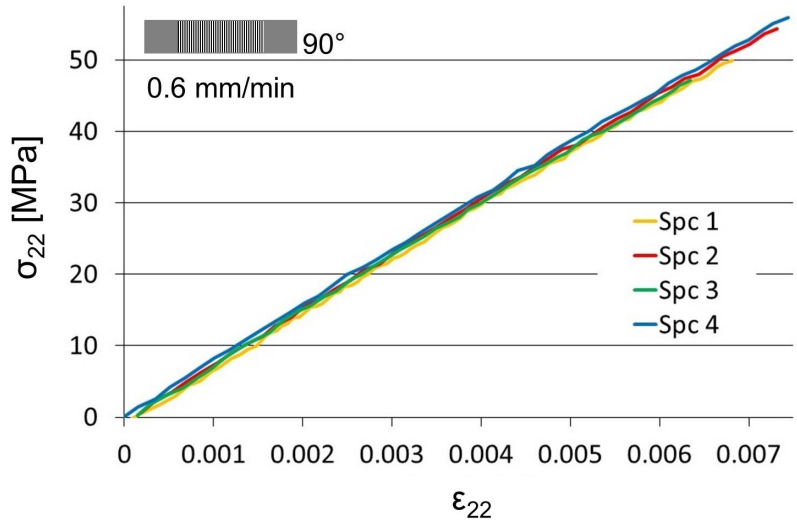

Figure 5.19: Stress-strain curve for the identification of E_{22} at 0.6 mm/min

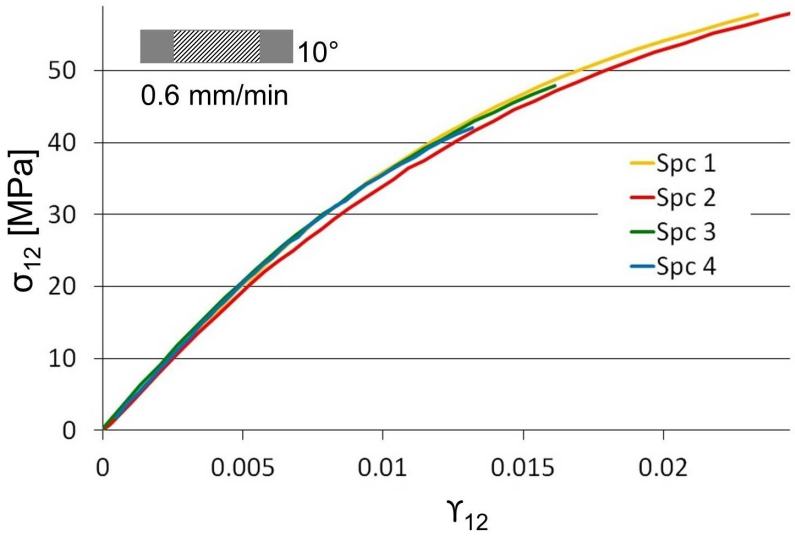

Figure 5.20: Stress-strain curve for the preliminary identification of G_{12} at 0.6 mm/min

The stress-strain curves obtained from the preliminary tests at a actuator displacement speed of 6 mm/min are shown in Figures 5.21 to 5.22.

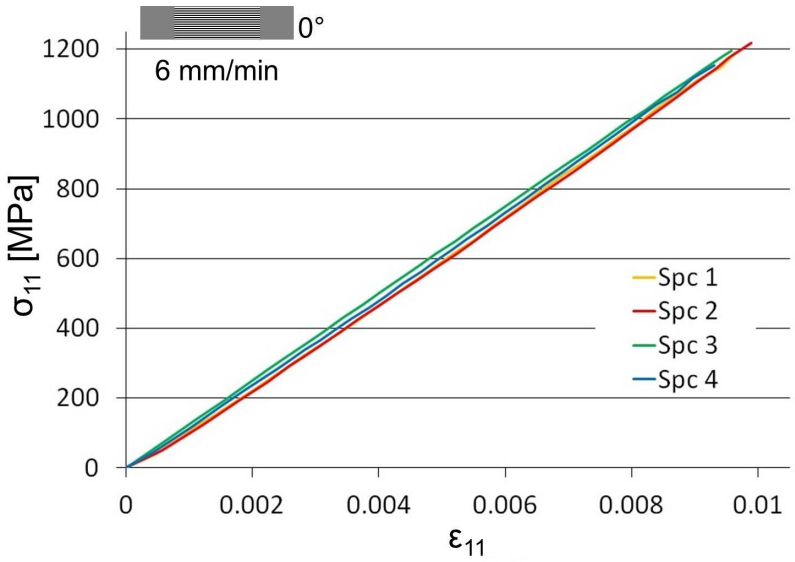

Figure 5.21: Stress-strain curve for the identification of E_{11} at 6 mm/min

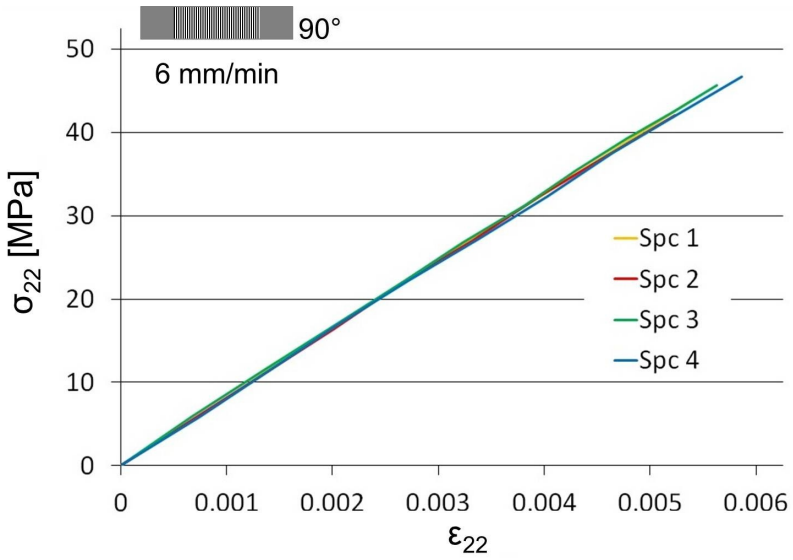

Figure 5.22: Stress-strain curve for the identification of E_{22} at 6 mm/min

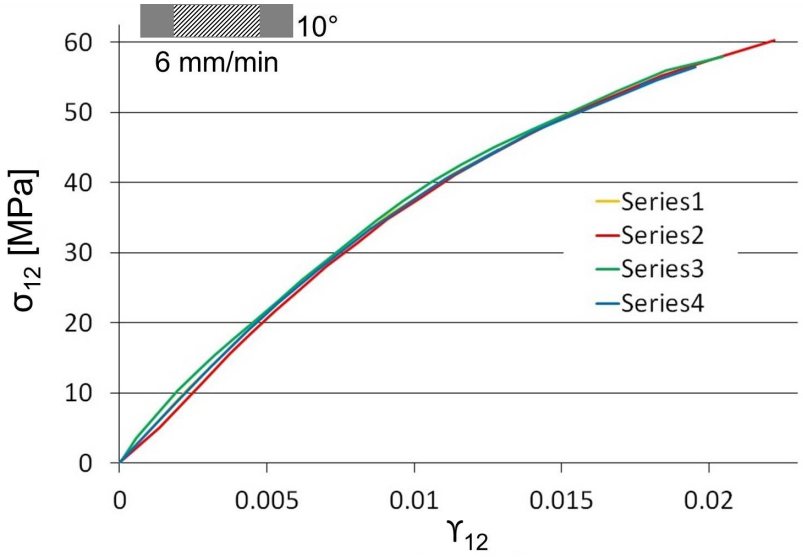

Figure 5.23: Stress-strain curve for the preliminary identification of G_{12} at 6 mm/min

The evaluated material properties are shown in Table 5.10.

High speed testing

The test set-up is described in Figure 3.19 (Section 3.4.3) with the illumination described in Figure 3.22 (Section 3.4.4). The specimen is loaded using the high speed servo-hydraulic test machine described in Section 3.3.1. The characteristics of the measurements performed at high speed are reported in Tables 5.7 and 5.8.

Table 5.7: Imaging characteristics for Stereo DIC for high speed preliminary tests for 0.1 and 1 m/s

Technique	DIC
Software	DaVis 8.0.8
Subset size	31 x 31 pixels
Step size	10 pixels
Camera	Photron SA-1
Lens	Sigma 105 mm f/2.8
Resolution	235 x 680 pixels
Field of view	20.64 x 59.74 mm
Frame rate	25 kHz
Shutter speed	1/35000 s
Spatial Resolution	0.878 mm
Displacement Resolution	0.0011 pixel
Strain Resolution	0.47 mε

Table 5.8: Imaging characteristics for Stereo DIC for high speed preliminary tests for 5 m/s

Technique	DIC
Software	DaVis 8.0.8
Subset size	31 x 31 pixels
Step size	10 pixels
Camera	Photron SA-5
Lens	Sigma 105 mm f/2.8
Resolution	192 x 744 pixels
Field of view	21.59 x 83.68 mm
Frame rate	40 kHz
Shutter speed	1/40000 s
Spatial Resolution	1.124 mm
Displacement Resolution	0.0013 pixel
Strain Resolution	0.51 mε

The stress-strain curves obtained from the preliminary tests at a actuator displacement speed of 0.1 m/s are shown in Figures 5.24 to 5.26.

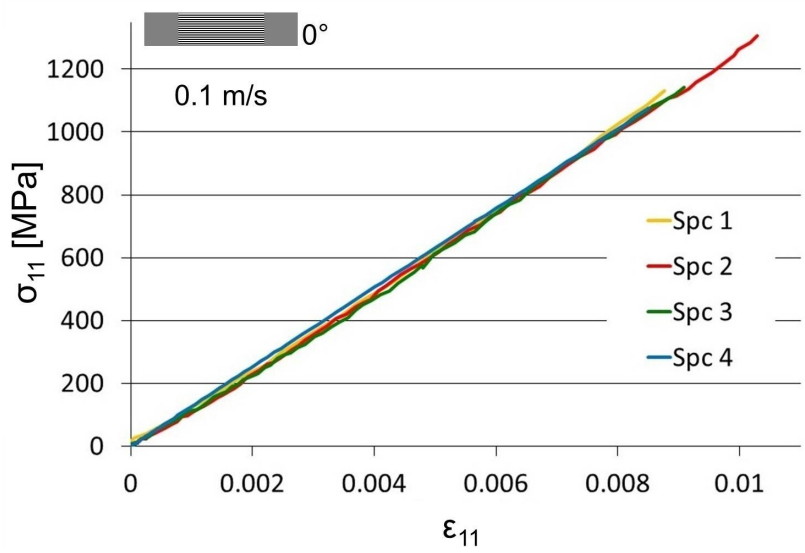

Figure 5.24: Stress-strain curve for the identification of E_{11} at 0.1 m/s

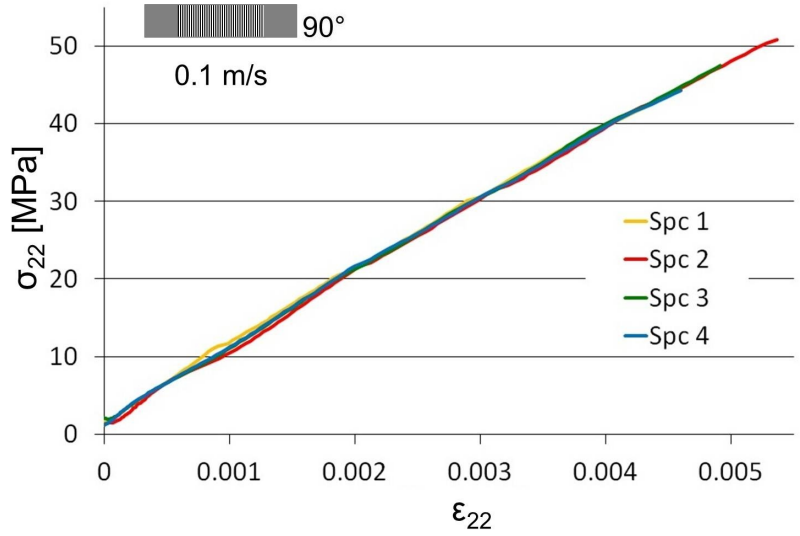

Figure 5.25: Stress-strain curve for the identification of E_{22} at 0.1 m/s

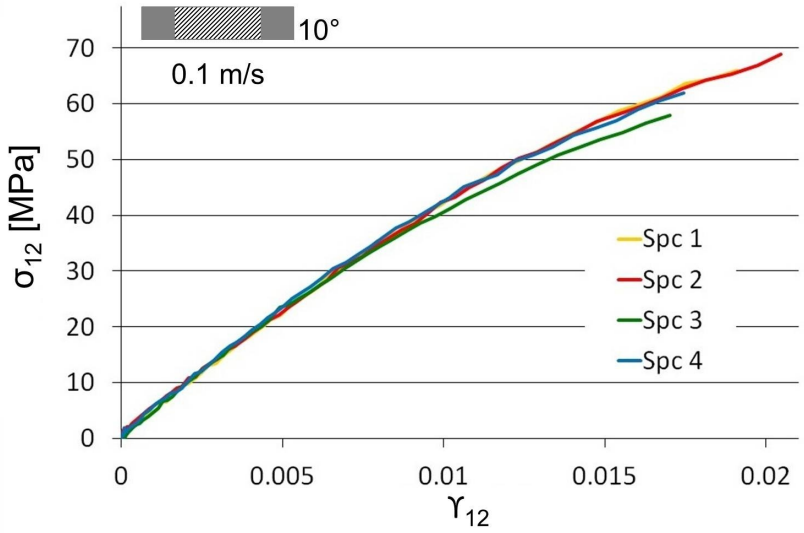

Figure 5.26: Stress-strain curve for the preliminary identification of G_{12} at 0.1 m/s

The stress-strain curves obtained from the preliminary tests at a actuator displacement speed of 1 m/s are shown in Figures 5.27 to 5.29.

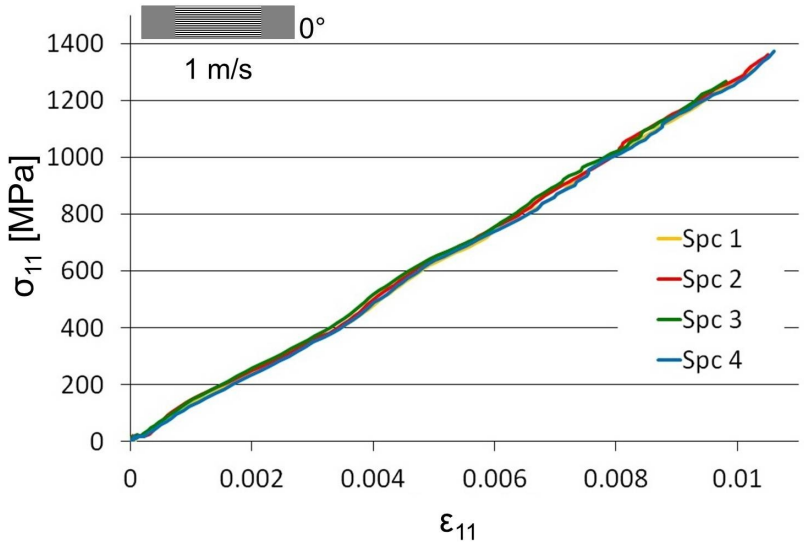

Figure 5.27: Stress-strain curve for the identification of E_{11} and ν_{12} at 1 m/s

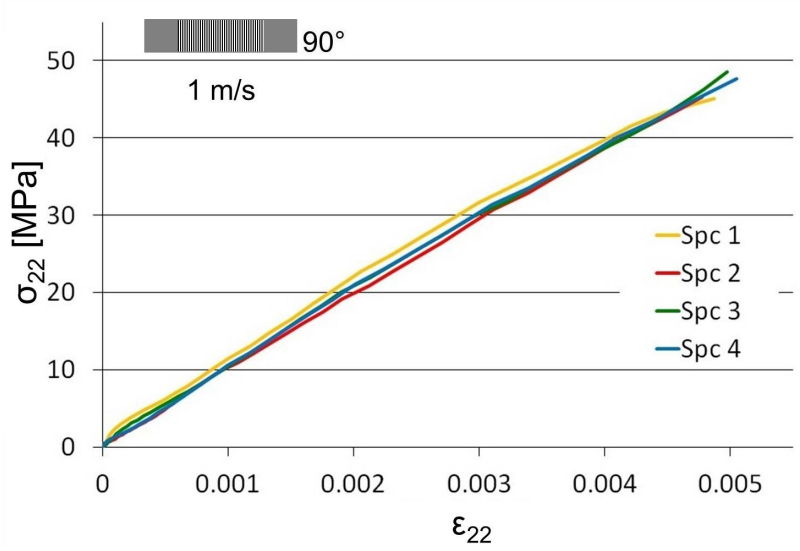

Figure 5.28: Stress-strain curve for the identification of E_{22} at 1 m/s

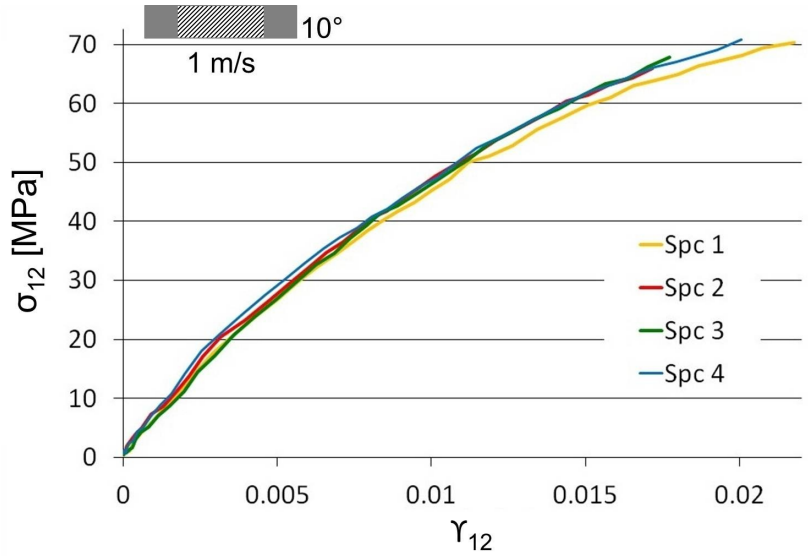

Figure 5.29: Stress-strain curve for the preliminary identification of G_{12} at 1 m/s

The stress-strain curves obtained from the preliminary tests at a actuator displacement speed of 5 m/s are shown in Figures 5.30 to 5.32.

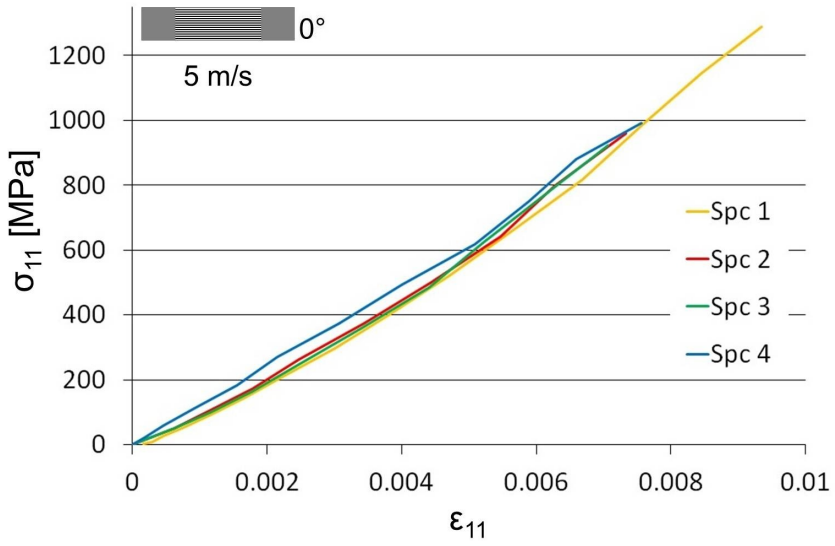

Figure 5.30: Stress-strain curve for the identification of E_{11} at 5 m/s

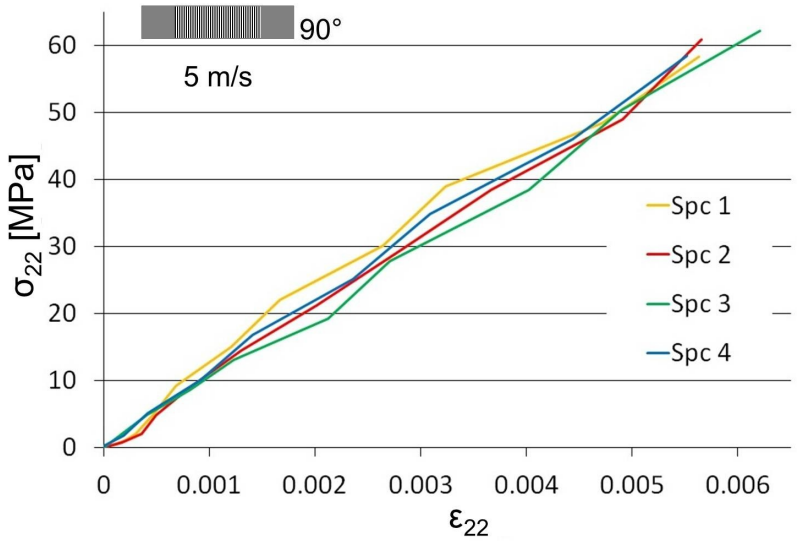

Figure 5.31: Stress-strain curve for the identification of E_{22} at 5 m/s

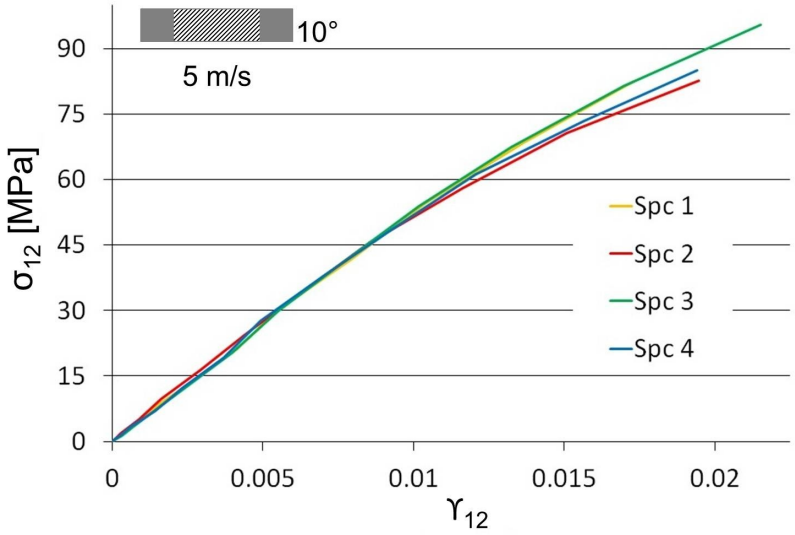

Figure 5.32: Stress-strain curve for the preliminary identification of G_{12} at 5 m/s

The evaluated material properties are shown in Table 5.10.

Preliminary tests outputs overview

At this stage it is important to remark some aspects that might affect the results quality and therefore the moduli identification at the different strain rates. Two different data acquisition systems have been used to acquire data when performing tests on the quasi-static servo-electric and the high-speed servo-hydraulic test machines. The two systems have different spatial resolutions, this marginally affects the results as the strain maps are averaged over the specimen surface to obtain the strain for a given load step. The two systems have also different but comparable strain resolution. Furthermore, identical specimens, i.e. with the same dimensions and same mechanical properties, have been used to perform the tests at different actuator displacement speeds. This is reflected by the number of data points that can be collected during the experiment duration. The average test duration and average number of data points obtained from the different tests are summarised in Table 5.9.

Table 5.9: Average test duration and number of data point used to define the stress-strain curve

Actuator displacement speed	0°		10°		90°	
	Test duration	Data points	Test duration	Data points	Test duration	Data points
	[s]		[s]		[s]	
0.6 mm/min	300	300	200	200	115	115
6 mm/min	35	35	20	20	10	10
	[ms]		[ms]		[ms]	
0.1 m/s	36	900	24	600	14	350
1 m/s	5.2	130	2.2	55	1.6	40
5 m/s	0.38	15	0.3	12	0.2	8

Furthermore observing Figures 5.27 and 5.31 the effect of the slack adaptor dynamic response, described in Section 3.3.2, appears evident on the stress strain curve. The effects of the dynamic response of the slack adaptor will be further discussed in Section 5.4.5.

Preliminary tests results and discussion

The longitudinal and transverse Young's moduli, E_{11} and E_{22}, are calculated considering the linear regression of the stress-strain curves. Following the methodology devised by Chamis and Sinclair, [91], the shear modulus, G_{12}, is determined from a linear regression of the segment of the σ_{12}-γ_{12} curve from 0 to 0.006 γ_{12}. According to the literature [63] the major Poisson's ratio is considered constant for the different strain rates, a value of 0.31 is obtained from the quasi-static tests.

The obtained results are summarised in Table 5.10.

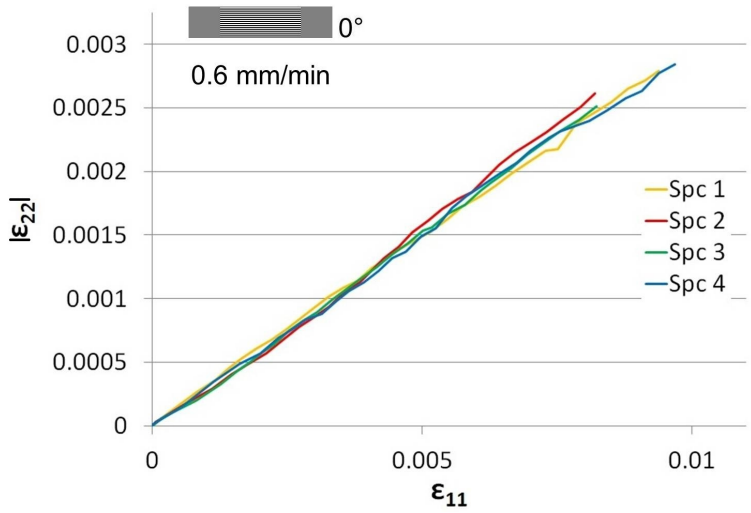

Figure 5.33: $|\epsilon_{22}|$-ϵ_{11} for major Poisson's ratio calculation from 0.6 mm/min tensile test

At this stage it is already possible to discuss the results relative to the longitudinal and transverse Young's moduli, i.e. E_{11} and E_{22}. In accordance with the majority of the results presented in the literature review in Section 3.2, both E_{11} and E_{22} appear to increase with the nominal strain rate. An analysis has been conducted to verify if the difference between the values obtained at different actuator speeds is statistically significant, as in Section 4.3.1. Analyses run for both E_{11} and E_{22} lead to the same results:

- Considering the data coming from the low and the high speed tests as two different groups it can be concluded that there is a statistically significant increase.
- Over the whole set of data the results obtained at 0.6 mm/min are statistically different from the ones obtained at 1 and 5 m/s.
- Among the results obtained at high actuator displacement speed the only statistically significant difference is between the results obtained at 0.1 and 5 m/s.

It can be concluded that the increase of E_{11} and E_{22} with actuator displacement speed is attributable to the material behaviour. In particular E_{11} increases by 4.6% and E_{22} by 37%.
The results relative to the longitudinal and transverse moduli will be used in Section 5.5 to model the strain rate material behaviour. Also G_{12} increases with the nominal strain rate. Accurate G_{12} values will be calculated in Section 5.4.3 from the oblique end-tab specimens, where a methodology for its identification from the stress strain curves will be defined.

Table 5.10: Summary of the preliminary test results in GPa

	0.6 mm/min			6 mm/min			0.1 m/s			1 m/s			5 m/s		
	E_{11}	E_{22}	G_{12}	E_{11}	E_{22}	G_{12}	E_{11}	E_{22}	G_{12}	E_{11}	E_{22}	G_{12}	E_{11}	E_{22}	G_{12}
Spc1	123.9	7.5	4.0	125.0	8.1	4.2	126.7	9.5	4.4	127.0	9.6	5.3	129.1	10.5	5.6
Spc2	123.2	7.5	3.9	125.0	8.0	4.2	126.2	9.5	4.4	128.0	9.6	5.4	129.2	10.6	5.4
Spc3	124.0	7.5	4.0	124.9	8.0	4.1	125.4	9.5	4.6	127.8	9.6	5.4	129.2	10.0	5.4
Spc4	123.7	7.5	4.1	125.1	7.9	4.3	126.3	9.5	4.6	127.4	9.6	5.2	130.0	10.1	5.5
Average	123.7	7.5	4.0	125.0	8.0	4.2	126.2	9.5	4.5	127.5	9.6	5.3	129.4	10.3	5.5
CV [%]	0.28	0.08	2.32	0.07	1.04	1.32	0.44	0.30	2.15	0.35	0.10	1.92	0.35	2.97	1.60

5.4.2 Off-axis tests definition

From the data summarised in Table 5.10 it is possible to evaluate the optimal off-axis tensile test angle, ϑ, and the correspondent oblique end-tab angle, φ. The results are summarised in Table 5.11.

Table 5.11: Optimal off-axis and correspondent end-tab angle

Actuator displacement speed		Off-axis angle ϑ [°]	End-tab angle φ [°]
0.6	mm/min	11	21
6	mm/min	11	22
0.1	m/s	11	23
1	m/s	12	24
5	m/s	12	25

As explained in Section 5.3.1, it would be possible to perform all the tests at the same off axis angle, between 10° and 15° , provided that the end-tab angle is correct. The specimens were manufactured with the off-axis angle reported in Table 5.11, errors of the order of ±2° might occur but, as discussed in Section 5.3.2, they have limited effect on G_{12} identification.

5.4.3 Shear modulus identification tests

The specimens for the shear modulus identification tests were manufactured according to the parameters summarised in Table 5.11. It was not possible to use co-cured end-tabs at this stage because of manufacturing difficulties. The oblique end-tabs were therefore bonded using SA-80 toughened low energy curing epoxy adhesive film, produced by Gurit. To keep the same nominal strain rate the gauge length was kept the same as the one used in the preliminary tests, 80 mm; width and thickness were respectively 15 and 1.35 mm.

The σ_{12}-γ_{12} curves obtained from the off-axis tensile tests performed at the different actuator displacement speeds are shown in Figures 5.34 to 5.38.

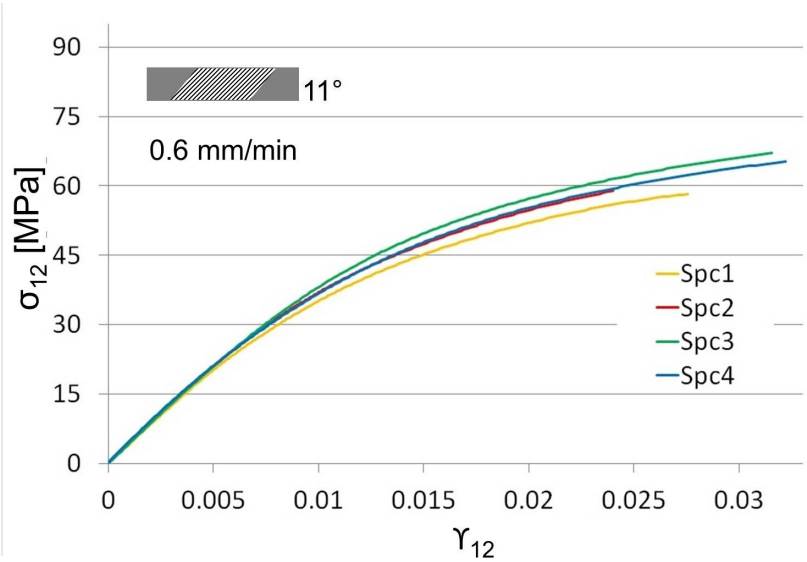

Figure 5.34: Stress-strain curve for the identification of G_{12} at 0.6 mm/min

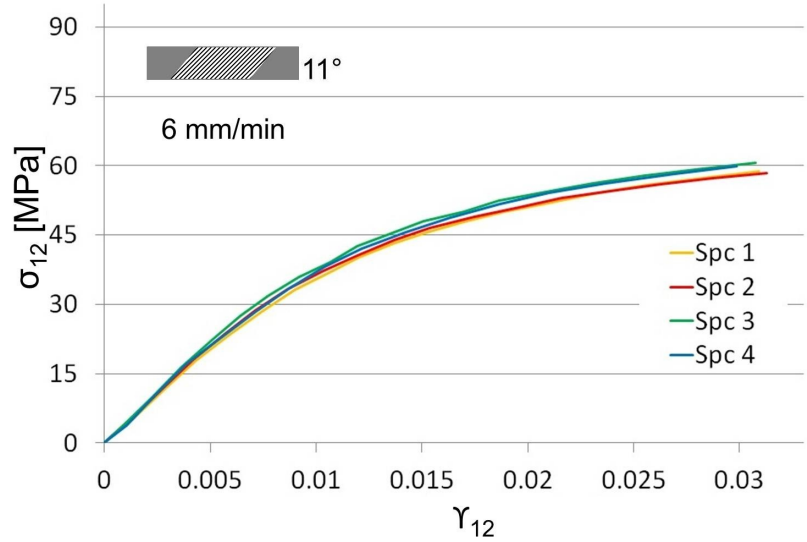

Figure 5.35: Stress-strain curve for the identification of G_{12} at 6 mm/min

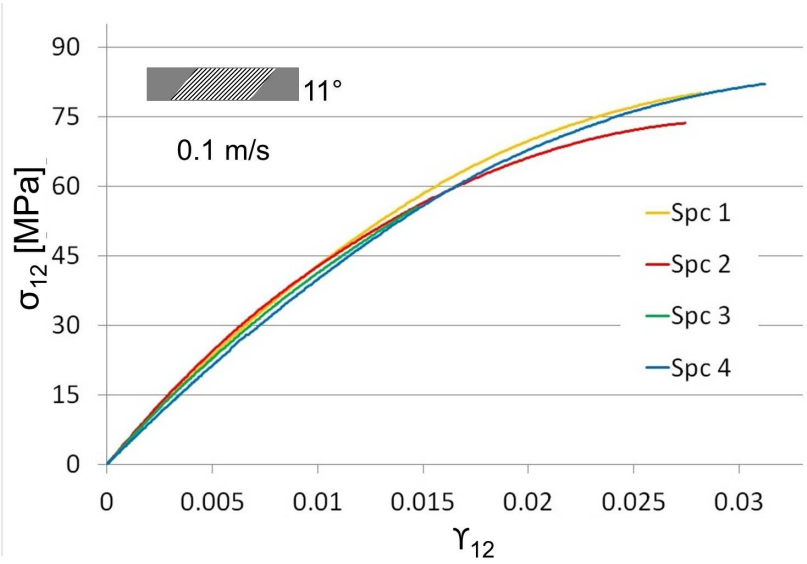

Figure 5.36: Stress-strain curve for the identification of G_{12} at 0.1 m/s

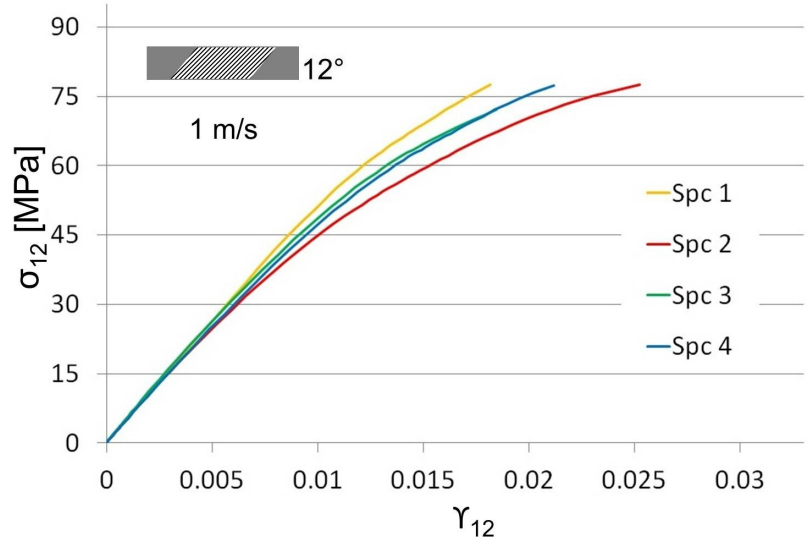

Figure 5.37: Stress-strain curve for the identification of G_{12} at 1 m/s

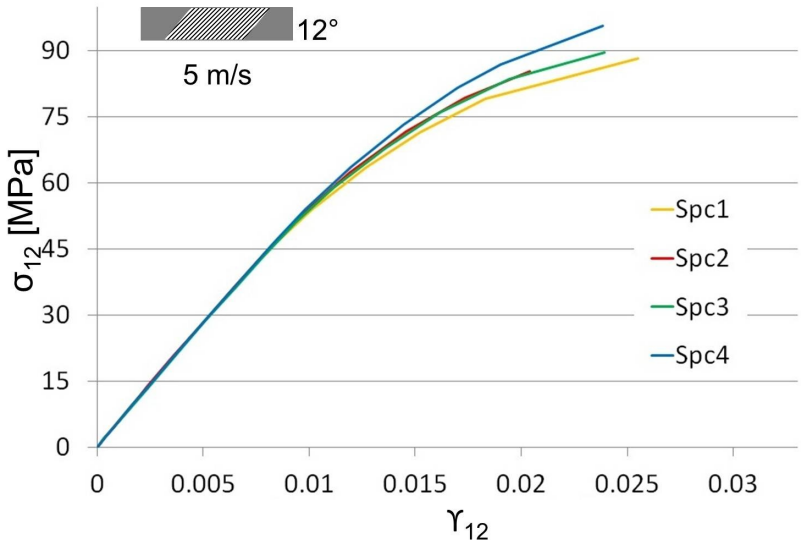

Figure 5.38: Stress-strain curve for the identification of G_{12} at 5 m/s

Comparing the five Figures above, an increase of the failure stress and a reduction of the failure strain with strain rate appears evident. This cannot be observed when using square end-tabs, Section 5.4.1. This is due to the use of oblique end-tab that relieve the stress concentration, and avoid premature failure, as shown in Figure 5.39. Furthermore, looking at Figures 5.34 to 5.38 an increase of the "linear region" in the first part of the stress-strain curve can be observed, this effect can also be observed in Figure 5.39.

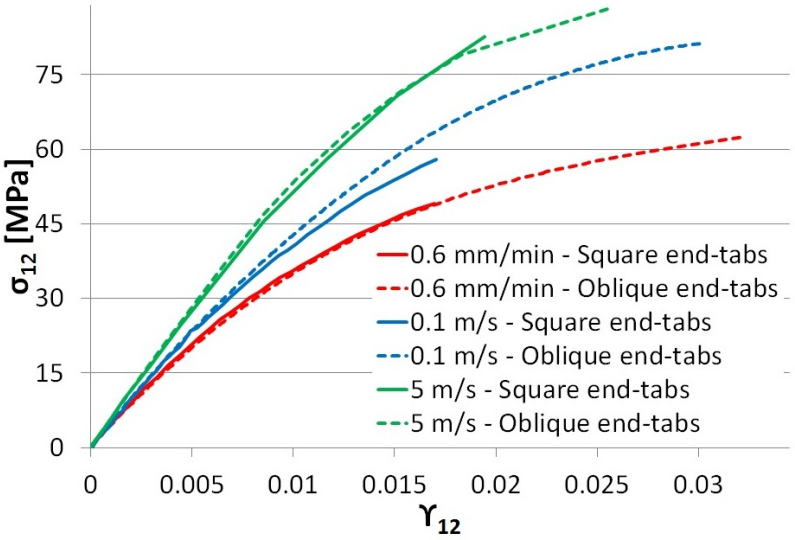

Figure 5.39: Stress-strain curves obtained with square and oblique end-tabs.

Furthermore, observing the stress-strain curve of the shear behaviour of CFRP, the linearity makes it difficult to unequivocally define a modulus through a simple

linear fitting over the whole curve. The identification method used to define G_{12} in Section 5.4.1 is not suitable as it was finalised only to capture the general trend of the initial shear behaviour with the finality to define the oblique end-tab angle. In the examined literature, none of the authors clearly stated how the shear modulus was defined in their work, as mentioned in Section 3.2. It is decided here to define two ways to identify initial shear modulus, representative of the elastic behaviour of the material:

- **Tangent modulus** The tangent modulus at data point $(\sigma\text{-}\gamma)_n$ is calculated as the slope of the linear regression from point $(\sigma\text{-}\gamma)_{n-2}$ to point $(\sigma\text{-}\gamma)_{n+2}$, as shown in Figure 5.40.

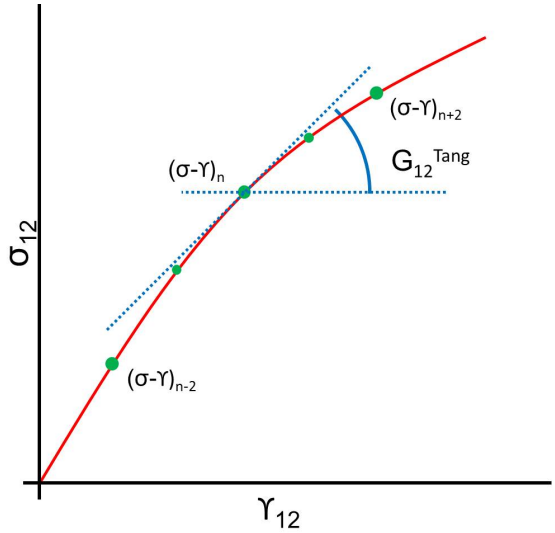

Figure 5.40: Schematic of the tangent shear modulus calculation

  The value of the tangent shear modulus is defined as the average of the tangent moduli calculated from point $(\sigma\text{-}\gamma)_3$ to point $(\sigma\text{-}\gamma)_{l-1}$ where point $(\sigma\text{-}\gamma)_l$ is the point where the tangent modulus drops by 5% from the average of the calculated shear tangent moduli.

- **Secant modulus** The secant modulus at data point $(\sigma\text{-}\gamma)_n$ is calculated as:

$$Secant\ G_{12} = \frac{\sigma_n}{\gamma_n} \tag{5.10}$$

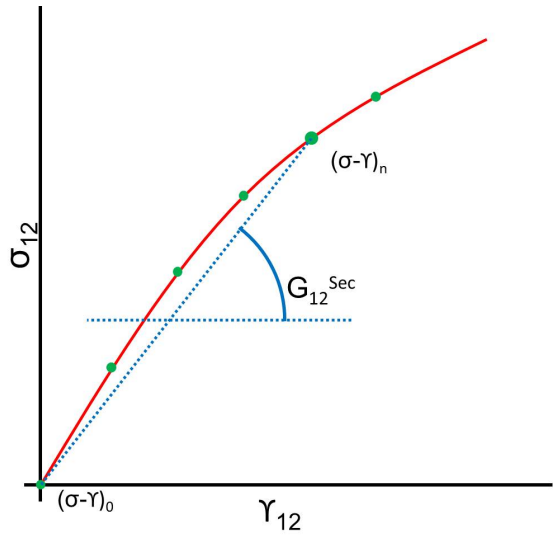

Figure 5.41: Schematic of the secant shear modulus calculation

The value of the secant shear modulus is defined as the average of the secant moduli calculated from point $(\sigma\text{-}\gamma)_0$ to point $(\sigma\text{-}\gamma)_{l\text{-}1}$ where point $(\sigma\text{-}\gamma)_l$ is the point where the secant modulus drops by a 5% from the calculated average of the shear secant moduli.

It is believed that these approaches allow the identification of the shear modulus when the damage caused by shear has not yet appeared in the material and the viscous behaviour of the resin is not yet the predominant deformation mechanism. The obtained shear moduli are summarised in Table 5.12. An example of the curves used to calculate tangent and secant G_{12} moduli from a low and a high speed test are shown in Figure 5.42 and 5.43.

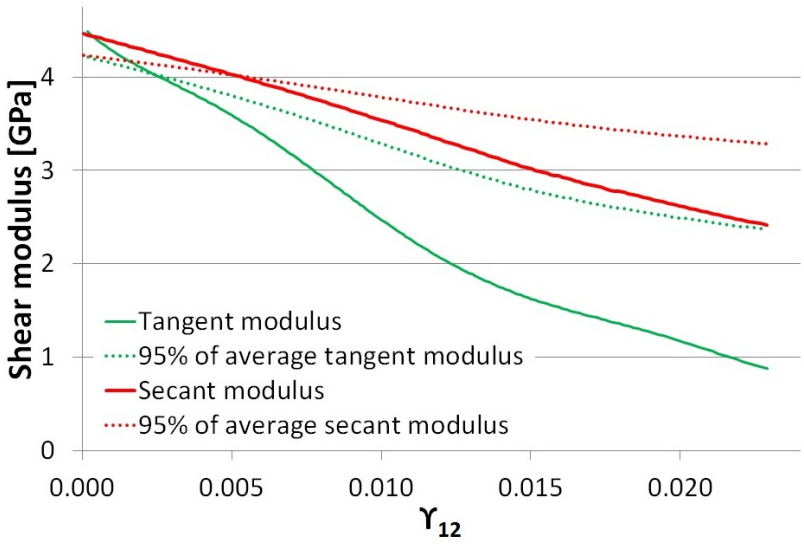

Figure 5.42: Tangent and secant shear moduli as function of strain: 0.6 mm/min test

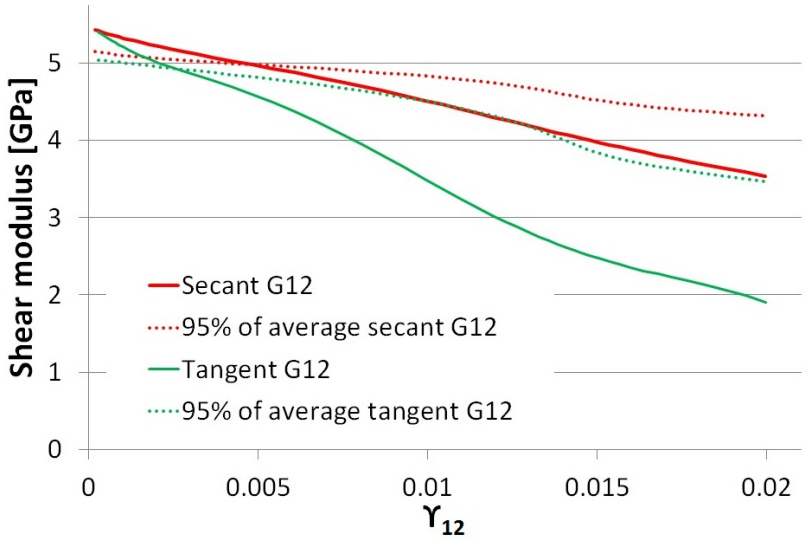

Figure 5.43: Tangent and secant shear moduli as function of strain: 1 m/s test

As for the preliminary results presented in Table 5.10, both the secant and tangent shear moduli increase with strain rate. The two shear moduli calculation methodologies produce consistent results. The only set of data point where a significant mismatch of the results can be observed is for 6 mm/min deformation speed. However it must be noticed that for this set of data the tangent modulus presents an high CV. The secant modulus identification method is less affected by the noisiness in the stress-strain curve and therefore is more robust than the tangent modulus method.

The same statistical analyses run in Section 5.4.1 for E_{11} and E_{22} is run here for the secant and tangent shear moduli. These led to similar results. Therefore the increases of 31% and 37% of the secant and the tangent moduli over the investigated actuator displacement speed range are attributable to the material behaviour.

The secant and tangent shear moduli results are used in Section 5.5 to model the strain rate dependent behaviour of the CFRP material studied here.

Table 5.12: Shear modulus GPa from oblique end-tab off-axis tests

	0.6 mm/min		6 mm/min		0.1 m/s		1 m/s		5 m/s	
	Secant	Tangent	Secant	Tangent	Secant	Tangent	Secant	Tangent	Secant	Tangent
Spc 1	4.1	3.9	4.3	3.8	4.9	4.9	5.2	5.2	5.4	5.8
Spc 2	4.2	4.2	4.3	3.1	5.1	5.0	5.2	5.1	5.7	5.6
Spc 3	4.2	4.1	4.5	4.1	4.9	4.3	5.5	5.6	5.5	5.5
Spc 4	4.2	4.1	4.4	3.8	4.6	4.3	5.2	5.1	5.4	5.5
Average	4.2	4.1	4.4	3.7	4.9	4.6	5.3	5.2	5.5	5.6
CV [%]	1.65	2.43	2.00	11.08	4.37	7.81	2.90	4.34	2.74	2.33

5.4.4 Benefits of the oblique end-tabs

As explained in Section 5.2 the use of oblique end-tabs is aimed at achieving of an uniform strain field over the specimen surface. The first way to verify if the end-tab angle is correct is to verify if the iso-displacement lines generated by the specimen stretching are parallel to the end-tabs. The longitudinal displacement maps for a quasi-static and a high speed test, are shown in Figures 5.44 and 5.45 alongside the finite element model results, Figure 5.46.

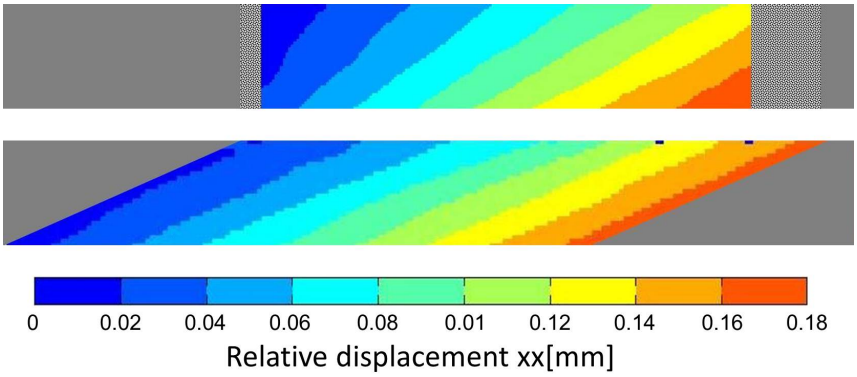

Figure 5.44: Displacement maps for a quasi-static test

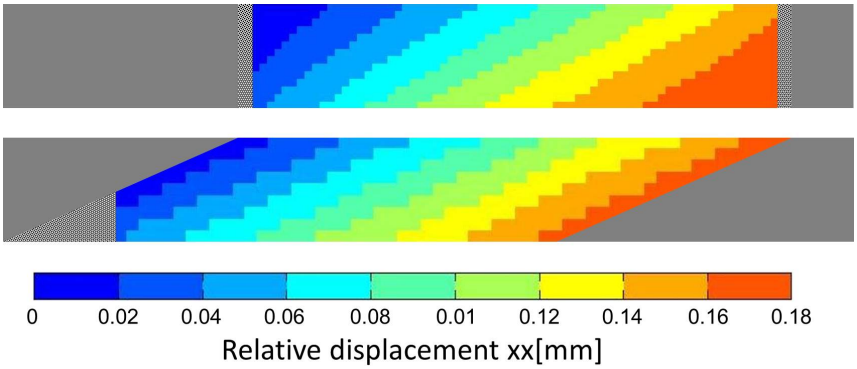

Figure 5.45: Displacement maps for a 5 m/s test

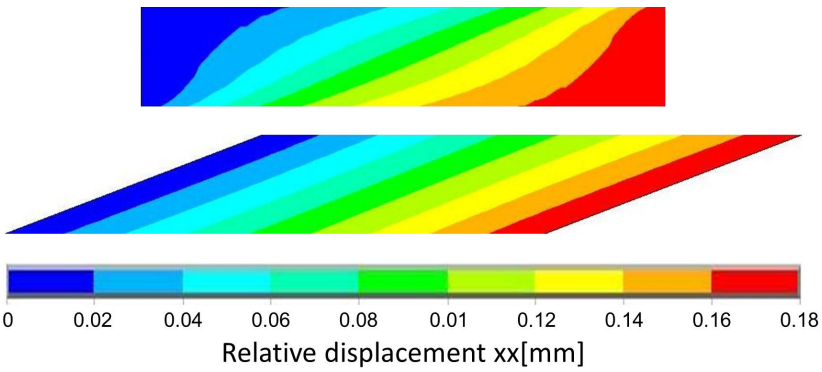

Figure 5.46: Displacement maps from finite element model

In both cases the specimens with oblique end-tabs show parallel iso-displacement lines, in good agreement with the finite element results. The benefits of the oblique end-tabs are also visible in the strain field, as shown in Figures 5.47 and 5.48. The finite element results are shown in Figure 5.49.

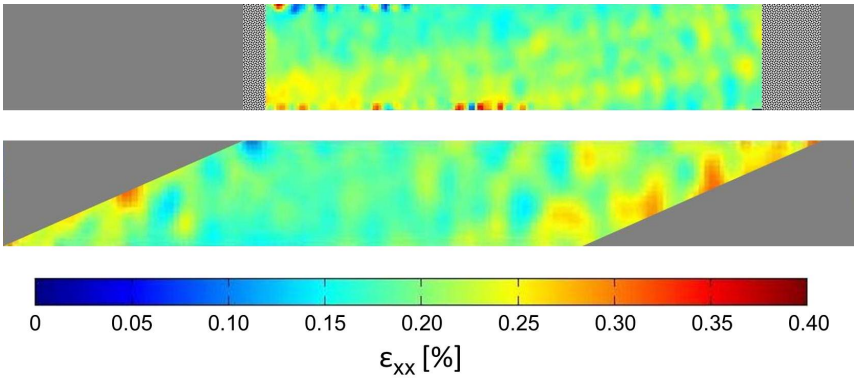

Figure 5.47: Strain maps for a quasi-static test

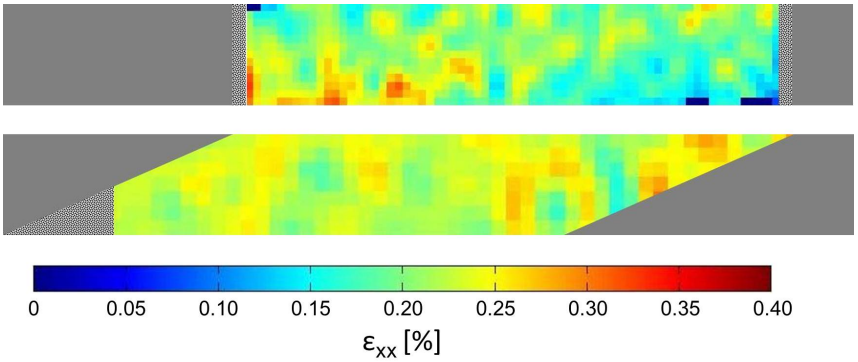

Figure 5.48: Strain maps for a 5 m/s test

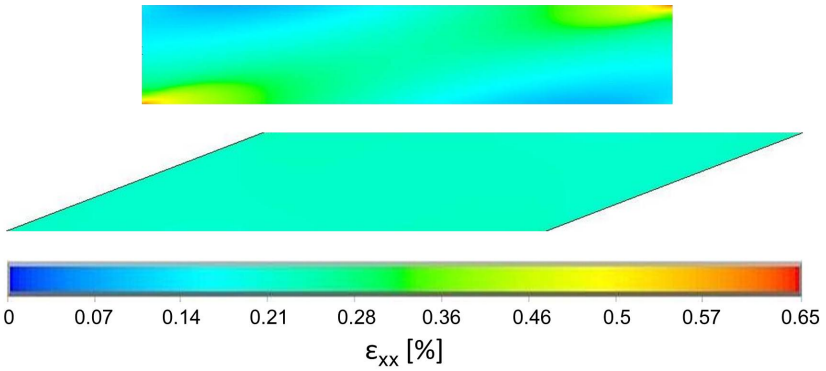

Figure 5.49: Strain maps for finite element model

The effects of the use of the two kinds of end-tabs on the shear strain in the material axes are shown in Figures 5.50 and 5.51. The finite element results are shown in Figure 5.52.

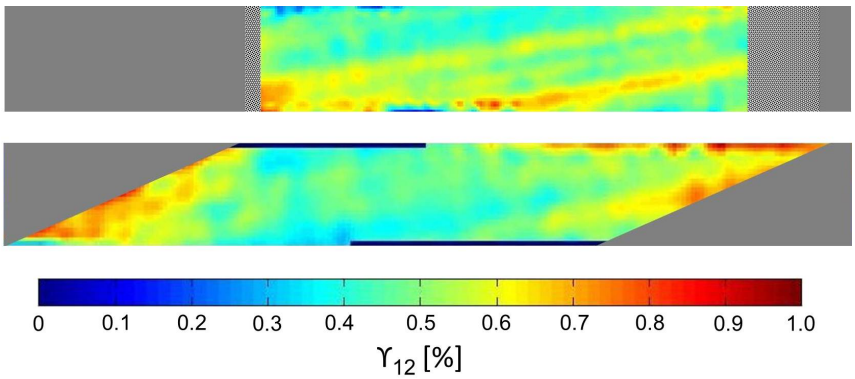

Figure 5.50: Shear strain maps in the material axes for a quasi-static test

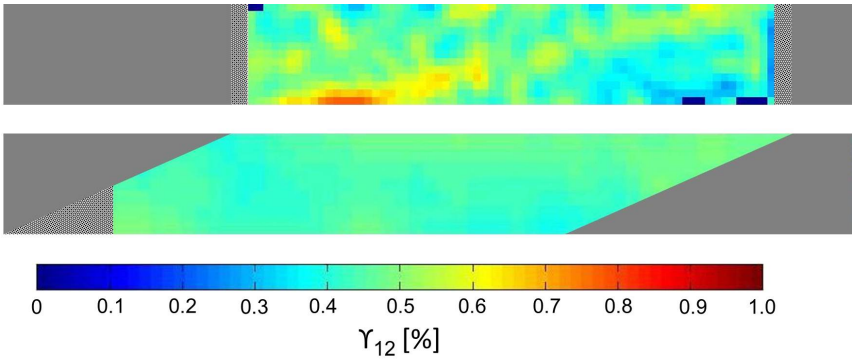

Figure 5.51: Shear strain maps in the material axes for a 5 m/s test

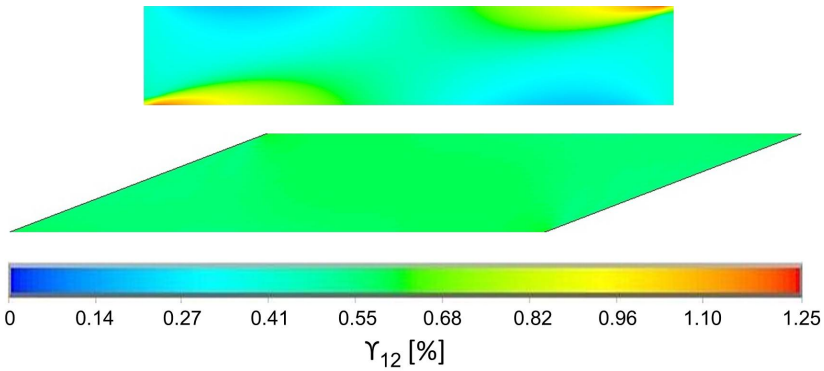

Figure 5.52: Shear strain maps in the material axes for finite element model

The oblique end-tabs lead to a more uniform shear strain field over the specimen surface.

The use of full-field strain measurement techniques allows not only the values of strain to define the stress-strain curve to be obtained, but also to observe the strain state over the entire specimen surface and verify the correct development of the tests.

5.4.5 Strain rate analysis and dynamic response of the slack adaptor

As highlighted in Section 5.4.1, the outputs of the high speed tests are affected by the dynamic response of the slack adaptor. This can be observed in the stress-strain curves. A generic study of the dynamic response of the slack adaptor was presented in Section 3.3.2. With the collected data it is now possible to observe its effects on the stress and stain and how it ultimately affects the properties that are measured here. Typical stress and strain values plotted against time, obtained from a test at a actuator displacement speed of 0.1 m/s on an off-axis specimen with oblique end-tab, are shown in Figure 5.53.

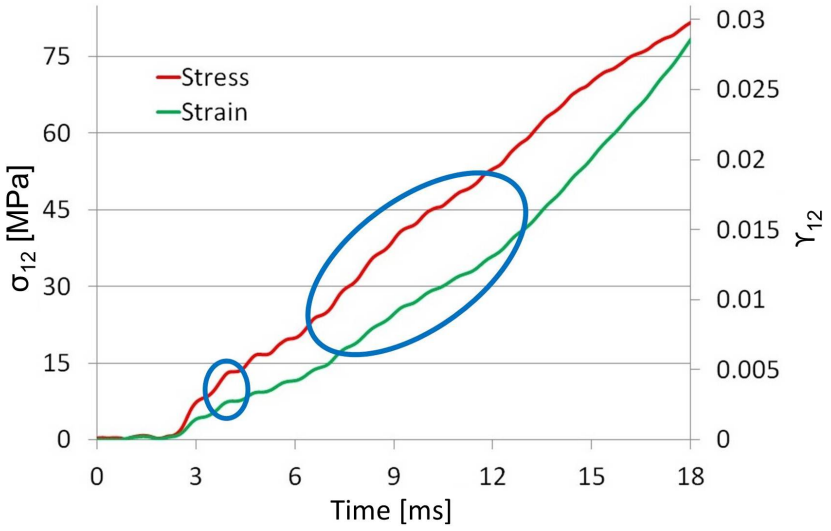

Figure 5.53: Stress and strain vs. time

Two periodic oscillations with different frequencies, shown in the blue circles, can be easily identified. The signal was then analysed through a fast Fourier transform, with results shown in Figure 5.54, to identify the characteristic frequencies of the observed oscillations.

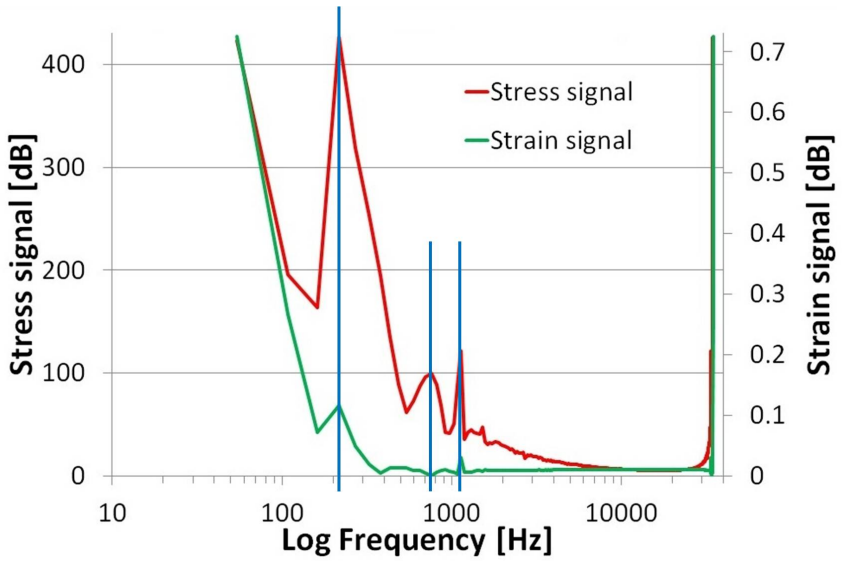

Figure 5.54: Fast Fourier transformation of the stress and strain signals

The FFT of both stress and strain signals present the same shape with the peaks of the dynamic response at the same frequencies. A modal analysis like the one run in Section 3.3.2 is run with the material properties and dimensions suitable to model the behaviour of the off-axis specimen. The results are summarised in Table 5.13, the conventions are the same as that used in Section 3.3.2.

Table 5.13: Modal analysis results

Mode	Frequency [Hz]	Part	Shape	Direction
1	70	All	Flex	z
2	72	Spc	Flex	y
3	194	Spc	Flex	y
4	379	Spc	Flex	y
5	493	All	Tors	x
6	625	Spc	Flex	y
7	731	All	Flex	z
8	930	All	Flex	y
9	1011	All	Flex	y
10	1089	All	Flex	z

The responses to mode 1 and 2 happen at frequencies too slow to be recorded during the observation time. The torsional effects cannot be observed on the stress or strain signals. The specimens offer a higher flexural stiffness in the z than in the y direction. Therefore the dynamic effects observed in the stress and strain signals are the oscillations in the y direction. The peaks of the FFT shown in Figure 5.54 coincide with the modal frequencies 3, 8 and 9 of Table 5.13. It can be therefore concluded that the oscillations of the stress and strain signals shown in Figure 5.53

are caused by the dynamic response of the specimen-slack adaptor system. As these happen in synchronisation in this cases they have no effect on the stress-strain curves. The same analysis was run on all the experimental results leading to the same conclusions. It is believed that in the 1 and 5 m/s actuator displacement speed tests the system responds in the same way, however the duration of the tests and the number of data points does not allow an FFT to be performed to verify this hypothesis. When the strain is differentiated over time to obtain the strain rate, the dynamic response of the specimen-slack adaptor has the effect of increasing the noise on the strain rate, as shown in Figure 5.55.

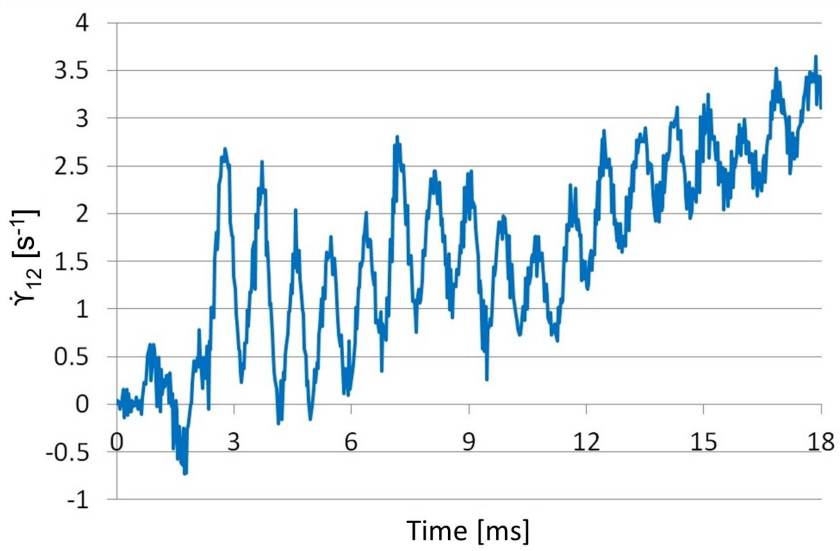

Figure 5.55: Effect of the dynamic response of the specimen-slack adaptor system at 0.1 m/s actuator displacement speed on the strain rate

The combination of the inertia effect described in Section 4.2.4 and the dynamic response makes it difficult to identify the strain rate of the studied events.
FFT transform was also performed on the strain rate signal, as shown in Figure 5.56.

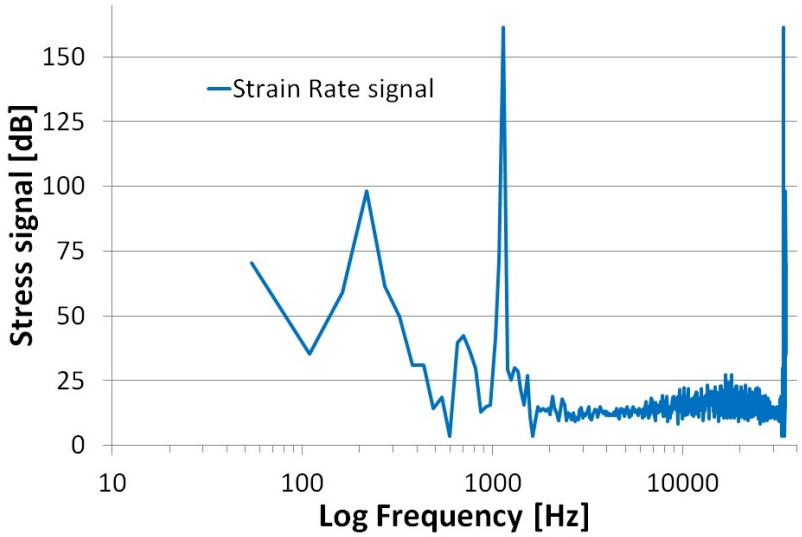

Figure 5.56: Fast Fourier transform of the strain rate signal

The peaks of the dynamic response are at the same frequencies as the ones of stress and strain signal, shown in Figure 5.54. The only difference in the two curves is the presence of high frequency noise introduced by the differentiation process.

5.5 Material strain rate dependent behaviour modelling

In this section the longitudinal, transverse and shear moduli summarised in Tables 5.10 and 5.12 are used in combination with the regression function described by Equation 3.1 proposed by Shokrieh and Omidi in [48], [49] [50] and [51], and recalled below, to describe the strain rate dependence of these properties:

$$M\left(\dot{\epsilon}\right) = \alpha + \beta\dot{\epsilon}^{\chi} \tag{5.11}$$

Considering what was discussed in Section 4.2.4 about the impossibility of achieving a uniform strain rate over the whole test duration, and the effect of the slack adaptor dynamic response, Section 5.4.5, it is not possible to unequivocally define the strain rate of the tests. The analysis of the results is therefore based on the nominal strain rate, calculated with Equation 4.2, recalled below:

$$\dot{\epsilon} = \frac{V}{L} \tag{5.12}$$

where V is the actuator speed and L the gauge length.

The average of the values used to inform the regression function model are sum-

marised in Table 5.14.

Table 5.14: Moduli summary in GPa as function of the strain rate

Strain rate	E_{11}	E_{22}	Secant G_{12}	Tangent G_{12}
$1.25{\cdot}10^{-4}$	123.7	7.5	4.2	4.1
$1.25{\cdot}10^{-3}$	125.0	8.0	4.4	3.7
1.25	126.2	9.5	4.9	4.6
12.5	127.5	9.6	5.3	5.2
62.5	129.4	10.3	5.5	5.6

The results obtained from the data fitting are shown in Figures 5.57 to 5.60.

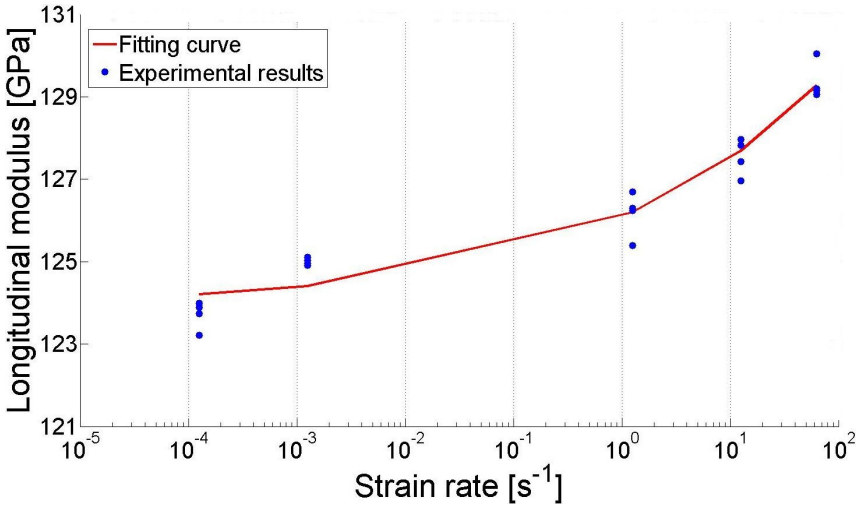

Figure 5.57: Longitudinal modulus strain rate dependence

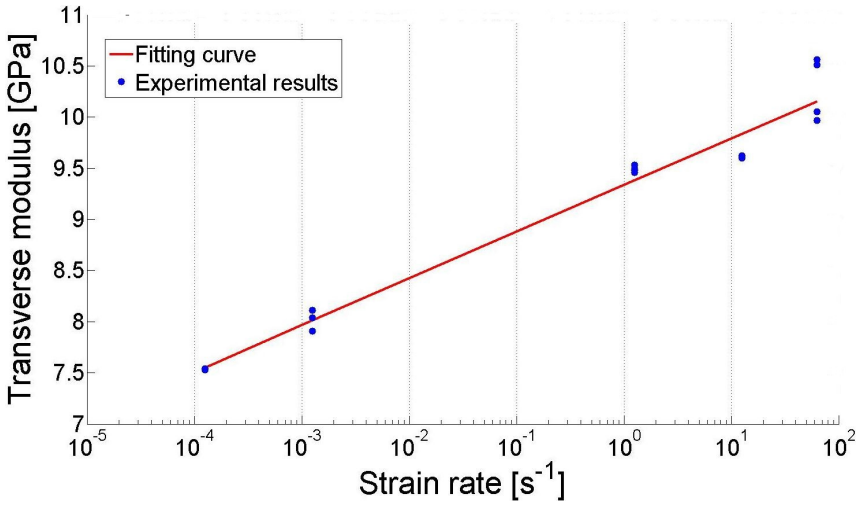

Figure 5.58: Transverse modulus strain rate dependence

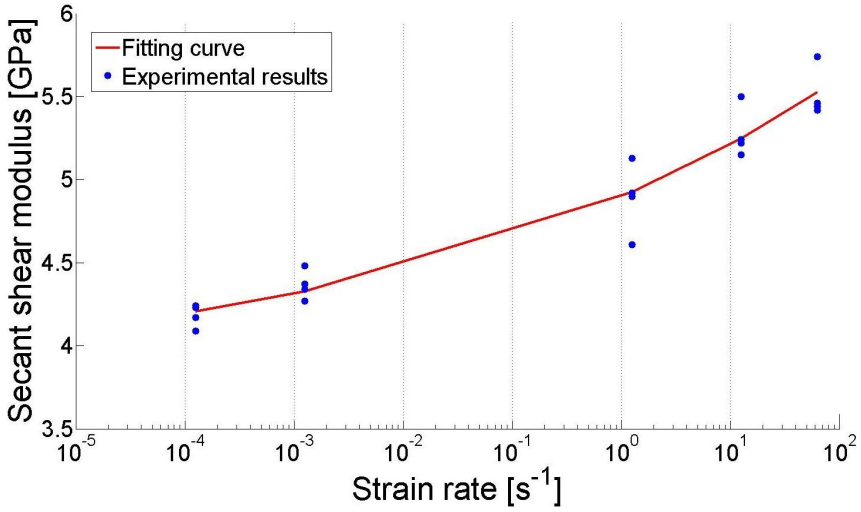

Figure 5.59: Secant shear modulus strain rate dependence

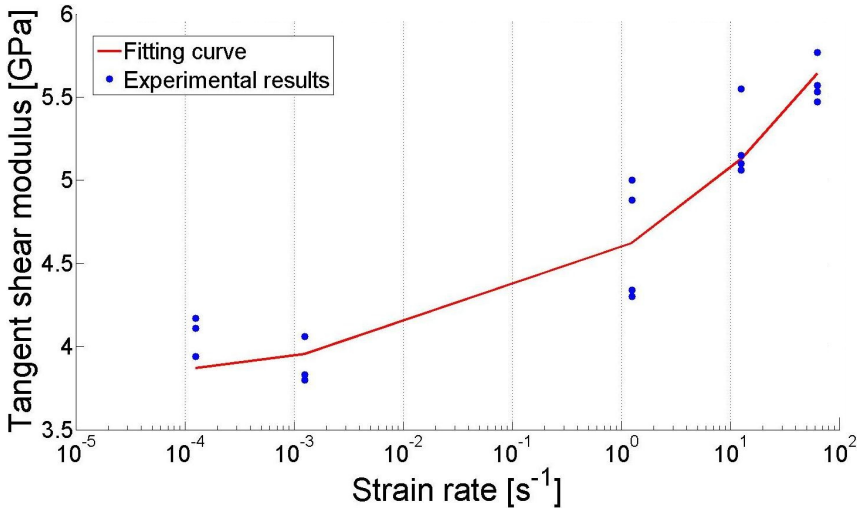

Figure 5.60: Tangent shear modulus strain rate dependence

Several computational runs were performed using different sets of initial fitting parameters. The material constants converged to the values summarised in Table 5.15 along with the coefficients of correlation R^2.

Table 5.15: Material constant for curve fitting describing longitudinal and transverse moduli behaviour

Constant		E_{11}	E_{22}	Secant G_{12}	Tangent G_{12}
α	[GPa]	$1.24\ 10^{2}$	$1.05\ 10^{2}$	$3.79\ 10^{0}$	$3.72\ 10^{0}$
β	[GPa·s]	$2.19\ 10^{0}$	$-9.52\ 10^{1}$	$1.11\ 10^{0}$	$8.66\ 10^{-1}$
χ		$2.18\ 10^{-1}$	$-2.10\ 10^{-3}$	$1.08\ 10^{-1}$	$1.93\ 10^{-1}$
R^2		0.968	0.985	0.997	0.950

Observing Table 5.15, and also considering the results obtained in Table 4.13 of Section 4.3.2, it can be observed that the constant α is comparable with the value

of the low strain rate modulus, while the constants β and χ are descriptive of the effects of strain rate on the modulus. In particular, β defines the rate of growth of the considered properties, while χ represents the curvature of the regression function. It appears evident how the results for E_{22} are in discordance with the other results. Even if the fitting curve shown in Figure 5.58 correctly describes the trend of the transverse modulus with strain rate, the constants are not representative of the material properties. Different fitting procedure have been tried, but for this case no satisfactory results could be achieved. To compare the strain rate dependence of the moduli the curves obtained with the regression function have been normalised by the respective quasi-static value and plotted in Figure 5.61.

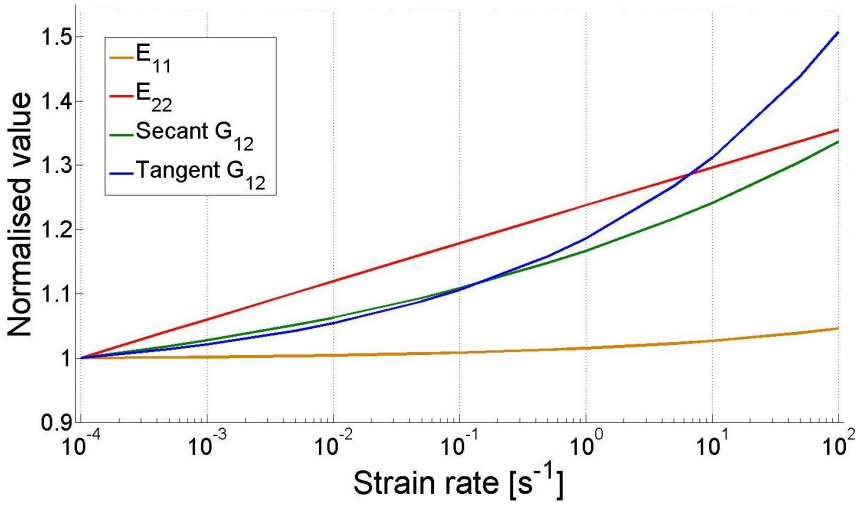

Figure 5.61: Normalised moduli against strain rates

It can be observed that the longitudinal modulus E_{11} is the less affected by the strain rate. E_{22} increases almost linearly, on a logarithmic scale, and its growth is comparable with secant G_{12}. Finally the strain rate has a higher effect on the tangent G_{12}.

5.6 Summary

A characterisation methodology to investigate the strain rate dependent behaviour of FRP material has been developed, verified and applied. The methodology can be summarised as follows:

1. Preliminary tensile tests on unidirectional laminates with 0° , 90° and 10 or 20° (respectively for CFRP and GFRP) fibre orientation with square end-tabs to identify E_{11}, E_{22}, ν_{12} and a preliminary value of G_{12}.

2. Definition of the off-axis and the oblique end-tab angle.

3. Optimised off-axis tensile test with oblique end-tabs to identify G_{12}.

The benefits of the use of the oblique end-tab have been widely discussed and can be summed up as the possibility to obtain a uniform strain field over the specimen surface, in the mitigation of the effects of the stress concentration in the transition area between specimen and end-tab and finally in a higher, and more realistic, failure stress. The effects of errors in the off-axis and end-tab angle have also been discussed. Furthermore the benefits of measuring strains with full-field optical techniques is the possibility of monitoring if the oblique end-tab angle is correct by observing the deformation and strain maps across the entire specimen.

As much as regards the experimental methodology, one of the main issues has been identified as the dynamic response of the slack adaptor that, even if it only marginally affects the general experimental outputs, makes the identification of some test parameters such as the real strain rate difficult.

6 Conclusions and future work

6.1 Overview

The objective of the research was to develop and apply full-field measurement techniques to the characterisation of FRP material constitutive behaviour in a strain rate range from quasi-static to 100 s^{-1}. The main body of this work can be divided in three parts:

1. Definition of a suitable experimental and imaging acquisition set-up, Chapters 2 and 3;
2. Validation of the developed methodology through the characterisation of a GFRP material, Chapter 4;
3. Application of the developed methodology to investigate the strain rate dependence of the stiffness of a CFRP material, Chapter 5.

The next section reports the main conclusions drawn during this research.

6.1.1 Novelty summary

The contributions of the research described in the thesis to the knowledge advancement in the field of FRP materials characterisation at intermediate strain rate with full-field strain measurement techniques, introduced in Section 1.3, can be summarised as follows:

- Development and validation of a new experimental methodology to perform test at strain rates between 0.01 and 100 s^{-1}:
  - Integration of VHS tensile test machine with high speed imaging.
  - New co-cured end-tab design for high speed testing.
  - Definition of a sound loading system for the VHS tensile test machine and the study of its impact on the specimen behaviour and test performance.
- Application of full-field strain measurement techniques traditionally used in quasi-static testing to higher strain rates:

  - Use of high speed imaging and full-field strain measurement techniques to achieve quantitative maps, validated with conventional techniques, of displacement, strain and strain rate over the whole specimen surface.
  - Direct comparison of DIC and GM on the same specimen.
  - Use of displacement and strain maps to verify the correct test configuration.

- Definition of a novel experimental procedure to study the strain rate dependence of longitudinal, transverse and shear moduli in FRP materials:
  - Application of off-axis tests on specimens with oblique end-tabs at intermediate strain rates to study FRP shear behaviour.
  - Definition of a robust method to identify the elastic shear modulus G_{12}.
  - Use of a regression function to describe the strain rate dependent behaviour of FRP materials constitutive moduli.

6.2 Conclusions

6.2.1 Experimental and imaging acquisition methodology

1. It has been demonstrated that the acquisition of biased images, that will lead to obtain biased strain maps and noisy stress-strain curves, can be prevented by an accurate set-up of the illumination apparatus, particularly by avoiding specular reflection on the specimen surface and image distortion caused by heat waves. Furthermore, the benefits of cold light sources has been demonstrated.

2. A slack adaptor system has been developed to clamp and load the specimen when performing high speed tests. It has been proven that the use of the slack adaptor overcomes the slippage issue that affects the fast jaw system and allows to minimise the out of plane movement. The slack adaptor behaviour has been studied and the main issue has been identified in the dynamic response triggered by the moment generated when the internal plunger and the outer cylinder engage.

3. A novel means to obtain a correct specimen loading in high speed tests, avoiding the end-tab debonding, by using co-cured end-tabs has been devised.

4. A suitable way to synchronise data coming from different acquisition systems has been identified in the use of a pulse generator to trigger the data acquisition and define an experimental time-zero.

5. A robust methodology based on full-field measurement techniques, able to produce repeatable and reproducible results, has been developed and validated.

6. The relevance of the maps obtained through the use of full-field measurement techniques is identified as:

   - The possibility to control the correct loading of the specimen observing the displacement maps. In particular it made possible to demonstrate the benefits of the oblique end-tabs, Section 5.4.4.
   - The possibility to visualise the strain distribution over the specimen surface and identify the strain concentration and damage localisation regions.

7. GM is more labour intensive and time consuming but allows to obtain a higher spatial resolution than the DIC. This will be of particular importance when the experimental methodology developed in this PhD programme will be used to measure non uniform strain fields with significant gradient.

6.2.2 Material characterisation and strain rate dependent behaviour

1. An experimental procedure that allows the characterisation of the strain rate dependent material behaviour through the use of full-field optical technique with a single test configuration has been devised and successfully applied. In particular the use of off-axis specimens with oblique end-tabs has been demonstrated to be a suitable mean to investigate the shear constitutive behaviour of FRP materials.

2. The specimen design parameters and manufacturing process that might lead to the incorrect implementation of the off-axis tensile tests have identified and their impact on the experimental results have been quantified. Particularly errors in the order of $\pm 5^{\circ}$ in the oblique end-tab angle produce and error smaller than 0.5% in the estimated G_{12}.

3. A consistent and reliable procedure to evaluate the initial secant and tangent shear modulus, G_{12}, was proposed and applied to real data in Section 5.4.3.

4. A simple but effective regression function was used to describe the strain rate dependent behaviour of FRP materials. This allowed to identify the strain rate dependence of the constitutive properties of the investigate GFRP and CFRP materials.

- **GFRP** An increase of 14% of the E_{11} value was observed in a strain rate range from quasi-static to 80 s^{-1}.
- **CFRP** Over a strain rate range from quasi-static to 62.5 s^{-1} an increase of 4.6% was observed for E_{11}, the moduli governed by the matrix dominated material behaviour, E_{22} and G_{12}, showed an increase in the order of 35%.

6.3 Recommendations for future work

The presented research has resulted in the development of a methodology for the investigation of the strain rate dependent behaviour of FRP materials. It is anyway acknowledged that in this thesis the capabilities of full-field measurement techniques are not exploited at their best. This research has proved the suitability of full-field optical techniques to measure uniform strain fields during high deformation speed events and investigate the linear behaviour of materials. The importance of the obtained results lie in fact that the usefulness of this technique to acquire data suitable for material characterisation has been demonstrated. This is an essential first step to further exploit these techniques for material characterisation in the future. Two potential applications are of particular interest:

- Data collected with full-field strain measurement techniques can be used to inform models of the non-linear behaviour of materials, especially when contact strain measurement techniques are not able to provide information.
- The virtual fields method (VFM) [35] can be used to optimise the constitutive parameters identification process extracting full-field strain maps from specimens able to generate a non uniform strain fields.

6.3.1 High speed full-field measurement techniques

The VFM is based on the virtual work principle that can be written as follows for a given solid of volume V, as the one shown in Figure 6.1.

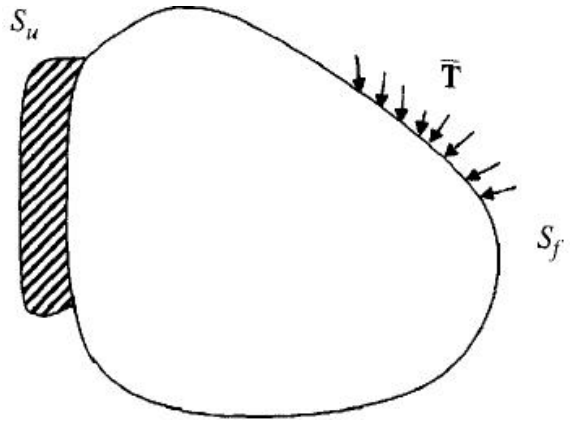

Figure 6.1: Solid of any shape loaded at its boundary from [35]

$$-\int_V \sigma : \epsilon^* dV + \int_{S_f} \bar{T}.u^* dS + \int_V f.u^* dV = \int_V \rho a.u^* dV \tag{6.1}$$

where σ is the actual stress tensor, u^* and ϵ^* are the virtual displacement vector and strain tensor respectively, $\bar{T}$ is the distribution stress vector acting on the boundary S_f, f is the distribution of volume forces acting on V, ρ is the mass per unit volume and a the acceleration. A virtual displacement field is a test function for which the previous equation is verified, and a virtual strain tensor is a strain tensor derived from a given virtual displacement vector. It is important to underline that the above equation is verified for any virtual field (u^*) continuous and differentiable across the volume and compatible with the boundary conditions. At this stage, the constitutive equations are introduced in the form of:

$$\sigma = g(\epsilon) \tag{6.2}$$

where g is a given function containing the constitutive parameters. Equation 6.1 can than be written as:

$$-\int_V g(\epsilon) : \epsilon^* dV + \int_{S_f} \bar{T}.u^* dS + \int_V f.u^* dV = \int_V \rho a.u^* dV \tag{6.3}$$

Any new virtual field in Equation 6.3 will lead to a new equation involving the constitutive parameters. Choosing the correct shape and number of virtual fields allows to write a set of equations that can be used to extract the unknown constitutive parameters.

The key issue of the method is the choice of the number and the shape of the virtual fields. Two cases can be distinguished in the selection of g, as explained by Grédiac *et al.* [10]:

- The constitutive Equation 6.2 depend linearly on the constitutive parameters. Provided that the actual strain field is heterogeneous and that a number of

independent virtual fields equal to the unknowns is chosen it is possible to write a linear system which, after inversion, allows to calculate the constitutive parameters .

- The constitutive Equation 6.2 is a non linear functions of the constitutive parameters. The identification strategy relies in this case on the minimisation of a residual constructed with Equation 6.3.

Therefore full-field displacement and strain fields obtained with optical techniques can be used to inform the VFM from experiment that involves:

- the use of specimens that generates non uniform strain fields, e.g. the T-shaped specimen proposed by Grédiac and Pierron [9];
- obtaining full-field maps also for non linear material behaviour.

6.3.2 Strain rate dependent behaviour study of CFRP

The data collected in Chapter 5 could also be used to inform a model to describe the non linear shear behaviour of CFRP. A polynomial stress/strain relationship like the one of Equation 6.4 can be used to describe the progressive shear damage.

$$\sigma_{12} = G_{12}\gamma_{12} - k\gamma_{12}^3 \tag{6.4}$$

where σ_{12} and γ_{12} are the shear stress and strain respectively, G_{12} is the shear modulus and k is a positive real number representative of the damage evolution. This constitutive law can be directly fitted to the obtained data to define G_{12} and k or in combination with the VFM, as done by Grédiac *et al.* [110] or Chalal *et al.* [111].

References

[1] M. Ashby. *Materials Selection in Mechanical Design (3rd edition)*. Butterworth-Heinemann, 1999.

[2] EADS Deutschland GmbH Corporate Research Centre. The research requirements of the transport sectors to facilitate an increased usage of composite materials. Part 1: The composite material research requirements of the aerospace industry. 2004.

[3] R. M. Jones. *Mechanics of Composite Materials, Second Edition*. Taylor and Francis, Inc., 1999.

[4] R. K. Goldberg and A. Gilat. Experimental and computational characterization of the high strain rate tensile response of polymer matrix composites. *Composite Materials: Testing and Design*, 14(36):207–223, 2003.

[5] N. K. Naik, P. Yernamma, N. M. Thoram, R. Gadipatri, and V. R. Kavala. High strain rate tensile behavior of woven fabric E-glass/epoxy composite. *Polymer Testing*, 29(1):14–22, 2010.

[6] A. Gilat, R. K. Goldberg, and G. D. Roberts. Experimental study of strain-rate-dependent behavior of carbon/epoxy composite. *Composites Science and Technology*, 62(10-11):1469–1476, 2002.

[7] J. H. Kim, F. Pierron, M. R. Wisnom, and K. Syed-Muhamad. Identification of the local stiffness reduction of a damaged composite plate using the virtual fields method. *Composites Part A: Applied Science and Manufacturing*, 38(9):2065–2075, 2007.

[8] J. H. Kim, F. Pierron, M. R. Wisnom, and S. Avril. Local stiffness reduction in impacted composite plates from full-field measurements. *Composites Part A: Applied Science and Manufacturing*, 40(12):1961–1974, 2009.

[9] M. Grédiac and F. Pierron. A T-shaped specimen for the direct characterization of orthotropic materials. *International Journal for Numerical Methods in Engineering*, 41(2):293–309, 1998.

[10] M. Grédiac, F. Pierron, S. Avril, and E. Toussaint. The virtual fields method for extracting constitutive parameters from full-field measurements: a review. *Strain*, 42(4):233–253, 2006.

[11] R. Bardenheider and G. Rogers. *Dynamic Impact Testing*. Instron, 2003.

[12] B. Pan, K. Qian, H. Xie, and A. Asundi. Two-dimensional digital image correlation for in-plane displacement and strain measurement: a review. *Measurement Science and Technology*, 20(6):062001, 2009.

[13] S. Avril, E. Ferrier, A. Vautrin, P. Hamelin, and Y. Surrel. A full-field optical method for the experimental analysis of reinforced concrete beams repaired with composites. *Composites Part A: Applied Science and Manufacturing*, 35(7-8):873–884, 2004.

[14] R. K. Fruehmann, J. M. Dulieu-Barton, and S. Quinn. On the thermoelastic response of woven composite materials. *Journal of Strain Analysis for Engineering Design*, 43(6):435–450, 2008.

[15] M.A. Sutton, J.J. Orteu, and H. Schreier. *Image Correlation for Shape, Motion and Deformation Measurements: Basic Concepts, Theory and Applications*. Springer, 2009.

[16] J. E. Field, S. M. Walley, W. G. Proud, H. T. Goldrein, and C. R. Siviour. Review of experimental techniques for high rate deformation and shock studies. *International Journal of Impact Engineering*, 30(7):725–775, 2004.

[17] M. Grédiac. The use of full-field measurement methods in composite material characterization: interest and limitations. *Composites Part A: Applied Science and Manufacturing*, 35(7-8):751–761, 2004.

[18] M. Grédiac. *Importance of full-field measurement techniques for better models in solid mechanics*, chapter 6, pages 13–14. Springer Netherlands, 2007.

[19] Y. Pannier, S. Avril, R. Rotinat, and F. Pierron. Identification of elasto-plastic constitutive parameters from statically undetermined tests using the virtual fields method. *Experimental Mechanics*, 46(6):735–755, 2006.

[20] H. Chalal, S. Avril, F. Pierron, and F. Meraghni. Experimental identification of a nonlinear model for composites using the grid technique coupled to the virtual fields method. *Composites Part A: Applied Science and Manufacturing*, 37(2):315–325, 2006.

[21] R. Moulart, F. Pierron, S. Hallett, and M. Wisnom. Full-field strain measurement and identification of composites moduli at high strain rate with the virtual fields method. *Experimental Mechanics*, 51(4):509–536, 2011.

[22] G. Crammond, S. W. Boys, and J. M. Dulieu-Barton. Dynamic analysis of composite marine structures using full-field measurement techniques. *Submitted for publication*, 2014.

[23] H. Schreier, J. Braasch, and M. Sutton. Systematic errors in digital image correlation caused by intensity interpolation. *Optical Engineering*, 39(11):2915–2921, 2000.

[24] Z.-F. Zhang, Y.-L. Kang, H.-W. Wang, Q.-H. Qin, Y. Qiu, and X.-Q. Li. A novel coarse-fine search scheme for digital image correlation method. *Measurement*, 39(8):710–718, 2006.

[25] D. J. Chen, F. P. Chiang, Y. S. Tan, and H. S. Don. Digital speckle-displacement measurement using a complex spectrum method. *Applied Optics*, 32(11):1839–1849, 1993.

[26] H. A. Bruck, S. R. McNeill, M. A. Sutton, and W. H. III Peters. Digital image correlation using Newton-Raphson method of partial differential correction. *Experimental Mechanics*, 29(3):261–267, 1989.

[27] P.-C. Hung and A. S. Voloshin. In-plane strain measurement by digital image correlation. *Journal of the Brazilian Society of Mechanical Sciences and Engineering*, 25:215–221, 2003.

[28] H. Haddadi and S. Belhabib. Use of rigid-body motion for the investigation and estimation of the measurement errors related to digital image correlation technique. *Optics and Lasers in Engineering*, 46(2):185–196, 2008.

[29] H. W. Schreier and M. A. Sutton. Systematic errors in digital image correlation due to undermatched subset shape functions. *Experimental Mechanics*, 42(3):303–310, 2002.

[30] S. Yaofeng and J. H. L. Pang. Study of optimal subset size in digital image correlation of speckle pattern images. *Optics and Lasers in Engineering*, 45(9):967–974, 2007.

[31] K. Triconnet, K. Derrien, F. Hild, and D. Baptiste. Parameter choice for optimized digital image correlation. *Optics and Lasers in Engineering*, 47(6):728–737, 2009.

[32] C. Badulescu, M. Grédiac, J. Mathias, and D. Roux. A procedure for accurate one-dimensional strain measurement using the grid method. *Experimental Mechanics*, 49(6):841–854, 2009.

[33] C. Badulescu, M. Grédiac, and J. D. Mathias. Investigation of the grid method for accurate in-plane strain measurement. *Measurement Science and Technology*, 9:95–102, 2009.

[34] J.-L. Piro and M. Grédiac. Producing and transferring low-spatial-frequency grids for measuring displacement fields with Moiré and grid methods. *Experimental Techniques*, 28(4):23–26, 2004.

[35] F. Pierron and M. Grédiac. *The virtual fields method. Extracting constitutive mechanical parameters from full-field deformation measurements.* Springer, New York, 2012.

[36] University of Southampton. http://www.southampton.ac.uk/ engineering/ undergraduate/ modules/ sesg6031_experimental_mechanics.page, Last accessed Feb 2014.

[37] Meng L., Jin G., and Yao X. Errors caused by misalignment of the optical camera axis and the object surface in the DSCM. *Journal of Tsinghua University (Science and Technology)*, 46(11):1930–2, 1936, 2006.

[38] A Hijazi, A. Friedl, and C. J. Kähler. Influence of camera's optical axis non-perpendicularity on measurement accuracy of two-dimensional digital image correlation. *Jordan Journal of Mechanical and Industrial Engineering*, 5(4):373 – 382, 2011.

[39] Z. Liang, B. Yin, X. Dai, J. Mo, and S. Wang. Using camera calibration to apply digital image correlation outside the laboratory. *Optical Engineering*, 52(12):123102–123102, 2013.

[40] S. Yoneyama, A. Kitagawa, K. Kitamura, and H. Kikuta. In-plane displacement measurement using digital image correlation with lens distortion correction. *JSME International Journal Series A Solid Mechanics and Material Engineering*, 49(3):458–467, 2006.

[41] P. Lava, W. Paepegem, S. Coppieters, I. Baere, and D. Debruyne. *Impact of Lens Distortions on Strain Measurements Obtained with Digital Image Correlation*, chapter 33, pages 233–238. Conference Proceedings of the Society for Experimental Mechanics Series. Springer New York, 2013.

[42] A. M. S. Hamouda and M. S. J. Hashmi. Testing of composite materials at high rates of strain: advances and challenges. *Journal of Materials Processing Technology*, 77(1-3):327–336, 1998.

[43] R.L Sierakowski. Strain rate effects in composites. *ASME*, 1997.

[44] N. K. Naik and Yernamma Perla. Mechanical behaviour of acrylic under high strain rate tensile loading. *Polymer Testing*, 27(4):504–512, 2008.

[45] A. Owens and H. V. Tippur. A tensile split Hopkinson bar for testing particulate polymer composites under elevated rates of loading. *Experimental Mechanics*, 49(6):799–811, 2009.

[46] W. Wang, G. Makarov, and R. A. Shenoi. An analytical model for assessing strain rate sensitivity of unidirectional composite laminates. *Composite Structures*, 69(1):45–54, 2005.

[47] J. Fitoussi, F. Meraghni, Z. Jendli, G. Hug, and D. Baptiste. Experimental methodology for high strain-rates tensile behaviour analysis of polymer matrix composites. *Composites Science and Technology*, 65(14):2174–2188, 2005.

[48] M. M. Shokrieh and M. J. Omidi. Tension behavior of unidirectional glass/epoxy composites under different strain rates. *Composite Structures*, 88(4):595–601, 2009.

[49] M. M. Shokrieh and M. J. Omidi. Compressive response of glass-fiber reinforced polymeric composites to increasing compressive strain rates. *Composite Structures*, 89(4):517–523, 2009.

[50] M. M. Shokrieh and M. J. Omidi. Investigation of strain rate effects on in-plane shear properties of glass/epoxy composites. *Composite Structures*, 91(1):95–102, 2009.

[51] M. M. Shokrieh and M. J. Omidi. Investigating the transverse behavior of glass/epoxy composites under intermediate strain rates. *Composite Structures*, 93(2):690–696, 2011.

[52] J. Berthe, M. Brieu, E. Deletombe, G. Portemont, P. Lecomte-Grosbras, and A. Deudon. Consistent identification of CFRP viscoelastic models from creep to dynamic loadings. *Strain*, 49(3):257–266, 2013.

[53] G. C. Jacob, J. M. Starbuck, J. F. Fellers, S. Simunovic, and R. G. Boeman. Strain rate effects on the mechanical properties of polymer composite materials. *Journal of Applied Polymer Science*, 94(1):296–301, 2004.

[54] J. Harding and L. M. Welsh. A tensile testing technique for fibre-reinforced composites at impact rates of strain. *Journal of Materials Science*, 18(6):1810–1826, 1983.

[55] H. M. Hsiao, I. M. Daniel, and R. D. Cordes. Strain rate effects on the transverse compressive and shear behavior of unidirectional composites. *Journal of Composite Materials*, 33(17):1620–1642, 1999.

[56] A. Lowe. Transverse compressive testing of T300/914. *Journal of Materials Science*, 31(4):1005–1011, 1996.

[57] G. L. Melin and E. L. Asp. Effects of strain rate on transverse tension properties of a carbon/epoxy composite: studied by Moiré photography. *Composites Part A: Applied Science and Manufacturing*, 30(3):305–316, 1999.

[58] M. V. Hosur, J. Alexander, U. K. Vaidya, and S. Jeelani. High strain rate compression response of carbon/epoxy laminate composites. *Composite Structures*, 52(3-4):405–417, 2001.

[59] N. Taniguchi, T. Nishiwaki, and H. Kawada. Tensile strength of unidirectional CFRP laminate under high strain rate. *Advanced Composite Materials*, 16(2):167–180, 2007.

[60] N. Taniguchi, T. Nishiwaki, N. Hirayama, H. Nishida, and H. Kawada. Dynamic tensile properties of carbon fiber composite based on thermoplastic epoxy resin loaded in matrix-dominant directions. *Composites Science and Technology*, 69(2):207–213, 2009.

[61] H. Koerber, J. Xavier, and P. P. Camanho. High strain rate characterisation of unidirectional carbon-epoxy IM7-8552 in transverse compression and in-plane shear using digital image correlation. *Mechanics of Materials*, 42(11):1004–1019, 2010.

[62] H. Al-Zubaidy, X.L. Zhao, and R. Al-Mahaidi. Mechanical characterisation of the dynamic tensile properties of CFRP sheet and adhesive at medium strain rates. *Composite Structures*, 96(0):153–164, 2013.

[63] O. I. Okoli and G. F. Smith. The effect of strain rate and fibre content on the Poisson's ratio of glass/epoxy composites. *Composite Structures*, 48(1-3):157–161, 2000.

[64] H. M. Hsiao and I. M. Daniel. Strain rate behavior of composite materials. *Composites Part B: Engineering*, 29(5):521–533, 1998.

[65] I. W. Hall and M. Guden. High strain rate testing of a unidirectionally reinforced graphite epoxy composite. *Journal of Materials Science Letters*, 20(10):897–899, 2001.

[66] T. E. Tay, H. G. Ang, and V. P. W. Shim. An empirical strain rate-dependent constitutive relationship for glass-fibre reinforced epoxy and pure epoxy. *Composite Structures*, 33(4):201–210, 1995.

[67] C. P. Buckley, J. Harding, J. P. Hou, C. Ruiz, and A. Trojanowski. Deformation of thermosetting resins at impact rates of strain. Part I: Experimental study. *Journal of the Mechanics and Physics of Solids*, 49(7):1517–1538, 2001.

[68] A. Gilat, R. K. Goldberg, and G. D. Roberts. High strain rate response of epoxy in tensile and shear loading. *Journal De Physique IV*, 110:123–127, 2003.

[69] A. Gilat, R. K. Goldberg, and G. D. Roberts. Strain rate sensitivity of epoxy resin in tensile and shear loading. *Journal of Aerospace Engineering*, 20(2):75–89, 2007.

[70] N. K. Naik, R. Gadipatri, N. M. Thoram, V. R. Kavala, and C. Veerraju. Shear properties of epoxy under high strain rate loading. *Polymer Engineering and Science*, 50(4):780–788, 2010.

[71] H. AL-Zubaidy, X. L. Zhao, and R. Al-Mihaidi. Mechanical behaviour of normal modulus carbon fibre reinforced polymer (CFRP) and epoxy under impact tensile loads. *11th International Conference on the Mechanical Behavior of Materials (Icm11)*, 10, 2011.

[72] D. Lee, H. Tippur, M. Kirugulige, and P. Bogert. Experimental study of dynamic crack growth in unidirectional graphite/epoxy composites using digital image correlation method and high-speed photography. *Journal of Composite Materials*, 43(19):2081–2108, 2009.

[73] D. Lee, H. Tippur, and P. Bogert. Quasi-static and dynamic fracture of graphite/epoxy composites: An optical study of loading-rate effects. *Composites Part B-Engineering*, 41(6):462–474, 2010.

[74] D. Lee, H. V. Tippur, B. J. Jensen, and P. B. Bogert. Tensile and fracture characterization of PETI-5 and IM7/PETI-5 graphite/epoxy composites under quasi-static and dynamic loading conditions. *Journal of Engineering Materials and Technology-Transactions of the Asme*, 133(2), 2011.

[75] D. R. Hufner and M. L. Accorsi. A progressive failure theory for woven polymer-based composites subjected to dynamic loading. *Composite Structures*, 89(2):177–185, 2009.

[76] S. Palanivelu, W. Van Paepegem, J. Degrieck, J. Van Ackeren, D. Kakogiannis, D. Van Hemelrijck, J. Wastiels, and J. Vantomme. Experimental study on the axial crushing behaviour of pultruded composite tubes. *Polymer Testing*, 29(2):224–234, 2010.

[77] M. Pankow, B. Justusson, A. Salvi, A. M. Waas, C. F. Yen, and S. Ghiorse. Shock response of 3D woven composites: An experimental investigation. *Composite Structures*, 93(5):1337–1346, 2011.

[78] F. Silva, D. Zhu, B. Mobasher, C. Soranakom, and R. D. Toledo Filho. High speed tensile behavior of sisal fiber cement composites. *Materials Science and Engineering: A*, 527(3):544–552, 2010.

[79] D. Zhu, B. Mobasher, and S. D. Rajan. *Non-Contacting Strain Measurement in Dynamic Tensile Testing*, chapter 26, pages 209–216. Conference Proceedings of the Society for Experimental Mechanics Series. Springer New York, 2011.

[80] S. Haldar and H. A. Bruck. Characterization of dynamic damage mechanisms in Palmetto wood as biological inspiration for impact resistant polymer composites. *Mechanics of Materials*, 57:97–108, 2013.

[81] R. Moulart, F. Pierron, R. Hallett, S., and R. Wisnom, M. Full-field strain measurements at high rate on notched composites tested with a tensile Hopkinson bar. *SEM Annual Conference & Exposition on Experimental & Applied Mechanics 2009*, 1:295–301, 2009.

[82] D.A. Crump, J.M. Dulieu-Barton, and M.L. Longana. Approaches to synchronise conventional measurements with optical techniques at high strain rates. *Applied Mechanics and Materials*, 70:75–80, 2011.

[83] W.H. Kruskal and W.A. Wallis. Use of ranks in one-criterion variance analysis. *Journal of the American Statistical Association*, 47(260):583–621, 1952.

[84] ASTM D2344/D2344M-13 Standard test method for short-beam strength of polymer matrix composite materials and their laminates, 2013.

[85] ASTM D4255/D4255M-01 Standard test method for in-plane shear properties of polymer matrix composite materials by the rail shear method, 2001.

[86] ASTM D7078/D7078M-12 Standard test method for shear properties of composite materials by V-notched rail shear method, 2012.

[87] ASTM D5379/D5379M-98 Standard test method for shear properties of composite materials by the V-notched beam method, 1998.

[88] ASTM D3518/D3518M-94 Standard test method for in-plane shear response of polymer matrix composite materials by tensile test of a $\pm 45^\circ$ laminate, 1994.

[89] ASTM D5448 Standard test method for inplane shear properties of hoop wound polymer matrix composite cylinders, 1993.

[90] R. E. Lavengood and M. J. Michno. Composite shear strength - tube torsion vs short beam shear. Technical Report HPC 73-155, Monsanto Research Corp, 1973.

[91] C. C. Chamis and J. H. Sinclair. Ten-deg off-axis test for shear properties in fiber composites. *Experimental Mechanics*, 17(9):339–346, 1977.

[92] F. Pierron, E. Alloba, Y. Surrel, and A. Vautrin. Whole-field assessment of the effects of boundary conditions on the strain field in off-axis tensile testing of unidirectional composites. *Composites Science and Technology*, 58(12):1939–1947, 1998.

[93] C. C. Chamis and J. H. Sinclair. 10° off-axis test for shear properties in fiber composites. Technical Report E-8577, Nationl Aeronautics and Space Administration, 1976.

[94] J. C. Marín, J. Cañas, F. París, and J. Morton. Determination of G12 by means of the off-axis tension test. Part I: review of gripping systems and correction factors. *Composites Part A: Applied Science and Manufacturing*, 33(1):87–100, 2002.

[95] N.J. Pagano and J.C. Halpin. Influence of end constraint in the testing of anisotropic bodies. *Journal of Composite Materials*, 2(1):18–31, 1968.

[96] R.R. Rizzo. More on the influence of end constraints on off-axis tensile tests. *Journal of Composite Materials*, 3(2):202–219, 1969.

[97] M. Pindera and C. Herakovich. Shear characterization of unidirectional composites with the off-axis tension test. *Experimental Mechanics*, 26(1):103–112, 1986.

[98] J. C. Marín, J. Cañas, F. París, and J. Morton. Determination of G12 by means of the off-axis tension test. Part II: a self-consistent approach to the application of correction factors. *Composites Part A: Applied Science and Manufacturing*, 33(1):101–111, 2002.

[99] F. Mujika. New considerations on the stress field in an off-axis tensile test. *Journal of Composite Materials*, 39(21):1909–1929, 2005.

[100] G.L. Richards, T.P. Airhart, and J.E. Ashton. Off-axis tensile coupon testing. *Journal of Composite Materials*, 3(3):586–589, 1969.

[101] R. B. Pipes and B.W. Cole. On the off-axis strength test for anisotropic materials. *Journal of Composite Materials*, 7(2):246–256, 1973.

[102] B. W. Chang, P. H. Huang, and D. G. Smith. A pinned-end fixture for off-axis testing. *Experimental Techniques*, 8(6):28–30, 1984.

[103] Y. Xiao, M. Kawai, and H. Hatta. An integrated method for off-axis tension and compression testing of unidirectional composites. *Journal of Composite Materials*, 45(6):657–669, 2011.

[104] C.T. Sun and S.P. Berreth. A new end tab design for off-axis tension test of composite materials. *Journal of Composite Materials*, 22(8):766–779, 1988.

[105] C. T. Sun and I. Chung. An oblique end-tab design for testing off-axis composite specimens. *Composites*, 24(8):619–623, 1993.

[106] F. Pierron and A. Vautrin. The 10° off-axis tensile test: A critical approach. *Composites Science and Technology*, 56(4):483–488, 1996.

[107] M. Kawai, M. Morishita, H. Satoh, S. Tomura, and K. Kemmochi. Effects of end-tab shape on strain field of unidirectional carbon/epoxy composite specimens subjected to off-axis tension. *Composites Part A: Applied Science and Manufacturing*, 28(3):267–275, 1997.

[108] N. Taniguchi, T. Nishiwaki, and H. Kawada. Experimental characterization of dynamic tensile strength in unidirectional carbon/epoxy composites. *Advanced Composite Materials*, 17(2):139–156, 2008.

[109] J. N. Reddy. *Mechanics of Laminated Composite Plates and Shells: Theory and Analysis (Second Edition)*. CRC Press, 2004.

[110] M. Grédiac, F. Auslender, and F. Pierron. Applying the virtual fields method to determine the through-thickness moduli of thick composites with a nonlinear shear response. *Composites Part A: Applied Science and Manufacturing*, 32(12):1713–1725, 2001.

[111] H. Chalal, F. Méraghni, F. Pierron, and M. Grédiac. Direct identification of the damage behaviour of composite materials using the virtual fields method.

Composites Part A: Applied Science and Manufacturing, 35(7-8):841–848, 2004.